

THE ROLE OF HEMODYNAMICS IN DETERMINING DRUG DEPOSITION IN STENT-BASED DELIVERY

Caroline C. O'Brien

THE UNIVERSITY OF
NEW SOUTH WALES



SYDNEY • AUSTRALIA

A thesis submitted in fulfilment of the requirements for the degree

Doctor of Philosophy

March 30, 2012

COPYRIGHT STATEMENT

'I hereby grant the University of New South Wales or its agents the right to archive and to make available my thesis or dissertation in whole or part in the University libraries in all forms of media, now or here after known, subject to the provisions of the Copyright Act 1968. I retain all proprietary rights, such as patent rights. I also retain the right to use in future works (such as articles or books) all or part of this thesis or dissertation.

I also authorise University Microfilms to use the 350 word abstract of my thesis in Dissertation Abstract International (this is applicable to doctoral theses only).

I have either used no substantial portions of copyright material in my thesis or I have obtained permission to use copyright material; where permission has not been granted I have applied/will apply for a partial restriction of the digital copy of my thesis or dissertation.'

Signed

Date

AUTHENTICITY STATEMENT

'I certify that the Library deposit digital copy is a direct equivalent of the final officially approved version of my thesis. No emendation of content has occurred and if there are any minor variations in formatting, they are the result of the conversion to digital format.'

Signed

Date

Originality Statement:

I hereby declare that this submission is my own work and to the best of my knowledge it contains no materials previously published or written by another person, or substantial proportions of material which have been accepted for the award of any other degree or diploma at UNSW or any other educational institution, except where due acknowledgement is made in the thesis. Any contribution made to the research by others, with whom I have worked at UNSW or elsewhere, is explicitly acknowledged in the thesis. I also declare that the intellectual content of this thesis is the product of my own work, except to the extent that assistance from others in the project's design and conception or in style, presentation and linguistic expression is acknowledged.

Signed.....

Date.....

ABSTRACT

Drug-eluting stents are used routinely in coronary arteries, and are increasingly being considered for non-coronary vascular beds. Yet, mechanisms governing the efficacy of the drug-eluting stent are still being understood, in particular those physiologic and device related factors that determine the arterial distribution of therapeutic agents.

The primary aim of this thesis is to determine the role of vascular-bed dependent luminal flow in dictating the extent of arterial drug deposition from endovascular stents. An integrated framework comprising computational and bench-top models has been formulated to explore the relative contributions of key hemodynamic parameters intrinsic to a vascular bed.

Using a novel, dynamically similar bench-top model, we determine that arterial drug patterns are sensitive to the net luminal flow environment, created by mean flow rate and strut geometry. This analysis is then extended to consider the mechanisms that govern the pulsatile nature of blood flow, and how they modulate arterial drug distribution. A coupled framework comprising a computational fluid dynamics and mass transfer model, along with the custom-designed bench-top model allowed us to investigate scenarios that are not possible with animal models alone. Model-based simulations predicted that when stent struts were fully-apposed only the time-averaged blood flow through the lumen (or the mean blood flow rate defined by Reynolds number) dictated the pattern of drug distribution, and not the factors that quantify the unsteady nature of blood. Contrastingly, when struts were malapposed from the wall, arterial drug uptake was found to be directly dependent on the unsteady flow effects.

Finally the effects of geometry-induced changes to the core flow were investigated, with focus on stent position at the aorta-renal ostia. The results showed that further to those local flow alterations induced by the stent strut, tissue drug uptake at the aorta-renal ostia is also modulated by both relative stent position with respect to the ostia and changes to the core flow due to bifurcation and curvature at the ostia.

GLOSSARY

Technical Terms

Hemodynamics:	The dynamics of blood flow.
Arterial wall:	Arterial wall denotes the vessel wall, that incorporates the tunica media, tunica intima and tunica adventitia.
Lumen:	The inside of a cavity, in this thesis lumen is used to describe the blood flow domain.
Mural:	The wall of a cavity, in this thesis it is used to describe the interface of the blood lumen and the arterial wall.
Endovascular/ Intravascular:	Denotes the space inside the blood vessel. This is opposed to <i>perivascular</i> , which denotes the space outside or around the vessel.
Stenosis:	The narrowing of the lumen
Stent:	Metallic scaffold implanted into a conduit, most usually a vessel.
Ischemia:	A restriction in the blood supply, most usually caused by the occlusion of the vessel due to stenosis.
Atherosclerosis:	The disease process characterised by fatty plaque build in the vessel, leading to stenosis.
Restenosis:	The reoccurrence of stenosis.
Lesion:	An abnormality in the tissue. In this thesis lesion refers to an atherosclerotic lesion.
De novo lesion:	A de novo lesion, is one that has not previously been treated by either angioplasty or stenting.

Pharmacokinetics:	The body's interaction with drug.
Neointima:	A new layer of tunica intima on the mural interface.
Neointimal hyperplasia:	The biologic response of the vessel to injury and is characterised by the formation of neointima as a result of proliferation of cells.
Thrombosis:	A blood clot.
Endothelium:	The lining of endothelial cells on the interior of the vessel wall (mural surface).
Endothelialization:	The formation of endothelium.

Abbreviations:

BMS:	Bare-Metal Stent
DES:	Drug-Eluting Stent
ARO:	Aorta-Renal Ostia
ARAS:	Atherosclerotic Renal Artery Stenosis
FS:	Fluorescein-Sodium

LIST OF PUBLICATIONS

O'Brien, C.C., C.H. Finch, P. Martens, T.J. Barber and A. Simmons, *Development of an in vitro method for modeling drug release and subsequent tissue drug uptake and deposition in a pulsatile flow network*. Annual International Conference of the IEEE Engineering in Medicine and Biology Society, EMBC'11. 2011. p. 3262 - 3265.

O'Brien, C.C., C.H. Finch, T.J. Barber, P. Martens and A. Simmons, *Analysis of Drug Distribution from a Simulated Drug-Eluting Stent Strut using an In-vitro Framework*. Annals of Biomedical Engineering, ***In Print***

TABLE OF CONTENTS

Abstract.....	i
Glossary.....	iii
List of Publications.....	v
Table of Contents.....	vi
Table of Figures.....	xii
Acknowledgements.....	xvi
CHAPTER 1. Background.....	1
1.1. Thesis Overview.....	1
1.2. Ischemic Disease: Background and Treatment Options.....	1
1.2.1. Disease.....	1
1.2.2. Treatments.....	3
1.3. Drug-Eluting Stents.....	7
1.3.1. Clinical Experience.....	7
1.4. Factors Governing Stent-Based Drug Delivery.....	13
1.4.1. Polymer Type.....	13
1.4.2. Arterial Ultrastructure.....	15
1.4.3. Flow-Mediated Deposition.....	15
1.4.4. Sensitivity to hemodynamic factors.....	17

1.5.	Hemodynamics in the Non-Coronary Vasculature	24
1.5.1.	Flow Pulsatility	24
1.5.2.	Geometry-Induced Changes to the Hemodynamic Field	26
1.6.	Summary of Literature Review and Thesis Aims	29
CHAPTER 2.	Numerical Methods	33
2.1.	Computational Schema	33
2.2.	The Computational Domain	35
2.3.	Governing Equations	36
2.3.1.	Fluid	36
2.3.2.	Porous Media	37
2.3.3.	Drug Transport	37
2.4.	Boundary conditions	38
2.4.1.	Transient Drug Release	39
2.5.	Numerical Solvers	40
2.5.1.	Finite Element Method	40
2.5.2.	Finite Volume Method	45
2.6.	Model Verification	49
2.6.1.	Description of Problem	50
2.6.2.	Solution Convergence	51
2.7.	Summary of Numerical Methods Employed	53
CHAPTER 3.	Experimental Methods	55
3.1.	Introduction	55

3.2.	Experimental Methods: Visualization of Drug Elution	56
3.2.1.	Conceptual In-vitro Framework.....	56
3.2.2.	Components of the Design.....	58
3.2.3.	Experimental Method.....	70
3.2.4.	Model Verification.....	71
CHAPTER 4.	Confirming Flow-mediated Arterial Drug Deposition.....	75
4.1.	Introduction.....	75
4.2.	Materials and Methods.....	77
4.2.1.	<i>In-Vitro</i> preparation.....	77
4.3.	Results.....	78
4.3.1.	Transport characteristics	78
4.4.	<i>In-vitro</i> Results.....	83
4.5.	Discussion.....	87
4.6.	Conclusion	95
CHAPTER 5.	Impact of Flow Pulsatility on Arterial Drug Deposition.....	97
5.1.	Introduction.....	97
5.2.	Background	99
5.2.1.	Fluid Dynamics of Pulsatile Flow.....	99
5.2.2.	Relevant Parameters Governing Pulsatility Around a Stent Strut.....	106
5.3.	Methods.....	108
5.3.1.	Numerical Simulations.....	108
5.3.2.	<i>In-vitro</i> Model.....	111

5.4.	Results and Discussion	112
5.4.1.	Pulsatility Modulates Local Flow Milieu Around Stent Struts	113
5.4.2.	Impact on Stent-Based Drug Delivery	116
5.4.3.	<i>In-vitro</i> Validation.....	121
5.4.4.	Impact of Suboptimal Deployment	123
5.5.	Conclusion	128
CHAPTER 6.	Arterial Drug Deposition at the Aorta-Renal Ostia.....	129
6.1.	Introduction.....	129
6.2.	Methods.....	131
6.2.1.	Fluid and Mass Transport Model.....	131
6.2.2.	Numerical Solution	134
6.2.3.	Mesh Dependence studies	134
6.3.	Results.....	135
6.3.1.	Flow in a Left Renal Artery Branch.....	135
6.3.2.	Arterial Drug Deposition in the Renal Branch.....	138
6.3.3.	Stent Position Determines Drug Uptake	139
6.4.	Discussion.....	149
6.4.1.	Stent Placement at the ARO Results in a Spatially Asymmetric Distribution of Drug	149
6.4.2.	Geometrical Changes to the Bifurcation Improve Flow and Spatial Distribution of Drug	151
6.4.3.	Strut spacing can improve symmetry of tissue drug distribution.....	152

6.4.4.	The ARO as an Indicator for other Vascular Beds	153
6.5.	Conclusion	154
CHAPTER 7.	Conclusions.....	156
7.1.	Specific Findings	156
7.2.	General Findings.....	158
7.2.1.	Computational Models are Invaluable Tools In Stent-Based Research.....	158
7.2.1.	Can We Run Simplified Models?	159
7.2.2.	Blood Flow Pulsatility and the Benefits of Local Drug Delivery	160
7.2.3.	Guiding Preclinical Studies for DES in Peripheral Vasculature	161
7.2.4.	Specific Case of Stenting in the Renal artery.....	163
7.3.	Future Directions	164
References	167
Appendix	182
Appendix 1	183
Appendix 2	184
Appendix 3	185
Appendix 4	188
Calibration of Signal	188
Appendix 5	189
Sensitivity Analysis: Mesh Convergence	189
Sensitivity Analysis: Time-step Convergence	190
Appendix 6	192

Sensitivity Analysis: Mesh Convergence 192

TABLE OF FIGURES

Figure 1-1: The Cappela Sideguard® Stent	4
Figure 1-2: Two-dimensional computational simulations of flow over stent struts.	8
Figure 1-3: Schematic of device deployment settings.	11
Figure 1-4: OCT image showing varying degrees of stent malapposition and association with endothelial coverage	12
Figure 1-5: 2D computational simulation of a Drug-Eluting Stent.....	19
Figure 1-6: Spatial distribution of drug with multiple DES struts.	20
Figure 1-7: Vessel-simulating flow-through cell	24
Figure 1-8: Pressure and velocity waveforms at different location of the arterial tree...	27
Figure 1-9: Recordings of blood velocity in the renal branch	29
Figure 1-10: Flow chart showing central hypothesis divided into three smaller objectives.....	32
Figure 2-1: The Computational Domain for a single stent strut in a straight arterial bed	36
Figure 2-2: Surface face of a volume element	47
Figure 2-3: Iterative convergence in numerical solvers	53

Figure 3-1: <i>In-vitro</i> bench-top model.....	59
Figure 3-2: Bench-top model showing stent strut placement	61
Figure 3-3: Pulsatile-flow generation.....	65
Figure 3-4: The drug-eluting strut used in bench-top model	68
Figure 3-5: Schematic of Side-Bi-Side Diffusion Cell used to measure diffusion through a membrane	72
Figure 4-1: Measuring diffusion properties of the system.....	80
Figure 4-2: Measuring drug release from the polyurethane membrane.....	82
Figure 4-3: Measuring drug release from the polyurethane membrane, after pre-soaking	83
Figure 4-4: Spatial map of marker drug on the surface of hydrogel.....	85
Figure 4-5: Spatial map of marker drug through the cross-section.....	86
Figure 4-6: Measured spatial marker map drug distribution.....	88
Figure 4-7: Mean concentration in the hydrogel bed, for varying Reynolds number.....	89
Figure 5-1: Nominal pressure gradient derived from renal flow rate waveform data using Womersley’s framework.	101
Figure 5-2: Effects of Womersley number on different flow regimes.....	104
Figure 5-3: Effect of a change in the Womersley number on the velocity profiles.....	105

Figure 5-4: Flow profiles used in <i>in-vitro</i> validation	112
Figure 5-5: Instantaneous flow field surrounding a stent strut	115
Figure 5-6: Arterial drug deposition for a change in the steady flow parameter	117
Figure 5-7: Arterial Drug deposition for a change in the unsteady flow parameter	120
Figure 5-8: <i>In-vitro</i> validation of sensitivity to unsteady flow	122
Figure 5-9: Arterial drug distribution for suboptimal interventional settings	124
Figure 5-10: Malapposition and the unsteady flow parameter.....	127
Figure 6-1: Computational domain for the DES at the aorta-renal ostium	132
Figure 6-2. Velocity pathlines of flow through a 90 degree branch	136
Figure 6-3: Velocity pathlines of flow through a 90 degree branch with curvature	137
Figure 6-4: Contours of the drug concentration field surrounding a stent strut.....	140
Figure 6-5: Local drug uptake from a single stent strut at axial locations downstream of ostia	141
Figure 6-6: Multiple stents struts placed at the ARO.....	143
Figure 6-7: Spatial drug concentration profiles for multiple struts placed at the ARO	145
Figure 6-8: Multiple stents struts placed at the ARO, showing strut placed at the ostia.	146
Figure 6-9: The effect of strut spacing on variability in drug concentration	147

Figure 6-10: Arterial drug uptake and position relative to ostia	148
Figure 6-11: Arterial drug uptake and strut spacing	148

ACKNOWLEDGEMENTS

Undertaking this PhD has been a truly rewarding experience. It has also required a great amount of intellectual and emotional effort. Without the help and guidance from a great number of people, the submission of this thesis would not have been possible.

First I would like to thank my supervisors, Professor Anne Simmons and Associate Professor Tracie Barber, for all their support over the three years it has taken me to do this PhD. They gave me the freedom to choose any research path, providing me with endless resources in the forms of students, equipment and knowledge.

I am thankful to Professor Anne Simmons for taking me on as a PhD student. Having only met me for ten minutes during a lunch time break in summer of 2009, I appreciate you having faith in me as a researcher and for providing a scholarship, enabling me to pursue a PhD. Thank you for your time and patience in formulating my research plan, analysing my results and helping to develop my writing.

To Associate Professor Tracie Barber, thank you for teaching me the ‘ins and outs’ of CFD. Thank you for always being excited about my results, for believing in me and my research from the very beginning, until the very end. Thank you for patiently working with me to develop my scientific writing, and going through each and every draft I sent you. Personally, you have been a constant source of inspiration to me - appearing to so easily manage life as an academic, researcher, supervisor and mother- I hope that we can continue our relationship into the future.

Over the course of my PhD I was lucky enough to collaborate with the Elazer Edelman Laboratory at the Harvard-MIT Division of Health Sciences. Professor Edelman thank you for sharing your expert knowledge and teaching me your unique philosophy to biomedical research; the research skills I have learnt as part of our collaboration have helped propel me from young mechanical engineer to biomedical researcher. Thank you also for giving me the opportunity to visit your laboratory for the month of August 2011, I look forward to our future collaborations together.

To Dr. Vijaya Kolachalama, who as a fellow mechanical engineer, applied mathematician and biomedical researcher, has been an advisor, a teacher, a mentor and a friend to me. We have worked closely formulating our research into the impact of flow pulsatility on arterial drug deposition, and I appreciate all the late nights you spent talking from your desk in Boston, in this time you have taught me so much about research, writing and life. You have so patiently translated physiology to physics, helped me structure my research and helped me communicate my findings; I am very grateful. Thank you for giving me the confidence to pursue post-doctoral research.

Thank you to all my fellow students, staff and post-docs at the Graduate School of Biomedical Engineering and Mechanical Engineering. First to all the technical staff at Mechanical Engineering and GSBmE, thank you for being patient with me and teaching me the practical skills of being a biomedical engineer. To Charles Finch and Harmeeek Singh, my two undergraduate students, who did so much wonderful work. You are both very intelligent and capable young apprentices, and I enjoyed being on the journey of scientific discovery with you. To Charles Finch, especially, for aiding in the design of,

and helping to perform the bench top work. Good luck to both Charles and Harmeeek with your careers, I am expecting “big things” from you both.

I would also like to thank my dear friend Cara Young, a fellow PhD student, who I met in the computer room in my very first week of graduate study. Thank you for being my friend, a confidant and a support along the well-trodden but still daunting path of being a PhD student. Thank you for teaching me and my undergraduates how to use the facilities in the biomedical laboratory, in particular for preparing the hydrogels. Thank you also for being a friend who I could unload on. I always managed to walk away from our discussions feeling more confident in myself, my research and my plans for the future.

I would like to thank my parents for encouraging me to take this PhD on. For proof-reading, for all the acclaim and praise- making me feel like I had single-handedly found the to cure to cancer.

I would like to thank my ASUS laptop. With a 17” screen, a quad-core processor, 8GB RAM and four kilos under the belt, you have been my heavy but constant companion throughout my travels: to Whistler for my honeymoon, to Boston for conferences, to New York to see my friends, to the Gold Coast for Mum’s chemotherapy treatment, to Byron Bay for a triathlon and to LA for a concert. You have allowed me to work from wherever I am in the world, and have not once broken down.

Finally I have to thank my husband Simon. For being patient with me, supporting me both emotionally and financially, and making sure I was fed. For carrying my laptop for

me each time we travelled (including on our honeymoon), and exercising patience and restraint when I said, “give me five more minutes, I just need to start another job”.

It has been a wonderful ride, thank you all.

CHAPTER 1. BACKGROUND

1.1. THESIS OVERVIEW

Drug-eluting stent (DES) therapy for the treatment of ischemic artery disease is the primary coronary intervention in millions of patients and is now being considered for use in peripheral vascular beds. Mechanisms governing DES efficacy are still being understood, particularly those physiologic and device-related factors of controlled release of therapeutic drug from endovascular stents, arterial drug pharmacokinetics and the long-term device safety and efficacy.

This thesis will consider which of those hemodynamic related factors will be critical to our understanding of DES safety. This thesis will begin with a background to ischemic disease, as well as treatment options including the stent and its drug-eluting platform. Issues arising from this form of therapy will then be discussed, followed by a review of relevant research pertaining to those factors determining efficacy in stent based drug delivery and discussion on how they relate to non-coronary applications.

1.2. ISCHEMIC DISEASE: BACKGROUND AND TREATMENT OPTIONS

1.2.1. DISEASE

The disease process underlying most ischemic disease is atherosclerosis in the arterial bed. Atherosclerosis is characterized by a fatty plaque build up in the arteries, leading to a narrowing of the vessel, or complete occlusion. Occlusions ensuing from atherosclerotic plaque can lead to ischemic attack. In the coronary pathway this can

result in myocardial infarction, or even rupture leading to thrombosis [1]. In the renal artery, ischemia can lead to neuroendocrine activity and hypertension, as well as accelerating atherosclerosis and renal dysfunction [2] while occlusion in the carotid artery can lead to stroke.

The pathogenesis of atherosclerosis is complex and has been the focus of much research, from which several hypotheses have originated. The most widely recognized, and most commonly accepted, is the response-to-injury hypothesis which intimates that endothelial injury initiates as an inflammatory response [3]. Inflammation following injury increases the vascular permeability, allowing transport for cells and lipids, (specifically low density lipo-proteins or LDL), to deposit themselves into the extracellular matrix of the intimal and medial layers [3]. The presence of these lipids encourages the localization of macrophages and other immunosurveillance cells [4], promoting migration of smooth muscle cells and stimulating neointimal proliferation. The accumulation of cells, leukocytes, lipids and macrophages initially form a fatty streak which progresses to a fibrous plaque.

The initial injury to the endothelial layer can be a result of many factors including hypertension and viral infections [3], however hemodynamic factors have also been posited as a potential cause [5-7]. This is especially true in the case of renal artery atherosclerosis where the disease is shown to preferentially occur on the caudal wall [7], proximal to the aorta-renal junction [8], an area that experiences geometry-induced blood flow separation [9, 10].

1.2.2. TREATMENTS

Ischemic disease is most usually treated with mechanical revascularization techniques, which include coronary artery graft surgery and percutaneous intervention, including angioplasty and stenting. The success percutaneous angioplasty has been hindered by poor clinical outcomes, including acute vessel closure and restenosis [11]. Angioplasty involves a balloon catheter being expanded into the vessel, immediately restoring blood flow, but also acts to weaken the vessel wall, leading to elastic recoil [12]. This then lead to the development of the endovascular stent, a permanent metallic scaffold, inserted and then expanded into the lumen, to maintain vascular patency post intervention.

Endovascular stents are now widely used in the treatment of coronary ischemia. In fact by 1999, 84% of coronary interventions were performed with a coronary stent [13]. They have also been introduced to non-coronary vascular beds [14-17]. The mechanical designs, however, can differ fundamentally depending on anatomical site of lesion. For instance in coronary interventions stents are balloon expandable and vary from 8-20mm in length and 2 to 4.5mm in diameter, while stents used in the treatment of the superficial femoral artery are generally self-expanding and 5 to 7mm in diameter and can be up to 80mm in length. Complex lesions at the sites of bifurcating vessels, often require the use of multiple stents or side-branch specific stents [18]. More recently, flaring of the proximal stent at the aorta-renal ostium either by post-dilation or with a trumpet shaped stent (Figure 1-1) is one technique being incorporated by clinicians to improve clinical outcome [16, 19, 20].

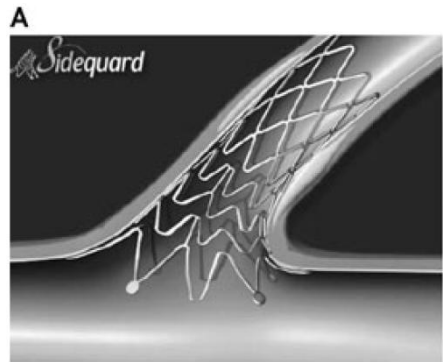


Figure 1-1: The Cappella Sideguard® Stent is a trumpet shaped stent, designed to round to the ostial walls at bifurcations. Taken from [18]. Reprinted with permission from *Journal of Interventional Cardiology*. See Appendix 1.

Long term clinical success of the Bare-Metal Stent (BMS) has been hindered by the reocclusion of the vessel, known as the condition “restenosis” [21, 22]. Restenosis is the renarrowing of the lumen ($> 50\%$) as a result of the injury caused to the wall from stent implantation. In-stent restenosis refers to the lumen loss from within the stent area, and can be focal (less than 10mm in length), diffuse (greater than 10mm in length) or occlusive.

Restenosis is known to be caused by the formation of neo-intima at the injury site on the artery wall. Since the first study by Komatsu et al. on the human systematic neointimal tissue response to stenting [23], the processes of in-stent restenosis are now well understood to be the combination of the acutely occurring inflammatory response at the time of stent implantation [24, 25], and the longer term smooth muscle cell growth and proliferation [25]. The pathogenesis of restenosis occurs over a period of weeks to years.

In the clinical setting there exist many factors determining the rate of restenosis. Patient-specific factors include diabetes mellitus and hypertension [26, 27] as well as lesion length [28], while stent design aspects like the number of stent struts [29] and stent area [30] have also been shown to be statistically significant predictors.

The clinical experience of in-stent restenosis in non-coronary vasculature is less known. Histopathology has confirmed that in-stent restenosis in the peripheral vasculature results from the same mechanisms as it does in the coronary vasculature [31]. While clinical factors, such as diabetes, hypertension and age have been correlated with in-stent restenosis in coronary stenting [26, 27], there is no evidence of such a relationship in renal artery stenting [15, 32]. In renal artery stenting anatomical factors have however been shown to be significant. Several studies have shown a consistent inverse relationship between vessel diameter and rate of restenosis [32-34]. In particular Vignali et al. reported that restenosis rates decreased significantly when vessel size was greater than 6mm (76.19% for $D < 6\text{mm}$, 23.81% for $D \geq 6\text{mm}$) [32], while Lederman et al. found an incidence rate to be significantly higher in vessels with diameter less 4.5mm (36% for $D < 4.5\text{mm}$, 12% for $D \geq 4.5\text{mm}$) [15]. Subsequent studies reported net lower rates over the whole cohort, but a similar pattern: Duda et al. reported in-stent restenosis rates for $D=5\text{mm}$ at 19%, for $D=6\text{mm}$ this rate decreased to 4.0% and for $D=7\text{mm}$ the rate was 2.5% [35]. Furthermore several studies have shown stent length to be directly proportional with restenosis rates [32-34].

The persistence of restenosis with the use of BMS [22] saw a flurry of research prompting procedural changes to the intervention method as well as more learned stent design.

Like the manifestations of atherosclerosis, neointima was shown to preferentially occur in areas of low and oscillating wall shear stress. This was demonstrated in rabbit iliac arteries [36], and in humans using combined angiographic and intravascular ultrasound techniques [37]. Consequently this prompted researchers to reconsider the design of stents now as a clinical predictor of restenosis, prompting more learned design. Indeed a single stent strut protruding into the flow creates an obstruction to the flow and thus acts to disrupt the local boundary layer flow. A principle aim of stent design was therefore to minimize the flow disruption and thus minimize alterations in the shear stress environment [38-40].

A computational fluid-dynamics study by Berry et al. [38] showed that when flow moves over a stent strut, stagnation zones are formed proximal and distal to the stent strut (Figure 1-2). The authors demonstrated that the size of these regions were determined by both strut spacing and instantaneous flow rate. In particular, with small strut spacing recirculating regions were shown to extend from one strut to the next (Figure 1-2a), or remained isolated to individual struts in the case of large enough strut spacing (Figure 1-2b & c). This fluid dynamic behaviour correlated well with experimentally observed biological outcomes, in particular those findings of Duraiswamy et al. showing platelet deposition to be strongly linked to strut spacing

[41], as well as those observations of Rogers & Edelman showing a correlation between strut spacing and local neointimal thickness in rabbit iliac arteries [42].

Further computational studies found that factors such as non-Newtonian characteristics of the flow and strut design [43], as well as strut shape and strut aspect ratio (height/width) [40] were all significant in determining the near-wall flow field. However despite the large body of research dedicated to optimizing BMS design, the emergence of the Drug-Eluting Stent (DES) shifted the focus of stent design away from BMS, towards this new paradigm of controlled and therapeutically effective drug therapy.

1.3. DRUG-ELUTING STENTS

1.3.1. CLINICAL EXPERIENCE

The use of DES is now the preferred method in percutaneous coronary intervention, performed in 80% to 90% of revascularization procedures [44]. It has also been, and is currently being, considered for non-coronary vascular beds [14, 45]. In DES the stent structure is used as a platform for localized delivery of anti-proliferative drugs (including Paclitaxel and Sirolimus) into the arterial wall. Results from major meta analyses of controlled clinical trials has shown that the use of DES for coronary artery disease has significantly decreased rates of restenosis and re-intervention, compared to the BMS [46, 47].

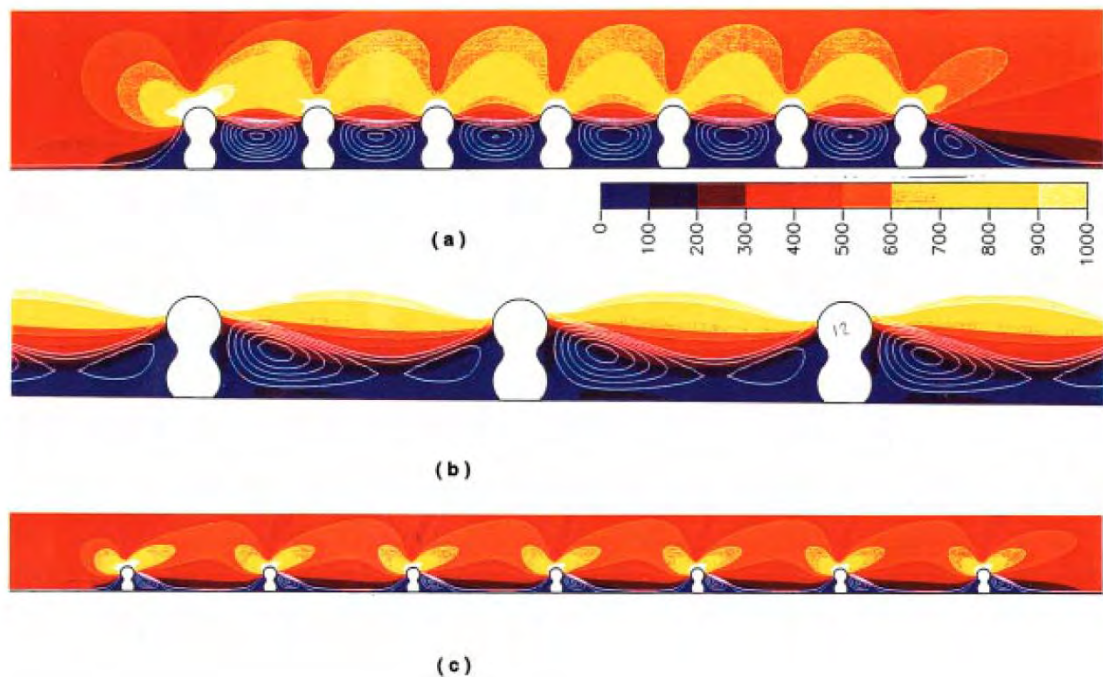


Figure 1-2: Two-dimensional computational simulations of flow over stent struts. The plot shows flow path lines and shear rate (1/s) (shown as contours) in the regions surrounding stent struts at different strut spacing. a) For small strut spacing flow recirculating regions are formed between sequential stent struts. c) However for large strut spacing flow path lines show boundary layer flow separates upstream and reattaches downstream of each stent strut. Taken from Berry et al. [38]. Reprinted with permission of *Annals of Biomedical Engineering*. See Appendix 1.

Current FDA (Food and Drug Administration, USA) approval of DES is restricted to patients with de novo lesions 28-30mm in length and vessel diameter between 2.5 and 3.75mm [46]. Owing to the size of the patient population with lesions outside this range, “off-label” use of DES has become increasingly popular, accounting for 60% of total use [48]. Off-label use has been in both small (<2.5mm) and larger arteries (>3.75mm), while lesions at junctions and branching points sometime requires multiple stents or more complex designs to be employed. While studies have shown poor long term

effectiveness in general [49, 50], the off-label use of DES in the treatment of non-coronary lesions remains unclear.

Indeed until now clinical interest has focused on the effects of drug therapy in the coronary circulation; therefore success of DES in non-coronary vasculature has not been sufficiently proven [51]. The Sirolimus-Eluting Versus Bare-Metal Low-Profile Stent for Renal Artery Treatment (GREAT) clinical trial, showed that the rate of restenosis, (measured as greater than 50% lumen loss), reduced from 14.3% in the bare metal group to 6.7% when a sirolimus-eluting stents was used [45, 52]. However it was concluded that the severity of the underlying atherosclerosis varied too considerably for statistical relevance. Because of those already reported low rates of restenosis associated with bare metal stenting in the renal vasculature for diameters 6mm or larger (< 4%, [35]), the recommendation is that DES should only be used in patients with smaller diameters, a single functional kidney or bilateral renal artery atherosclerosis [35, 53].

DES in the superficial femoral artery was shown to be successful at 6 months but not in the long term [14], with binary in-stent restenosis rates at 18 months at 20.7% in the Sirolimus-eluting group, compared to 17.9% in the control group. While in the infrapopliteal vasculature, stenting with DES has demonstrated mixed success in improving patency and reducing restenosis [54-58]. One such study by Scheinert et al. found in-stent restenosis rates were reduced from 53% with the use of BMS to 1.8% for use with a Sirolimus-eluting stents [59].

Further to restenosis, another critical long-term failure mode of DES in coronary vasculature has been thrombosis [46, 60-63]. While overall long and short term rates of

acute, later and very late thrombosis are the same for the BMS and DES groups [64], Stone et al. reported a higher incidence of late stent thrombosis with DES, however found that this was off-set by the improved rates of vessel patency when compared to the BMS group [46]. While the number of reported cases of stent-thrombosis is low (0.6% to 1% annually [61]), the consequences are often fatal, making it a cause for concern for clinicians. Thrombosis in the event of renal or peripheral DES intervention has not been reported, however stent thrombosis in the broader off-label use was reported to be statistically higher than on-label use [50, 65], particularly at sites of bifurcations in the coronary tree [60].

Stent length has been recognised as a predictor of subacute thrombosis [60]. In cases of late (more than 30 days) and very late stent thrombosis, strong histological predictors were found to be stent length and delayed neointimal healing [66-69] with incomplete reendothelialization of the stent struts [67, 70]. Anti-proliferative drugs act by inhibiting neo-intima growth to slow the healing response of the vessel however they also impair endothelial regrowth, cells which provide critical anti-thrombotic factors [71].

Ultrasound studies have shown a consistent association between stent malapposition of DES and delayed endothelialization [72, 73], leading to late and very late stent thrombosis [74, 75]. Incomplete stent apposition (malapposition) occurs as a result of outward wall remodelling as a result of chronic inflammation [75] or as a result of the stent being under expanded. Conversely over-expansion can lead to the strut being embedded in the tissue. These settings are shown diagrammatically in Figure 1-3 for a single stent strut.

Indeed the association between strut malapposition and delayed endothelialization of individual stent struts has only recently been validated (2010), a result of only those poor imaging modalities being available prior to this date. However the introduction of high resolution Optical Coherence Tomography (OCT) changed the landscape of endovascular imaging. This imaging facility allows clinicians to identify whether a strut is malapposed/embedded as well as to determine the relative amounts of tissue coverage [76, 77], allowing for even subtle biologic effects to be defined [72]. This is demonstrated in Figure 1-4, where a series of OCT images [72], shows a clear association between stent position relative to the wall and tissue coverage.

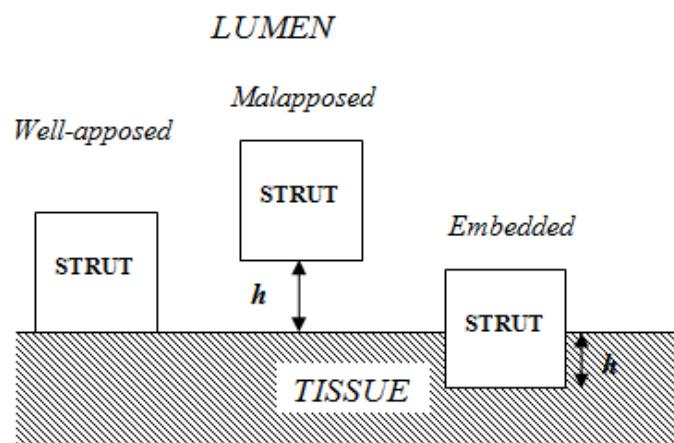


Figure 1-3: Schematic of device deployment settings. A stent strut is either well-apposed to the wall, malapposed (a displacement h from the wall, into the lumen), or embedded (a displacement h into the tissue, away from the lumen)

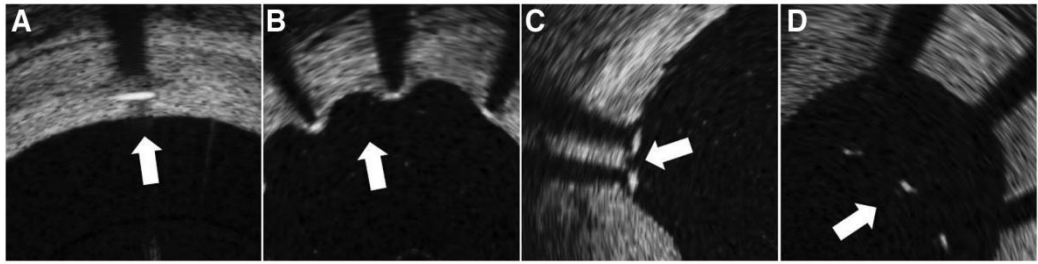


Figure 1-4: OCT image showing varying degrees of stent malapposition and association with endothelial coverage at 13 month follow up. Surface of stent strut can be identified by the high intensity line, its location is also indicated with arrow. Arrow indicates A) an embedded strut with significant endothelial coverage, B) lumenally protruding struts with moderate endothelial coverage, C) an uncovered, well-apposed strut and D) a severely malapposed uncovered stent strut. Taken from [72] and reprinted with permission from *Circulation* (See Appendix 1).

In summary the evidence suggests that those problems of thrombosis and restenosis associated with DES, are attributable to either incomplete endothelialization or a neointima hyperplastic response, respectively. This leads to the question then, what are the effects of arterial drug distribution on the endothelialization and neo-intima growth? Biologic effect has been shown to be dependent on drug dosage and can range from sub-therapeutic to toxic [78]. For instance inadequate drug concentrations will lead to neointima hyperplastic response while in areas where excess drug there will be denuded endothelia [79, 80]. Theoretically then it is the aim of drug therapy to maintain a uniform, spatially targeted drug distribution along the entire lesion length [28], retained in sufficient but not toxic concentrations, during a time frame commensurate with the pathogenesis of restenosis [78, 81]. In order to understand how to maximise clinical benefit of the DES in both coronary and non-coronary vasculature, it will therefore be

essential to characterize those factors governing drug delivery to the arterial wall, and understand how they change with anatomical position.

1.4. FACTORS GOVERNING STENT-BASED DRUG DELIVERY

Arterial spatial and temporal distribution of drug will be established from the local delivery of drug from the drug-laden strut coating into the local tissue wall. The mesh like structure of the stent will create local variability in the tissue drug concentrations: with high concentration in the tissue immediately below the contacting surfaces and low concentrations in the interstrut regions that are not in contact with the drug source. Where uniform tissue concentration is desired, this variability in drug concentration is clinically unfavourable. However there is a growing body of evidence that this variability in spatially distributed drug is actually modulated by a series of mechanisms beyond those simple convection/diffusion forces in the tissue. These include the drug release kinetics of the coating, as well as those forces intrinsic to tissue bed and luminal flow. Each will be discussed.

1.4.1. POLYMER TYPE

Arterial exposure to the drug will be determined by the rate of release of drug. In the case of DES this is most usually achieved by using polymeric materials as a rate controlling membrane. Such membranes rely on physical process; like that of diffusion, dissolution or degradation, and are therefore preferred to chemical processes which require breaking covalent bonds [79]. Of these, the most commonly used in the DES has been non-degradable and hydrophobic polymers.

The CYPHER® stent uses a base coat of polyethylene-co-vinyl acetate (PEVA) and poly(n-butyl methacrylate) (PBMA) (66% polymer to 33% drug) and then a top coat of only PBMA. The top coat acts as a rate controlling membrane by storing the drug Sirolimus during the initial burst release. The CYPHER® stent represents a diffusion controlled reservoir device.

The TAXUS® stent by Boston Scientific employs a poly(styrene-b-isobutylene-b-styrene) triblock copolymer. In this way the drug- Paclitaxel- is released straight from the polymer matrix and therefore the TAXUS® stent represents a diffusion controlled matrix system. For a diffusion controlled membrane, like the TAXUS® stent, the rate of release is proportional to a diffusion coefficient D_c . By varying these diffusion coefficients, D_c , in a 2D computational model of drug delivery (this method will be discussed later in Section 1.4.4.1), both Balakrishnan et al. [81] and Mongrain et al. [82] were able to appreciate the effects of release on arterial drug deposition.

Balakrishnan et al. showed that optimal drug delivery occurred when rate of release balanced that of tissue absorption [81]. The authors demonstrated that in the instance of a bolus release (very large D_c), the drug was cleared away almost immediately by the flow before it was be absorbed by the tissue. While too slow a release of drug (very small D_c), resulted in a limited amount of drug penetrating the tissue. These findings were reiterated by Mongrain et al. [82], who found optimal uptake occurred when the diffusion coefficients were in the mid range between bolus and slow release. Further to this Balakrishnan et al. found that an optimal polymer thickness and drug loading combination was required for effective drug uptake [81].

1.4.2. ARTERIAL ULTRASTRUCTURE

Once eluted into the tissue, the architecture of the treated artery bed will control the transport of drug. Generally arteries are composed of collagen, elastin, smooth muscle cells and the extracellular matrix. In muscular arteries there is a less organized elastic lamina compared with elastic arteries. Studies by Hwang et al. showed that the extent of drug transport was dependent on the relative amounts of elastin and collagen; where hydrophobic drugs were shown to favour hydrophobic elastic tissue [83] and will preferentially partition into elastic arterial components of the tissue wall [84]. Furthermore Hwang et al. found the geometric construction of these layers leads to anisotropic diffusion of drug in the tissue [84], with subsequent experiments showing axial diffusivity to be 3-orders of magnitude larger than transmural diffusivity [85].

Atherosclerotic lesion state will also affect the local tissue capacity for absorption and retention of drug [86]. Tzafiriri et al. showed that drug binding sites and amount of lipid content (lipids attract drugs) act to alter the distribution of drugs [87]. However the extent of the lesion will vary depending on anatomical site: in the femoral artery, the lesion is mostly diffuse with a length in excess of 30cm [88] while in renal artery stenting, the lesion is most occasionally focal [7] and localized to the caudal wall.

Local thrombotic response to stent deployment can also affect arterial drug distribution by forming a mural layer that impedes drug penetration into target lesions [17,18].

1.4.3. FLOW-MEDIATED DEPOSITION

Further to those gradients found by Hwang et al. as a result of drug interaction with tissue factors, his colleagues at the Elazer Edelman Laboratory also found local drug

gradients created by the luminal flow patterns surrounding the strut [89, 90]. Figure 1-5a, like that Figure 1-2, shows that when flow moves past a stent strut, two pockets of recirculating flow (referenced as proximal (KL) and distal (MN)) are formed when the inlet flow separates at point K, and reattaches at N. Both Balakrishnan et al. and Kolachalama et al. were able to demonstrate that drug released from the adluminal surfaces (those not in contact with the vessel wall) was able to pool in these recirculating flow regions proximal and distal to the stent strut, creating standing drug rich recirculating flow in contact with the vessel wall [89] (shown in Figure 1-5b). Concentration gradients across this mural interface cause drug to diffuse through into the tissue below, serving as a secondary source of arterial drug uptake. This non-contact mediated transport of drug was found to be significant: Steady state computational simulations, shown in Figure 1-6, revealed that those stent struts with only the abluminal surfaces coated in drug (shown in green) had local peak concentrations in the tissue bed that were nearly three-fold smaller than those with all four sides coated (in orange). In fact those surfaces of the strut coating exposed to the luminal flow (adluminal) accounted for 43% of total arterial drug uptake, while that delivered from the contacting (abluminal) surface accounted for only 11% of total drug uptake [89]. This was a critical finding as it demonstrated that it was the **flow-mediated deposition** of blood solubilised drug, rather than that resulting from arterial wall contact with the drug laden surface, that accounted for the most significant contributions to overall drug uptake.

These drug distribution patterns were found to be sensitive to the degree to which the strut was exposed to the flow field. A strut with a smaller aspect ratio (Width/Height)

will protrude more into the flow, and thus have more interaction with the luminal flow field, when compared to a larger aspect ratio which will have the effect of lying almost flat against the wall. Correspondingly both Kolachalama et al. and Balakrishnan et al. reported a flow-mediated component of drug deposition that increased in magnitude and extended spatially further, with decreasing aspect ratio [89, 90].

That is by creating a greater obstruction into the flow, the distribution of drug can be locally extended far downstream of the struts contact point, leading to less variability in the distributed drug. Thus Balakrishnan et al. [89] and Kolachalama et al. [90] were able to show that the *effect* of the drug-eluting stent DES was actually **maximized** with greater obstruction to the flow. It was a critical and non-intuitive finding, since it appeared to contradict the design aims of the bare metal stent. As mentioned previously in Section 1.2.2, the specific research aim of the BMS had to been to design the stent profiles so as to minimize the flow disruption and thus minimize alterations in the wall shear stress environment. However with the DES, by increasing the flow disruption we can theoretically improve arterial drug distribution. This finding indicated that hemodynamic factors were significant in determining arterial drug deposition and thus stent efficacy, and encouraged further study in this area.

1.4.4. SENSITIVITY TO HEMODYNAMIC FACTORS

Flow directionality results in an asymmetric distribution of drug. A positive (forward) directed flow over a strut creates flow disruptions that are smaller in the proximal region and larger in the distal (Figure 1-5a). Kolachalama et al. argued that a smaller proximal recirculating region, and thus smaller volume of fluid, will allow drug to accumulate to

a much higher concentration, while a larger recirculating flow region will dilute the pooling drug [90]. Consequently the authors were able to show that the proximal region maintained higher surface concentration when compared to the distal region, despite being 3-fold smaller in size. Importantly though the resulting tissue drug uptake will also be determined by the size of the mural (tissue/lumen interface) surface area exposed to drug. So a larger distal length leads to drug being distributed far downstream of the strut. This complex behaviour results in an asymmetric distribution of drug in the tissue below, that is skewed towards the downstream (shown in Figure 1-6, in yellow).

Already discussed is the sensitivity to the stent strut aspect ratio, however stent strut spacing is also a key determinant. Stent struts reside as part of a larger network forming the stent geometry, which adds further complexity to the mechanisms of flow mediated transport. For sequentially spaced struts spatial drug distribution (Figure 1-6) is shown to increase from left to right (proximal to distal), following the direction of flow, with local variation dependent on strut spacing [89].

Furthermore these asymmetries in arterial drug uptake for a single stent strut were found to be sensitive to a change in the mean vessel flow rate. Both the separation and reattachment point will be sensitive to the magnitude of the flow, so that with increasing Reynolds numbers these regions will increase in size, acting to dilute the concentration of the pooling drug. Correspondingly Kolachalama et al. was able to show that a larger Reynolds number lead to decreased drug uptake into the tissue [90].

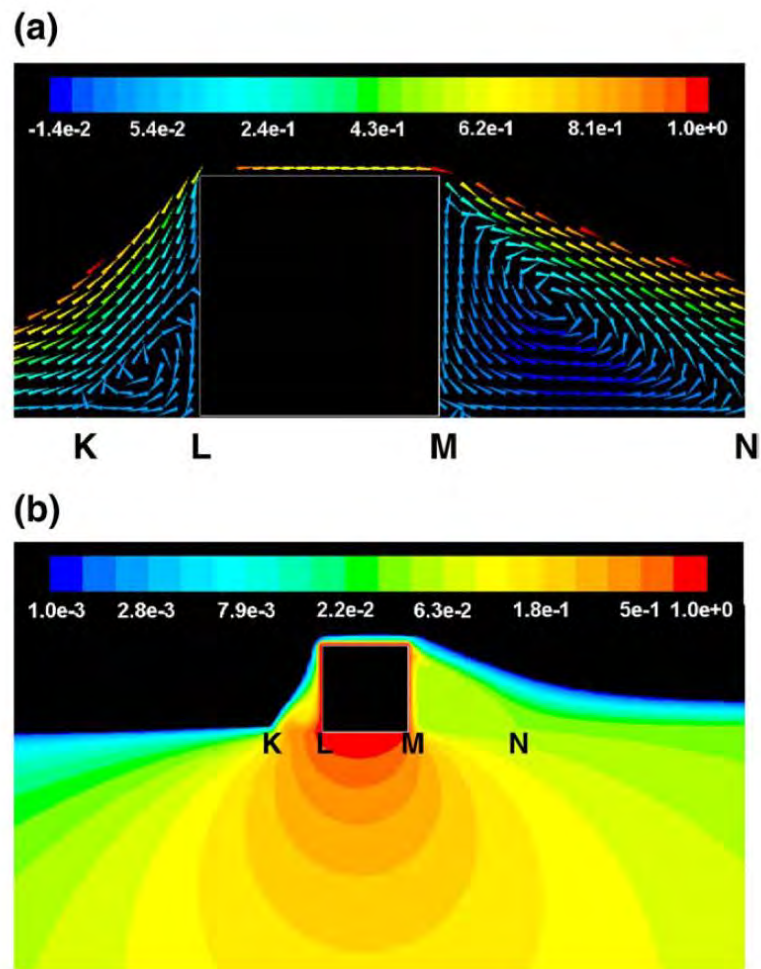


Figure 1-5: 2D computational simulation of a Drug-Eluting Stent. a) Flow over a luminal protruding strut creates two regions of recirculating flow proximal (K-L) and distal (M-N) to the stent strut. b) Asymmetries in these flow regions, create asymmetric steady state drug concentration patterns within the lumen and tissue. Figure taken from [90] and reprinted with permission from *Journal of Controlled Release* (See Appendix 1)

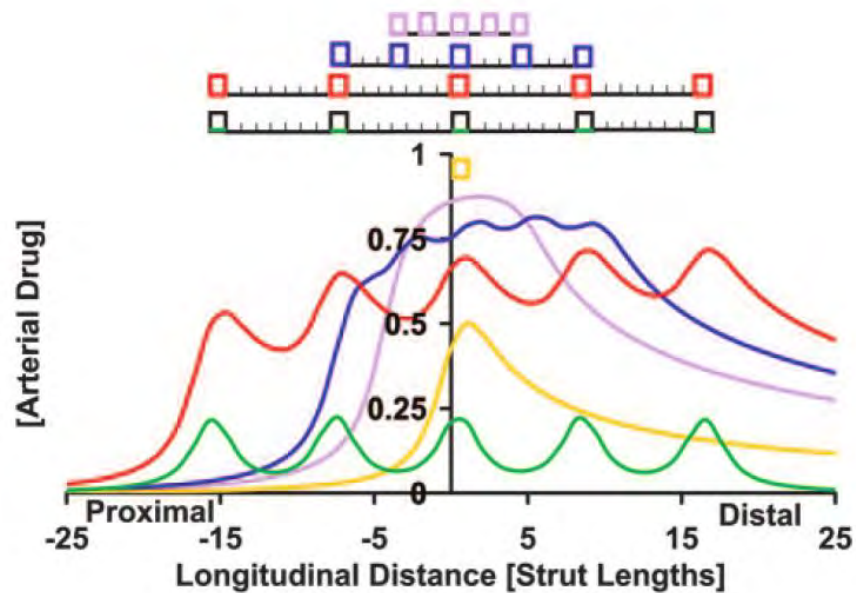


Figure 1-6: Spatial distribution of drug with multiple DES struts. Tissue drug distribution (at a point 1.5 strut widths below tissue/lumen interface). Arterial drug distribution for a single stent strut is shown in yellow. Arterial drug levels are shown to be determined by the spacing between stent struts. Taken from [89] and reprinted with permission from *Circulation* (See Appendix 1).

1.4.4.1. Methods for Appreciating Flow Mediated Deposition

Appreciating these sensitivities to the local flow field has been facilitated via numerical methods. Using computational schemes to simulate physiological transport systems is becoming increasingly more popular [91]. Rather than being utilised as a predictive tool, computational models are useful as they provide insight into biological mechanisms where other models can't. For instance systematically varying flow rate is impossible in a porcine model. Computational models allows the delineation of individual physiological variables, offering local resolution where animal models and clinical data are inadequate.

Computational models are however limited in their ability to model complete and realistic physiologic functions. Computational resources are not infinite which makes modelling physiological systems with a the wide range of space and time scales challenging.

Facilitating computational analysis requires model assumptions and simplifications, which, critically, can act to significantly affect results. The authors Vairo et al. argued that the computational scheme employed by Balakrishnan et al. [89] overestimated the sensitivity to the local flow environment [92] by assuming isotropic diffusion properties. By modelling tissue porosity and anisotropy of drug transport using those characteristics measured by Levin et al. [85] (axial diffusivity being 3-orders of magnitude larger than transmural diffusivity), the authors found transient spatial distributions in the tissue to be relatively homogeneous, unlike those gradients found by Hwang et al. [83]. Furthermore they found this distribution to be relatively insensitive to flow rate.

Indeed Balakrishnan et al. [89] and Kolachalama et al. [90] did assume isotropic diffusion of the drug in the tissue, however they also considered the problem to be steady state. It is likely the sensitivities found by Vairo et. al were indeed only small after such a short simulation time (150 hours); a time far premature of the timescale necessary for steady state concentrations to be achieved. These authors also neglected the complexity of pulsatile flow, instead running their transient simulations with a constant inlet flow rate.

In fact, all the computationally-determined results from literature discussed thus far have assumed a steady inlet flow, when in reality blood flow is dynamically changing. While Kolachalama et al. briefly considered pulsatile blood flow [90], the analysis was restricted to only a single realistic coronary waveform for a single vessel Reynolds number. Furthermore the dynamic release behaviour of the drug from the coating was neglected.

In a review of literature it becomes apparent that the dynamic coupling between the instantaneous flow and drug release from the polymer has yet to be appreciated in computational simulations of DES. While transient release of drug has been widely implemented, blood flow pulsatility has been neglected from all known simulations of DES to date [82, 89, 90, 92-94]. Indeed computationally simulating cardiac flow introduces high computational cost. Cardiac cycles are generally of the order of 1Hz, and so accurately resolving changes in the instantaneous flow rates requires sufficiently small time steps. Coupling the small time scale changes in the flow with the much larger characteristic time scale of drug release and drug transport has proven computationally elusive to date.

It is also worth considering whether a steady inlet flow is a valid assumption. Indeed it is the case that in the transport of mass with low diffusivities (high Schmidt number, $Sc > 10^3$) a lack of a significant temporal response under pulsatile flow in both straight vessels [95] and those with secondary flows [96] has been reported. However, exactly how pulsatility will effect mass transport in the presence of a time dependent point-drug

source and instantaneously changing strut induced flow alterations is unknown and should be studied

Creating a physiologically realistic, dynamically equivalent bench-top model has proven difficult to implement. While the group of researchers Seidlitz et al. have created a complex multi-compartment model simulating drug release and transport [97], they have been unable to characterize those local concentration gradients following stent placement found *ex-vivo* by Hwang et al. [83]. Shown in Figure 1-7, the model of Seidlitz et al. incorporated a stent expanded into vessel-simulating hydrogel (sink like material) and a blood mimicking solution. Unfortunately the diffusion properties of the drug in both the solution and hydrogel meant that after only 5 mins the hydrogel was inundated with drug, creating a uniform (homogeneous) distribution and thus physiologically unrealistic model of stent-based drug delivery (which occurs over months). While the authors suggested that those local gradients could be observed at 1min after incubation, this time frame is considered impractical for a full parameterization study. The authors of this particular study did not vary flow rate, but it is unlikely that sensitivities would be appreciated given the timescale of drug transport.

It is therefore yet to be determined if the findings by Kolachalama et al. [90] are valid in the instance of realistic and thus dynamically equivalent, stent based drug delivery.

Beyond the dynamic effects which have yet to be appreciated, there is the fact that each model used thus far has only considered a straight arterial bed. Vessel shape and size will change with anatomical position. Our understanding of the role of hemodynamics is

thus incomplete, especially as it relates to this drug therapy being extended from one vascular bed to others.

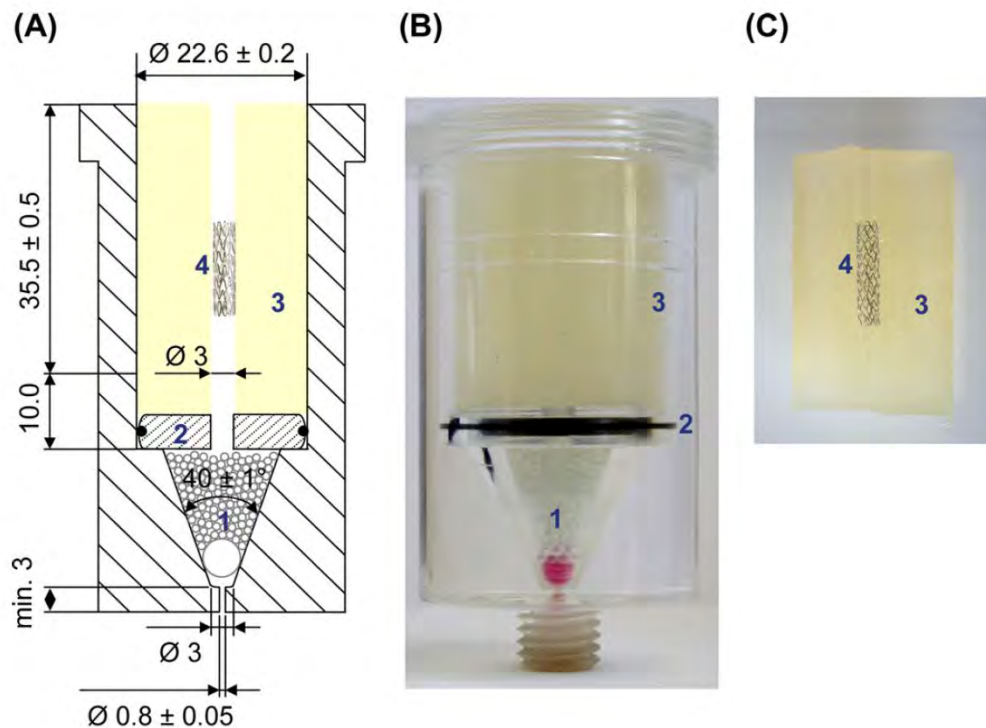


Figure 1-7: Vessel-simulating flow-through cell, shown as a) Schematic and b) real life image. c) Longitudinal cross-section of hydrogel showing stent placement. Taken from Seidlitz et al. [97] and reprinted with permission from the *European Journal of Pharmaceutics and Biopharmaceutics* (See Appendix 1)

1.5. HEMODYNAMICS IN THE NON-CORONARY VASCULATURE

1.5.1. FLOW PULSATILITY

The impact of luminal flow on arterial drug uptake is being increasingly characterized, yet several aspects associated with blood flow need to be understood. In particular, the time-varying patterns of blood flow caused by the cardiac pulse creates a time-varying

(or unsteady) flow environment that in turn may influence the overall arterial drug distribution patterns. It will be necessary to define what these changes are.

Flow profiles are vascular bed specific. Instantaneous pressure and flow change as blood moves through the arterial tree, illustrated in Figure 1-8. In the ascending aorta flow is largely positive and fast moving, with large acceleration and deceleration of the flow during systole. As flow moves down through the abdominal aorta, the low resistance regions in the kidneys mean that during rest 23% of thoracic arterial flow moves through each of the relatively small renal arteries [98]. Consequently periodic instances of retrograde flow are observed during the cardiac cycle in iliac, infrapopliteal and femoral arteries [98, 99].

Differences in instantaneous flow may be systematically quantified using dimensionless fluid dynamic parameters: the Reynolds, Re , and Womersley, α , numbers. In simple cylindrical pipe flow, a vessel is said to dynamically similar if both instantaneous Reynolds and Womersley numbers are matched. The Reynolds number is measured as $Re = \frac{2VR}{\nu}$, where R is radius of the vessel, V is the velocity and ν is the kinematic blood viscosity, and so varies significantly depending on vessel size and proportion of cardiac flow. The parameter Re measures the amount of acceleration or steady inertia of the fluid, and so a high Reynolds number denotes a mainly inertial fluid, while a low Reynolds can be assumed to be almost entirely viscous. Reynolds numbers vary from approximately 1 in the small arterioles to 4000 in the aorta [100].

The unsteady flow parameter is more complex. In his 1955 paper, J. R. Womersley numerically derived a solution to the unsteady flow harmonics [101] for a straight rigid vessel. As part of this solution, a dimensionless parameter $\alpha = R\sqrt{\frac{\omega}{\nu}}$, denoted as the Womersley number was introduced, as a function of vessel radius, pressure gradient frequency ω and the kinematic blood viscosity. This number quantifies transient inertial forces relative to viscous forces, and provides a qualitative description of the unsteady forces governing luminal blood flow that in turn are determined from the frequency and magnitude of the driving pressure gradient. A change in the Womersley number will give rise to fundamentally different flow fields through the vessel. When the Womersley number is low ($\alpha < 1$) the viscous forces dominate and flow behaves like characteristic Poiseuille parabolic flow through the cross section of the vessel. However as this Womersley number increases unsteady inertial forces dominate and profiles tend to a more blunt shape through the inviscid core of the vessel [102]. Womersley numbers can vary from less than 1 in the arterioles to 16 in the aorta [100].

As discussed in Section 1.4.3, it has been shown that net luminal flow as governed by the mean Reynolds number, Re , determines the extent of flow-mediated drug uptake [90], however the mechanism by which parameters governing flow pulsatility modulate arterial distribution are not completely characterized.

1.5.2. GEOMETRY-INDUCED CHANGES TO THE HEMODYNAMIC FIELD

Further to these dynamic flow parameters, variations in local hemodynamics due to geometry changes will present unique challenges. As flow bifurcates and expands/tapers, the boundary layer of flow separates and areas of recirculating flow

develop. Physiologically this is most prevalent at the sinus of the internal carotid artery [103] and in the aorta-renal vasculature [10].

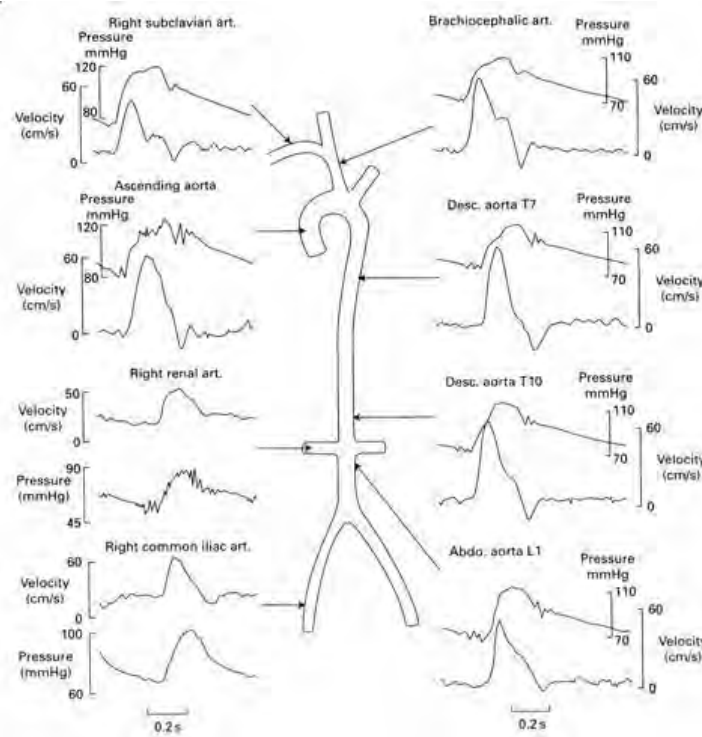


Figure 1-8: Pressure and velocity waveforms at different location of the arterial tree for a man. Both pressure and flow is shown to change dramatically at different anatomical locations. Taken from Mills et al. “Pressure flow relationship and vascular impedance in a man” [104] and reprinted with permission from the *Cardiovascular Research* (See Appendix 1).

While the effect of flow mediated drug transport has been extended to small angled bifurcations [93], the flow field and stent placement within the aorta-renal branch is unique. At the aorta-renal ostium, the renal artery bifurcates at approximately 90 degrees [10]. Clinical evidence shows that 80% of aorta-renal atherosclerosis occur proximal to the ostium [105], and are most often stenosis caused by aorta plaque encroaching on the renal branch. Suggested treatment in the instance of angioplasty

failure includes placement of an endovascular stent so that it protrudes 1 - 2mm into the aorta lumen [106] so as to prevent aorta plaque recoil [107-109]. Expansion of a stent at this location will create a 90 degree sharp edged corner at the ostia, as well as introducing significant rigidity to the vessel.

The laminar flow field around a 90 degree junction has been widely studied in literature, and there is consensus that under specific mass flow splits boundary layer separation in the renal branch will occur [9, 110, 111]. In a rigid model of a rabbit renal branch, recirculating flow was shown on the cranial side, as the boundary layer flow separates proximal to the ostia reattaching far downstream [9]. Simultaneously, on the caudal side, there was shown to be significantly high velocities [9]. The position in the instantaneous cardiac cycle will determine the extent of this separation region. This was demonstrated by Yamamoto et al. [10], and shown in Figure 1-9, using Doppler recordings of blood velocity in the renal branch. Here decelerating flow during systole was shown to cause significant reverse flow on the cranial wall as the boundary layer separates, and fast forward moving flow on the caudal wall. This axial misalignment of the flow was shown to dissipate again during diastole [10]. The size of the flow separation region will therefore be time-dependent.

Furthermore the degree of flow separation will change with downstream resistance. So that during exercise, when downstream resistance is significantly low (so to promote blood flow to the extremities) [112], boundary separation in the renal branch is significantly smaller [110].

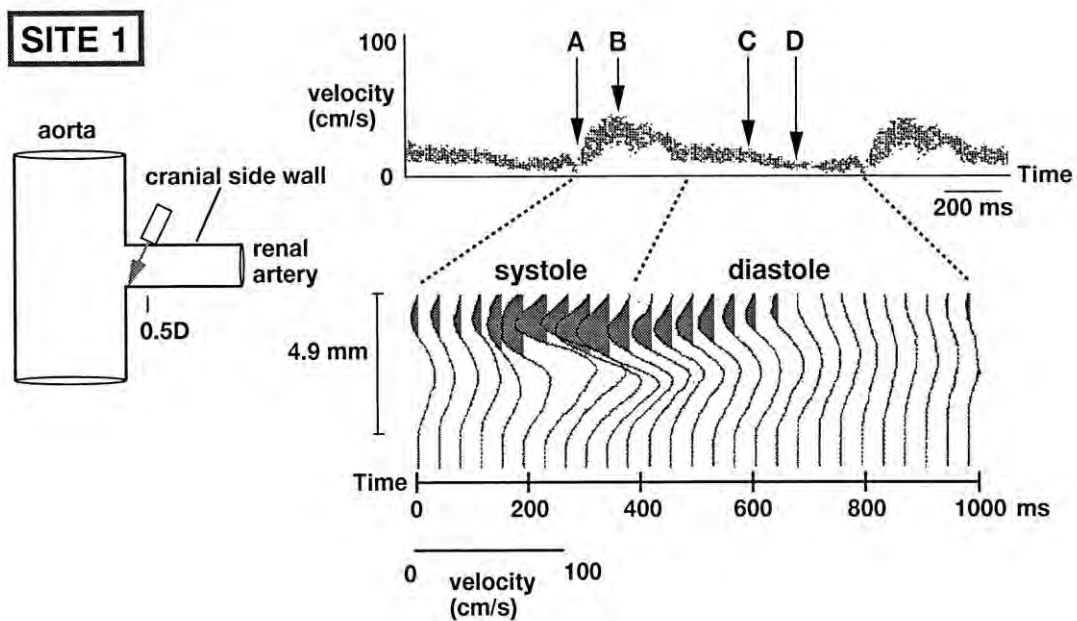


Figure 1-9: Recordings of blood velocity in the renal branch at 0.5 diameters (0.5D) downstream of ostia, at different points in the instantaneous flow cycle (A to D). Please note that angle of Doppler probe is shown figuratively. Taken from [10] and reprinted with permission from *Arteriosclerosis, Thrombosis, and Vascular Biology*.

Recent developments in stent deployment and design have seen the introduction of trumpet-shaped, side branch specific stents [113]. Shown in Figure 1-1 these stents aim to conform and round the ostial walls [18]. By creating curvature on the inner wall, the extent and position of boundary layer separation will likely change. Thus this method of implantation is likely to significantly change the flow field in the renal branch; exactly how this affects local drug deposition is unknown.

1.6. SUMMARY OF LITERATURE REVIEW AND THESIS AIMS

Implantation of an endovascular stent establishes a reactive healing process called restenosis. To circumvent this response, drugs and other therapeutic agents are coated

on the stents, which are then released into the underlying tissue bed over time. Drugs used in the DES act to inhibit neointimal hyperplastic response, however critically they also act to prevent endothelial recovery of the vessel wall, which can lead to thrombosis. Biologic effect is determined by local drug concentration: for instance local toxicity can occur in regions of vascular tissue with too high a concentration of drug, while regions of too low concentration can cause a neointimal hyperplastic response. Non-uniform drug deposition patterns established as a result of the mesh like structure of the stent, can thus create non-uniform biologic responses, where variation in hyperplastic response and delayed endothelialisation can occur, potentially leading to either vessel re-occlusion or thrombosis.

The aim of drug therapy is to achieve uniform levels of therapeutically safe and effective drug. Locally non uniform drug distributions will always persist in release from mesh-like structures like stents. However, importantly, literature has shown that luminal flow can locally extend the distribution of the drug by creating drug pooling separation regions on either side of the stent strut. Thus drug distribution is extended beyond those regions in contact with the strut, to the non-contacting regions of the tissue.

It is hypothesized that the hemodynamic environment local to the vascular bed will determine the extent and magnitude of the arterial drug distribution. As the impact of luminal flow on arterial drug uptake is being increasingly characterized several aspects still need to be understood. These include

- Understanding whether strut geometry and mean vessel Reynolds number determine uptake when blood flow is pulsatile.
- Understanding whether the pulsatility (unsteadiness) of blood flow affects arterial drug deposition. Is this the case when the stent is not ideally apposed (“malapposed”) to the wall?
- Understanding the extent to which geometry of the vessel induces changes to the local and vascular-bed wide tissue drug distribution.

The major aim of this thesis is to explore the relative contribution of key hemodynamic parameters intrinsic to the stent and vascular bed on arterial drug distribution following stent implantation. This will be achieved by considering three major aims, described diagrammatically in Figure 1-10. First will be to determine the sensitivity of flow-mediated drug to the steady flow parameter and intrinsic stent design, using a dynamically equivalent model of an implanted DES. Second it will be determined whether arterial drug distributions are sensitive to the pulsatility of the flow for several deployment settings. Finally the sensitivity in arterial drug deposition to changes in the hemodynamic field caused by non-linear geometry will be determined.

By quantifiably considering each of these flow factors in the context of stent based drug delivery, it may be possible to rationalize the limited clinical data available and potentially predict clinical outcome for stenting in the non-coronary vasculature.

The investigation of these three factors requires a simple method in which to systematically delineate the relative contributions of each. We present a 2D model of

intravascular arterial deposition from a single stent strut, presented both in a computational schema and bench-top analogue. These will be presented in the methods chapters 2 and 3.

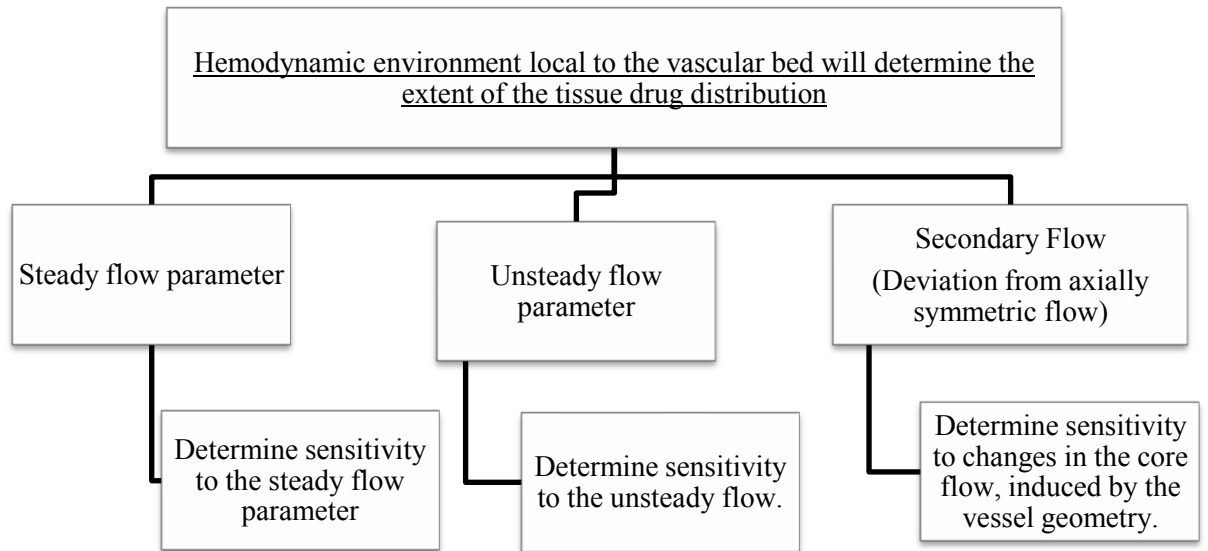


Figure 1-10: Flow chart showing central hypothesis divided into three smaller objectives. These are determining sensitivity in flow-mediated drug delivery to local dynamic flow parameters.

CHAPTER 2. NUMERICAL METHODS

This chapter outlines the numerical methods used to elucidate sensitivities to the hemodynamic environment. This chapter will begin with the presentation of a generic computational domain followed by the governing equations in which to describe the physical phenomena of stent based drug delivery. The relative benefits of two different numerical methods and their appropriateness for individual physical problems will be discussed.

2.1. COMPUTATIONAL SCHEMA

Biologic effect of stent therapy is dependent on drug being eluted and then transported and retained in the tissue bed. There are many steps from drug release to drug effect that determine biologic outcome; these include drug release kinetics, convective and diffusive transport through lumen and tissue domains and then secondary binding and tissue interactions in the tissue. Since these primary processes can be numerically modelled using continuum mechanics, systematic variation of key parameters will allow us to determine what those factors are that govern stent based drug delivery.

Presented in this chapter is a simple, idealized multidomain model of a single stent strut in a vessel, with a set of equations expressing in a formal and exact manner the relations among variables that characterise stent-based delivery of drug. These equations are analytically indeterminable and as such we rely on sophisticated numerical schemes to derive solutions.

As with any computational method, each numerical scheme will require verification and validation. These terms have been defined by the AIAA [114]:

Verification: *The process of determining that a model implementation accurately represents the developer's conceptual description of the model and the solution to the model.*

Validation: *The process of determining the degree to which a model is an accurate representation of the real world from the perspective of the intended uses of the model.*

The computational schemes employed in this thesis will be verified by considering the applicability of governing equations and optimizing system parameters so as to minimize numerical error.

In this thesis a mixture of qualitative and quantitative comparisons with selected variables will be used to validate the computational method, each of which will be detailed in the relevant chapters. While direct comparisons between computational and the designed experimental method are attractive they were determined to be unrealistic based on several limitations. For instance while steady state solutions are possible, computational power restricts the length of transient simulations to 60 seconds. However executing an experimental method in this time frame is not realistic but running any longer to achieve steady state concentrations was beyond the scope of the method.

Each of Chapters 5 and 6 handles different geometry and flow field conditions: in Chapters 5 we consider a straight arterial segment where flow is pulsatile and thus requires a time-dependent mass transport analysis, while in Chapter 6, the geometry is much more complex and only a steady state analysis is required. As such both geometry and computational schema will change. Therefore validation of the computational derived findings will be contained in those individual results chapters. Since the sensitivity analyses (time-step convergence, mesh independence) will also be problem specific, these will also be contained in relevant chapters.

This chapter begins with the presentation of a generic computational domain followed by the governing equations in which to describe the physical phenomena. Numerical solving schemes are discussed, as are their appropriateness for individual physical problems. A discussion is provided on the meshing capabilities of each solver, as well as the convergence criteria chosen.

2.2. THE COMPUTATIONAL DOMAIN

The deployment of a fully expanded, well-apposed stent creates a geometric protrusion into the flow domain and a contact surface with the tissue domain. The computational domain for a 2D reconstruction of a single, apposed stent strut is shown in Figure 2-1.

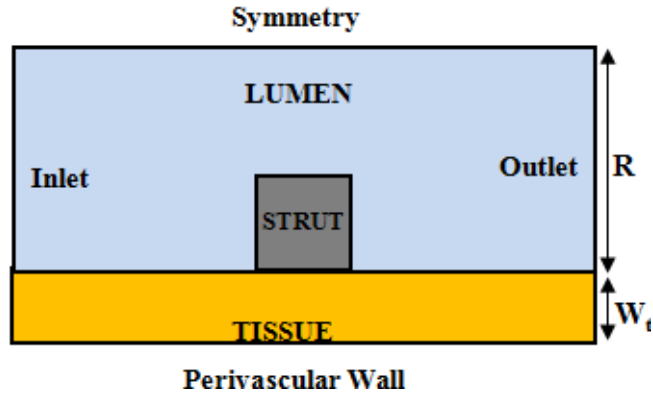


Figure 2-1: The Computational Domain for a single stent strut in a straight arterial bed. R is vessel radius and W_t is tissue thickness.

2.3. GOVERNING EQUATIONS

2.3.1. FLUID

Blood was modelled as an ideal single-phase laminar fluid. The Carreau model is used to systematically account for the shear-rate dependent characteristics of blood. This is defined as

$$\mu = \mu_{\infty} + (\mu_0 - \mu_{\infty})[1 + (\lambda\dot{\gamma})^2]^{(n-1)/2}, \quad (2-1)$$

where μ is the effective blood viscosity and in the limiting case, where shear rates go to infinity and zero, viscosity is $\mu_{\infty} = 0.0350 \text{ g cm}^{-1} \text{ s}^{-1}$ and $\mu_0 = 2.5 \text{ g cm}^{-1} \text{ s}^{-1}$, respectively. The power law index is set to $n = 0.25$ and the time constant is set to $\lambda = 25 \text{ s}$. $\dot{\gamma}$ is the shear rate determined from the solution procedure [93].

Transient luminal blood flow was modelled by utilizing the continuity and momentum relations

$$\nabla \cdot \mathbf{v}_f = 0 \quad (2-2)$$

and

$$\rho \left[\frac{\partial \mathbf{v}_f}{\partial t} + \mathbf{v}_f \cdot \nabla \mathbf{v}_f \right] = -\nabla P + \nabla \cdot (\mu \nabla \mathbf{v}_f), \quad (2-3)$$

where \mathbf{v}_f is the normalized velocity field of the fluid, P is the pressure field and ρ and μ are the density and dynamic viscosity, respectively.

2.3.2. POROUS MEDIA

The arterial wall was assumed to behave as a homogeneous porous medium. Transport of interstitial fluid was modelled numerically using the continuity equations and Darcy's momentum equation for porous media,

$$\nabla \cdot \mathbf{v}_t = 0 \quad (2-4)$$

and,

$$\rho \left[\frac{\partial \mathbf{v}_t}{\partial t} + \mathbf{v}_t \cdot \nabla \mathbf{v}_t \right] = -\nabla P + \nabla \cdot (\mu \nabla \mathbf{v}_t) - \frac{\mu}{K} \mathbf{v}_t, \quad (2-5)$$

where \mathbf{v}_t is the tissue velocity vector (in both x- and y- directions) and permeability coefficient, K , measuring the hydraulic resistance of the media.

2.3.3. DRUG TRANSPORT

A scalar transport model was employed to simulate drug transport:

$$\frac{\partial C_i}{\partial t} + \mathbf{v}_i \cdot \nabla C_i = D_i \nabla^2 C_i \quad (2-6)$$

where C_i is the normalized concentration, D_i is the diffusion coefficient of the medium, and \mathbf{v}_i is the normalized velocity vector, for both tissue and blood. Drug transport is assumed to be isotropic, with diffusion coefficients for blood and tissue taken from literature, $D_f = 3.89 \times 10^{-11} \text{ m}^2 \text{ s}^{-1}$ and $D_t = 3.68 \times 10^{-12} \text{ m}^2 \text{ s}^{-1}$, respectively [83, 90, 115]. The resulting lumen Peclet number ($Pe = Re \frac{v}{D}$) is much larger than 1, indicating a convection dominated regime. This will be significant when numerical solvers are considered (Section 2.5).

Importantly though, by modelling tissue and drug in this way, we neglect several key physiological features: Firstly drug transport through the coronary tissue was found to be anisotropic *in-vivo* [85], which has previously been considered by Vairo et al. in their computational analyses [92]. Drug partitioning, on account of binding of the drug to tissue proteins, has also been neglected (indeed partition coefficients would only change the relative magnitude but not the pattern of distributed drug). Furthermore the presence of plaque and lesion will affect both the transport of interstitial fluid and drug in the tissue. Unfortunately these diffusion properties and behaviours are yet to be characterised for non-coronary vascular beds, furthermore those lesion and bindings sites will change with vascular bed. The purpose of these computational models is to gain mechanistic insight into those processes governing flow-mediated delivery in non-coronary vascular beds and thus these behaviours are not included.

2.4. BOUNDARY CONDITIONS

The domain boundaries are shown Figure 2-1. The lumen domain inlets and outlets are problem-specific and will therefore be contained in each of the relevant chapters.

Generally they are a flow inlet condition, and zero pressure outlet condition. A symmetry boundary condition is applied representing the centreline of the flow. No-slip walls were assumed at strut/lumen and lumen/tissue interfaces. This is a valid assumption for the prescribed drug transport characteristics and flow conditions [90]. A continuity of flux is assumed the interface of fluid and tissue domains. Concentration is assumed to be zero at the inlet, and flux of drug is assumed to be zero at the lumen outlet and remaining tissue aspects, with the exception of the perivascular wall which is assumed to be impermeable. Drug is released from the strut surface using a Dirichlet boundary condition.

2.4.1. TRANSIENT DRUG RELEASE

Previously transient drug release has been modelled as a uniform release $C(t)/C_0=1$ [90, 93], or as a process of diffusion through a coating domain of defined thickness [81, 82, 92, 94]. The former is unrealistic and not representative of actual stent-based release, however handling drug release in the latter way induces unaffordable computational costs; resolving concentration in such a small thickness would require a prohibitively small mesh. Instead a simple time-dependent Dirichlet boundary condition is applied on the surface of the strut, with a flux condition prescribed by Higuchi [116]:

$$J(t) = \sqrt{\frac{D_c C_0^2}{\pi t}} \quad (2-7)$$

with the diffusion coefficient prescribed as $D_c = 1 \times 10^{-15} \text{m}^2/\text{s}$ [117], consistent with release from a TAXUS® stent. The Higuchi model assumes a release rate that is

constant with respect to the square root of time and is commonly used to describe the initial release of drug from diffusion controlled membranes [118].

2.5. NUMERICAL SOLVERS

Where these equations cannot be solved analytically, numerical schemes must be employed. Two distinct numerical methods will be described for discretizing the governing equations: the Finite Volume and Finite Element methods.

In the specific case of modelling drug transport, coupling both convection and diffusion processes for large Peclet numbers is indeed numerically challenging; where the limiting case for extremely low diffusivity problems turns the convection-diffusion equation into a wave equation (a hyperbolic partial differential equation). The numerical solution of such an equation can exhibit global spurious oscillations, especially in the vicinity of sharp gradients. The treatment of the convection term in the governing equations will determine the stability of the scheme in the case of convection dominated flows.

Various Finite Volume and Finite Element methods have introduced stabilizing schemes to circumvent this problem. These will be discussed below and their relative benefits compared.

2.5.1. *FINITE ELEMENT METHOD*

The Finite Element (F.E.) method is two-fold. First the governing equations are translated into their weak form, which are then solved in each of the finite element

subspaces. The most common of F.E. methods, the Galerkin method, formulates the weak formulation (or variational form) in terms of the divergence-free test function, \mathbf{W} , which satisfies the boundary conditions [119]. Generally, the variational or “weakened” form of a partial differential equations is created by first multiplying the governing equations by the test function and then integrating over a subspace.

The exact weak formulation of the governing equations in each finite element subspace, will depend on the order of the basis functions (element types) chosen. These basis functions will be discussed.

The domain is divided into finite elements, with nodal points at the vertexes of each mesh element. Consider two continuous elements in one-dimension, with nodal points x_1, x_2 and x_3 and characterizing the velocity variable $u(x)$, at each point then $U_1 = u(x_1)$, $U_2 = u(x_2)$ and $U_3 = u(x_3)$, respectively [120]. If these elements are defined as linear shapes then the velocity variable $u(x)$ can be linearly interpolated across the element, such that

$$u(x) = U_1\varphi_1(x) + U_2\varphi_2(x) + U_3\varphi_3(x), \quad (2-8)$$

where $\varphi_i(x)$ is a piecewise linear function, or a basis function, that equals 1 at node i and zero everywhere else. For instance at node $i=1$

$$\varphi_1(x) = \begin{cases} 1-x & \text{if } 0 \leq x \leq 1 \\ 0 & \text{if } 1 \leq x \leq 2 \end{cases}. \quad (2-9)$$

Similarly if quadratic elements are used, nodal points x_4 and x_5 , are inserted at the midpoints of those elements bounded by x_1 and x_2 , and x_3 and x_4 , respectively.

The variable u can then be defined with two additional degrees of freedom,

$$u(x) = U_1\varphi_1(x) + U_2\varphi_2(x) + U_3\varphi_3(x) + U_4\varphi_4(x) + U_5\varphi_5(x) \quad (2-10)$$

where $\varphi_i(x)$ is now a quadratic basis function that equals 1 at node i and zero everywhere else [120]. For instance at node $i=1$,

$$\varphi_1(x) = \begin{cases} (1-x)(1-2x) & \text{if } 0 \leq x \leq 1 \\ 0 & \text{if } 1 \leq x \leq 2 \end{cases} \quad (2-11)$$

In general any dependent variable u_l can be expressed in terms of their basis function (also called a **shape function**) [120].

$$u_l = \sum_i U_i \varphi_i^{(l)} \quad (2-12)$$

where \mathbf{U} is the vector of each of the components U_i and makes up the solution vector.

Following on, each of the dependent variables in a system as well as the test functions are expressed in terms of their basis functions. The **degrees of freedom** of the system will be defined by the order of the basis function for each solution variable, the number of variables and the number of elements.

Simply if the elements are linear, then the test functions can be written in terms of the basis function $v_l = \varphi_i^{(l)}$ at each node i , and then this can be substituted into the weak formulation [120].

In the standard Galerkin F.E. method the existence of a convection term in the weakened partial differential equation, will lead to strongly oscillatory solutions. The stability problems of the Galerkin formulation are spatial instabilities, caused by mesh size. If the mesh size is reduced sufficiently, these oscillations are eliminated, but it comes at great computational cost. Alternatively the Streamline-Upwind Galerkin (SUPG) stabilization scheme, as introduced by Brookes and Hughes, [121], can be implemented. This scheme adds artificial diffusion to the solution, proportional to the residual, in the direction of the streamline, to the standard Galerkin test function, \mathbf{W} . The result is a modified test function,

$$\tilde{\mathbf{W}} = \mathbf{W} + \boldsymbol{\tau}_{SUPG} \mathbf{A} \nabla \mathbf{W} \quad (2-13)$$

where \mathbf{A} is the Jacobian flux matrix appearing in the weak form of the governing equation and $\boldsymbol{\tau}_{SUPG}$ is the stabilization matrix which controls the amount of streamline upwinding, acting much like the upwind bias in F.V. upwind scheme, shown in following section in eqn. (2-17). The accuracy of the SUPG method has been shown to be $O(h^{p+1/2})$, where h is the element size and p is the order of the basis function. Thus for quadratic shape elements at least 2nd order accuracy can be achieved, making it a strongly consistent and highly accurate stabilization scheme [122]. This scheme was implemented using commercial F.E. software COMSOL 4.0a (Comsol Inc.).

Time dependent momentum and continuity equations are solved with the Generalized- α method, which is an implicit, second-order accurate method [123, 124]. In this method the non-linear system of equations are solved at each time step using a damped Newton method.

The relative error at the end of each iteration is computed as the weighted Euclidean norm,

$$\bar{E} = \left(\frac{1}{N} \sum_{i=1}^N \left(\frac{|E_i|}{W_i} \right)^2 \right)^{1/2} \quad (2-14)$$

where N is the degrees of freedom and $W_i = \max(|v_i|, S_i)$, where S_i is the scale factor calculated as $S_i = \sum_{i=1}^N |v_i| * 10^{-5}$ for highly non-linear problems or 0.1 otherwise. Only after this relative error is below a nominated threshold is the solution at that time step determined to be converged.

The meshing functionality of COMSOL 4.0a is restricted to relatively simple two-dimensional, triangulated meshes with quadrilateral elements in the boundaries. Meshing strategies do, however, allow for the Delaunay triangulation scheme, which acts to reduce the number of skewed triangles. Its algorithm works by attempting to maximize the minimum angle of all the angles in the individual triangles in the total mesh triangulation.

COMSOL allows for interpolation of the nodal values of each mesh element with shape functions of n orders. Indeed using higher order elements allows us to obtain a much

better approximation, however there is a limit; too higher an order element tends to invert and result in a distorted solution. Optimal solution properties were found when quadratic elements were used for each of the velocity and concentration variables and linear elements for pressure.

2.5.2. *FINITE VOLUME METHOD*

Different to the F.E. method, in the Finite Volume (F.V.) method governing equations are integrated over a control volume [119]. The F.V. method consists of a number of steps. First the computational domain is divided into n mesh elements and then the governing equations are discretized in integral form. The integral equations are then converted into a system of equations via a substitution of the numerical approximations for the convection, diffusion and source terms. Commercial software package ANSYS CFX v12.1 (ANSYS Inc.) was employed, and we will discuss below how each step of the F.V. method was implemented using this code.

CFX stores the solution at the nodal points (“node centred method”) however solving these governing equations in discrete form requires the calculation of surface fluxes, and thus the calculation of solution data at integration points across the face of the control volume (Figure 2-2).

Say the solution of scalar variable at node i is φ . Then the solution at the integration point is

$$\varphi_{ip} = \sum_i^N N_i \varphi_i \quad (2-15)$$

where N_i is the shape function [125], like that in the F.E. method. CFX uses trilinear shape functions in three dimensions to interpolate nodal solution variable values to integration points at element centres. Using trilinear shape functions with a structured volume mesh (hex) will result in a linearly exact interpolation value.

The diffusion term requires the calculation of the term $\left. \frac{\partial \varphi}{\partial x} \right|_{ip}$. In this approximation these shape functions are used [125]:

$$\left. \frac{\partial \varphi}{\partial x} \right|_{ip} = \sum_i^N \frac{\partial N_i}{\partial x} \varphi_i. \quad (2-16)$$

Here the cartesian derivatives of the shape functions are summed over all the shape function in the element.

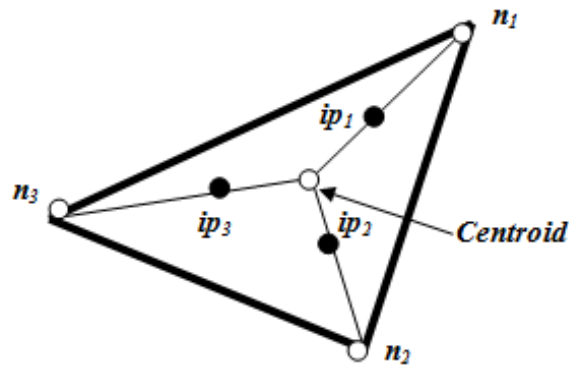


Figure 2-2: Surface face of a volume element with nodes n_i and integration points ip_i .

Numerical approximation of the advection term using a F.V. code can be handled via a number of methods. The most simple is the first-order upwind method, where the value of the scalar quantity at the integration point, is calculated directly from the upwind node. Since the first-order derivative is ignored in the Taylor approximation, we say that this method represents a first-order accurate method.

The accuracy of the solution can be improved by using higher-order numerical advection schemes. First is the power-law scheme, however in the instance of large Peclet numbers, this scheme reduces to first-order accuracy. The central differencing scheme, another alternative, uses a linear interpolation between integration points to calculate the solution variable, however for local Peclet numbers above 2, the solution can be strongly oscillatory or even diverge.

To determine the solution variable in the instance of high Peclet numbers, at the integration point, φ_{ip} , when at least second-order accuracy is desired, second order

upwind schemes are frequently employed. Importantly though this method can also introduce a third order dispersive error if the slope of the upwind node is unbounded. This was overcome by implementing the method from Barth and Jespersen [126]. In this method, the value of the scalar quantity at the integration point, φ , is calculated as

$$\varphi_{ip} = \varphi_{up} + \beta \nabla \varphi_{up} \cdot \nabla \hat{r} \quad (2-17)$$

Where φ_{up} and $\nabla \varphi$ is nodal value and gradient at the upwind node, and \hat{r} is the vector from the integration point. The β value is chosen as close to 1 as possible, so that it approximates a second order accurate solution however also ensures the fluxes are bounded.

Third-order accurate schemes, such as the Quadratic Upwind Interpolation for Convective Kinetics (QUICK) scheme, are also available. The QUICK scheme, uses a three-point upstream-weighted quadratic interpolation for the variable φ_{ip} . However in regions of large velocity or concentration gradients, the solution can overshoot or undershoot. Stability of the QUICK scheme is therefore an issue. While higher order methods (i.e. at least third-order accurate) are more accurate, the stability issues along with the significant computational cost that they induce, make them less ideal for application to our problem than a bounded, second-order upwind methods.

In the CFX solving scheme, pressure-velocity coupling is handled with the in-built Rhie-Chow algorithm [127]. Error at the end of each iteration is calculated as the scaled residual of the linearized discretized equations:

$$\bar{r}_\varphi = \frac{r_\varphi}{a_p \Delta\varphi} \quad (2-18)$$

where r_φ is the raw residual of the imbalance of the discretized equations [125]. CFX uses a simple algorithm to determine the scaling value a_p , and $\Delta\varphi$ is the range of variables in the domain [125]. The solution is considered converged if the root-mean square scaled residual is below a nominated tolerance.

2.6. MODEL VERIFICATION

Errors due to the numerical method will be a result of the iterative error in numerical calculation, those due to step size and those due to size in time step. Since grid size and time step are domain and problem specific (steady state vs. transient) we leave a thorough analysis of each to the relevant chapters.

Iterative error is measured as the magnitude of the sum of the scaled or normalized residuals (imbalances) of the discretized equations due to the use of an implicit numerical method. The use of the normalized residual is particularly important when solving for the scalar variable drug concentration (which is measured as a volume fraction), as it means that large residuals in areas of negligible volume fraction are avoided. Both CFX and COMSOL use a fundamentally similar measure of scaled residual errors (shown in eqn. (2-14) and the root-mean square error of the residual in eqn. (2-18), respectively).

A solution is determined to be converged when this source of iterative error is minimized. While iterative convergence to machine zero is desirable, it is not possible. A necessary part of computational modelling is therefore determining a stopping criteria that minimizes error but is also computationally achievable. In implicit steady state solvers, the residual is time-marched through the iterative procedure until a steady state solution is obtained. For transient solutions, convergence is required at each time step.

In order to determine the appropriate stopping criteria for solution convergence, a basic steady state problem based on that described earlier (Section 2.2 and 2.3) is set up in CFX. The convergence of parameters of interest at different stopping criteria is shown in the following section.

2.6.1. DESCRIPTION OF PROBLEM

A computational model was developed with struts modelled as blocks with unit aspect ratio and drug-laden surfaces of width 0.1mm, juxtaposed to both the lumen and the tissue wall [81, 89, 90, 128] (Figure 2-1). The radius of the vessel, R , was set at 3 mm, similar to that in the renal vasculature, and blood was assumed to be a fluid with density 1060 kg m^{-3} and a shear-independent dynamic viscosity of 0.0035 Pa s . The tissue domain was assumed to be 1mm in depth. Simulated blood flow was governed by continuity and Navier-Stokes relations, eqn. (2-2) and eqn. (2-3) respectively, and tissue modelled as a porous channel using both the continuity equation and a modified Navier-Stokes relation, eqn. (2-4) and eqn. (2-5). Volume porosity available to interstitial flow, γ , was set at 0.61 [94, 129], and Darcy's permeability was prescribed as $K = 1.43 \times 10^{-18} \text{ m}^2$ [129]. Drug concentration was specified as a normalized

concentration ($c_i = \frac{c_i}{C_{strut}}$), and modelled using a general equation for passive scalar transport of a solute (eqn. (2-6)). The scalar quantity used in this simulation has assumed diffusivity in fluid and tissue be $D_f = 3.89 \times 10^{-11} \text{ m}^2 \text{ s}^{-1}$ [115] and $D_t = 3.68 \times 10^{-12} \text{ m}^2 \text{ s}^{-1}$ [83], respectively, following that determined in-vivo.

Inlet flow was assumed to be Poiseuille parabolic, consistent with a low Womersley number ($\alpha \approx 2$), with a mean Reynolds number $Re_0 = 427$, consistent with renal arterial flow. A zero stress condition was applied at the outlet and a symmetry plane was applied at the centreline. Drug elution was handled with a Dirichlet boundary condition where normalized drug concentration was assumed be one. Continuity of flux was assumed at the lumen-tissue interface and drug concentration at the perivascular wall was assumed to be washed out ($c = 0$), and a zero concentration at the inlet. A zero flux condition was applied to all other boundaries. CFX was used to solve for the governing equations, with advection schemes and pressure-velocity couplings handled with the methods described in Section 2.5.2. The solution to volume-weighted average concentration in the tissue was found to mesh independent for 369000 elements.

2.6.2. SOLUTION CONVERGENCE

A general convergence criteria is ensuring the largest residual in the balance equations is less than some tolerance. While normal industrial convergence is roughly a RMS residual of 10^{-4} , and for an academic application this is 10^{-6} , solution convergence of high Schmidt number scalar variables requires a sufficiently small residual error. Indeed from literature, the accepted standard stopping criteria for modelling Paclitaxel in blood

flow and arterial wall transport is a mass transport residual between the orders 10^{-4} to 10^{-8} [81, 89, 90, 92, 93, 128]. A sensitivity analysis to convergence criteria was performed by comparing both the RMS residuals and the error in two key parameters- velocity at a probe in the flow and total drug uptake into the vessel- for successive iterations.

Results in Figure 2-3a showed that after 35000 iterations the drug concentration residual had been reduced by 10^{-7} , while the u velocity variable residual was reduced by approximately 10^{-17} . The solution to the probe velocity had converged at a stopping criteria of 10^{-6} , (Figure 2-3b) however this was not the case for drug uptake, measured as the Volume-Weighted Average Concentration (VWAC) in the tissue. Results showed that the error in VWAC with successive iterations was still large for a stopping criteria of 10^{-7} (35000 iterations) however this solution was converging.

Further reduction of the Drug Concentration residual beyond 10^{-7} required in excess of 35000 iterations, which was considered computationally excessive and impractical for the purposes of modelling. For this reason a 10^{-7} reduction in each of the solution variables at each successive iteration was considered a reasonable stopping criteria that was both practical to our problem and in line with that in literature.

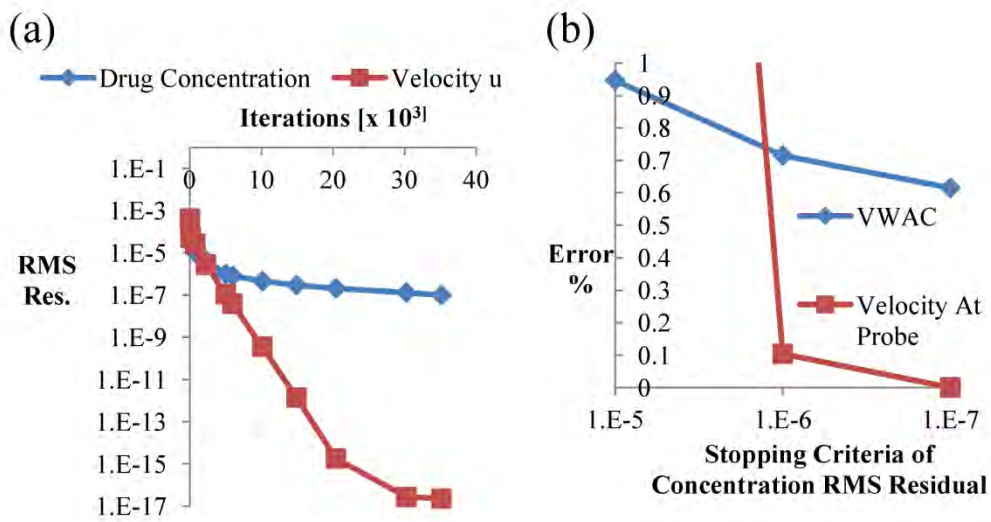


Figure 2-3: Iterative convergence in numerical solvers. a) Convergence of RMS Residual of solution variables drug concentration, c , and velocity u component. b) Error in parameters of interest with successive reduction in Drug Concentration RMS residual. These parameters of interest were velocity at a probe in the flow and drug uptake, measured as the Volume Weighted Average Concentration (VWAC) in the tissue domain.

2.7. SUMMARY OF NUMERICAL METHODS EMPLOYED

While the F.E. proved to be a robust and computationally efficient solving scheme, COMSOL's meshing insufficiencies prevented its use in modelling the complex geometry of the aorta-renal vasculature (Chapter 6).

Furthermore the efficiency (in terms of computing time) of the SUPG F.E. method compared the F.V.M make the former a more attractive scheme. Indeed, the SUPG scheme is a linear method, and when comparing similar levels of convergence requires a much sparser mesh density when compared the F.V. second-order upwind scheme [122].

For this reason it was determined that the F.E. SUPG method would be used to model drug elution from a stent strut under pulsatile flow (Chapter 5) which because of the small timescales of pulsatile flow, required computationally expensive simulations in only a simple geometry. While the F.V. second-order upwind scheme implemented in CFX would be used to determine steady state drug concentration in the aorta-renal geometry (Chapter 6).

CHAPTER 3. EXPERIMENTAL METHODS

This chapter outlines a novel experimental method used to validate computational findings. The experiment simulates drug release from a single stent strut, and then allows visualization of drug uptake into both lumen and tissue domains using optical techniques. The results will aim to confirm sensitivities to the flow field as determined computationally in Chapter 4 and Chapter 5. The method is discussed along with verification that it is an accurate representation of physiologic conditions.

3.1. INTRODUCTION

An experimental method is required to validate numerically determined results investigating those flow mediated mechanisms of drug delivery following stent implantation. Systematically delineating the effects of these parameters in animal models or with acquired clinical data is complex and for the most part inadequate. It was determined that a simple in-vitro framework would be an ideal method in which to validate computationally determined results.

In designing a rigorous and controlled bench-top method in which to vary the flow parameters, it was necessary to verify that we are in fact creating a physiologically realistic analogy. Transport characteristics of the system have been characterized and compared to both those in clinical practice, as well as those implemented into the numerical method. The results of this investigation are contained in Chapter 4.

This chapter outlines an experimental method used to validate computational findings in Chapters 4 and 5. In a simple geometry we aim to create a system in which to prove a

coupling between spatial drug map and the surrounding fluid flow following stent implantation. This will require a **Visualization of Drug of Elution and Distribution** from a model stent strut. An *in-vitro* framework is employed as a simple analogy of actual stent based drug delivery, which provides a novel platform in which to determine sensitivity to physical flow parameters α and Re . Specifically in Chapter 4 this method will be used to confirm computational studies in literature showing a flow-mediated component of drug delivery that is sensitive to Re . This method will also be employed to confirm computational findings in Chapter 5 investigating sensitivity to flow parameter α .

In this chapter the components of the design are outlined, as well as verification that it is an accurate representation of physical anatomy, realistic hemodynamic conditions and actual stent based drug delivery.

3.2. EXPERIMENTAL METHODS: VISUALIZATION OF DRUG ELUTION

3.2.1. CONCEPTUAL IN-VITRO FRAMEWORK

A novel bench-top method was constructed to appreciate the sensitivity to flow conditions, in a complete, dynamically equivalent model of stent based drug delivery. Indeed this is the first bench-top method of its kind: as discussed in Section 1.4.4.1, others [97] are yet to appreciate the local concentration gradients in the tissue following stent placement, or indeed a sensitivity to flow conditions.

The experiment represents a 2D reconstruction of a stent strut placed on a generic vascular bed. A drug-loaded elastomer is used as a model of a drug-coated wire, a

hydrogel is used to replicate the vessel wall and pulsatile flow of a blood mimicking solution is utilized (Figure 3-1a). The geometry of the channel is optimized so that when coupled with a pulsatile flow generating pump, realistic flow profiles of a range of arterial beds can be produced. The system is designed so that transport properties, via the relevant non-dimensional parameters of Peclet, Reynolds and Womersley numbers, are maintained throughout the experiment to keep the system closely related to physiologically realistic stent-based drug delivery.

Revisiting these parameters, the dynamic flow environment can be described by the flow parameters Reynolds number $Re = \frac{2VR}{\nu}$ and the Womersley number $\alpha = R \sqrt{\frac{\omega}{\nu}}$. Relative amounts of convective/diffusive transport of the drug can be determined from the Peclet number, $Pe = Re \frac{\nu}{D}$. In chapters 4 and 5 flow parameters are varied by changing the input flow rate and frequency, ω , of the flow waveform generated by the piston pump, thus it will be necessary to choose system dimensions, R , and transport properties kinematic viscosity ν and diffusivities D that are physiologically realistic. These system non-dimensional values were verified with independent experiments.

The final results of the experimental procedure will take the form of real-time experimental images of transient flow and drug distribution. The results are then compared with either literature (Chapter 4) or with computationally-obtained flow field images and spatial drug distribution maps (Chapter 5).

3.2.2. COMPONENTS OF THE DESIGN

3.2.2.1. Design Criteria

The principle aim of building this bench-top model was to verify and/or determine sensitivity to both strut geometry and flow conditions. Creating such a bench-top model in which to test flow sensitivities is complex. To accurately characterize the flow mediated contribution of drug deposition from a stent strut, it was determined that the following criteria must be met:

- The *in-vitro* system was required to provide high resolution images of spatial drug maps, with results being precise with minimal error, as well as being repeatable;
- It was essential to be able to change strut geometry and flow conditions, via instantaneous flow rate and flow frequency, in successive experiments. These changes must be precise and repeatable and reflect a full physiologic range of values;
- The method required an optically clear path through the channel, fluid and tissue for the excitation and emission of the fluorescent marker from the light source and to the camera;
- Model must be an accurate representation of physical anatomy, realistic hemodynamic conditions and actual stent based drug delivery;
- It was critical that the hydrogel and strut could be accessed at the completion of each individual experiment.

3.2.2.2. Final Design

The vessel model, as shown in Figure 3-1a, consists of an acrylic test section containing a flow channel, a hydrogel and polyurethane strip loaded with a fluorescent marker, all in a sealed arrangement. The piston pump with a working fluid of diluted glycerin solution was able to produce pulsatile flow waveforms through the channel, the resulting spatial map of fluorescently labelled drug was visualized with an epi-fluorescence microscope using the Laser Induced Fluorescence (LIF) Method (Figure 3-1b). Temperature variations were recorded to ensure constant transport properties over experimental time.

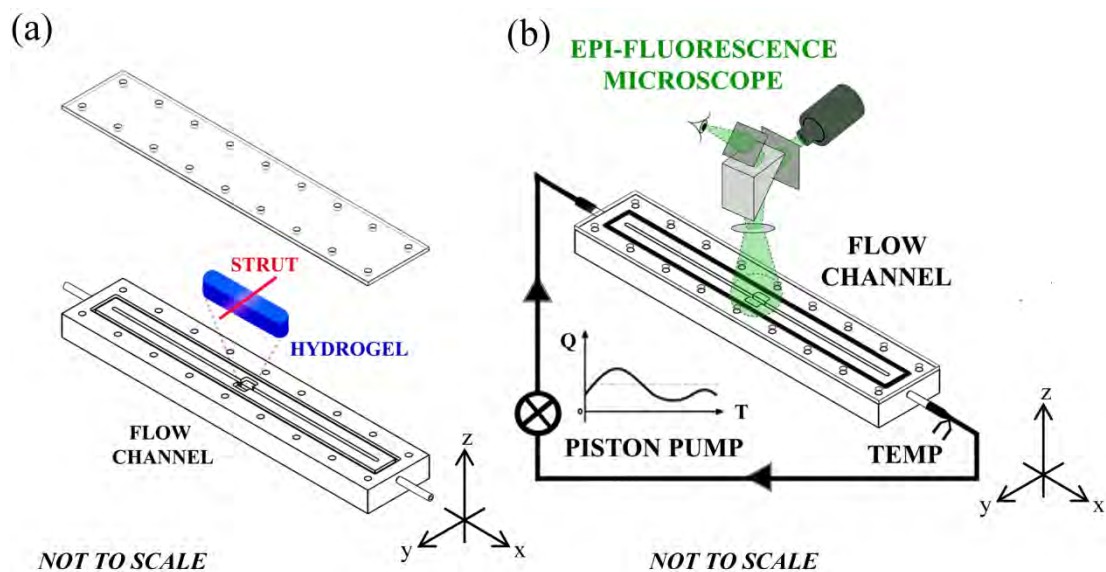


Figure 3-1: *In-vitro* bench-top model. (a) Detailed view of vessel design demonstrating placement of fluorescently loaded strut and hydrogel, within the flow channel (expanded view). (b) Schematic of *in-vitro* flow experiment (closed system). The flow channel is shown connected to the piston pump generating a pulsatile flow waveform. Temperature variations are monitored by a thermocouple. The epi-fluorescent microscope is positioned to visualise mass transport of the drug-eluting strut through the transparent acrylic channel and fluid.

3.2.2.3. Flow Channel

The channel was constructed from a clear acrylic block with flat surfaces and rigid walls; a reasonable assumption since the implantation of a stent would effectively ensure vessel rigidity. The channel was square in dimensions (3mm X 3mm), to ensure a profile with a parabolic centreline profile [130], and a length (120 mm) sufficient for fully developed flow at the region of interest. Dimensions were taken from that of a coronary vessel, as it is the most common vessel to be treated with drug-eluting stents. The channel was sealed with a 3mm thin acrylic lid, and secured with 18 X M3 screws. In order to maintain a closed fluid loop and prevent leakage an o-ring was located in a recess around the channel. The flow channel was primed prior to each experiment.

The mimic tissue bed (the “hydrogel”) was located in a recess mid-way along channel length (Figure 3-2). The well was designed so that hydrogel is flush with the vessel walls and its top surface can be exposed to the channel fluid chamber. The strut was then located on this top surface and secured in place with two acrylic blocks with M1 screws.

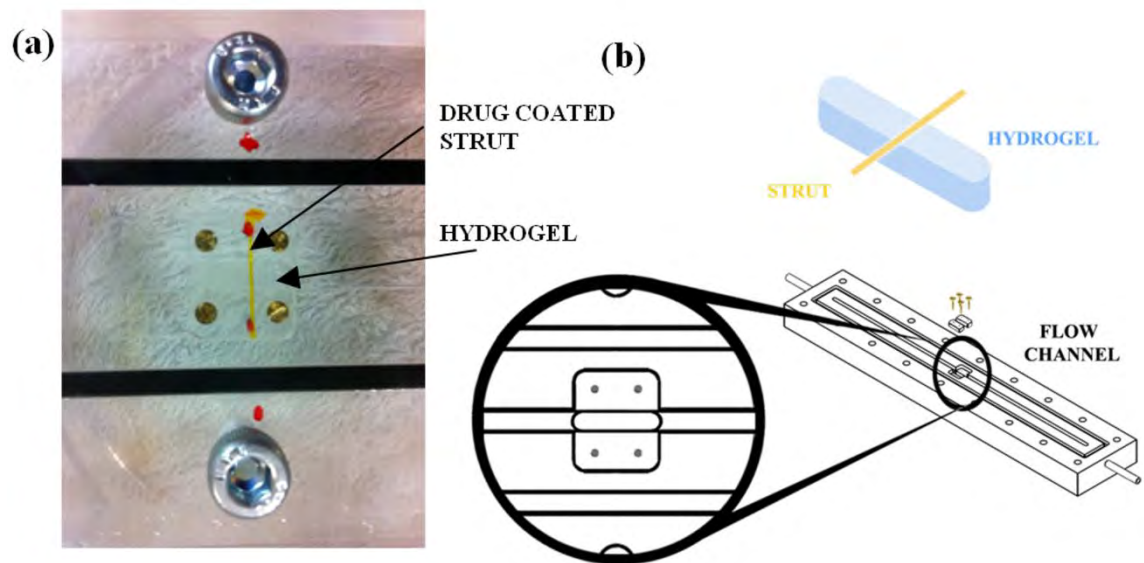


Figure 3-2: Bench-top model showing stent strut placement, a) actual and b) schematic showing the hydrogel placed in the flow channel, with the strut placed on top and secured in place with two plugs and 4X M1 screws.

3.2.2.4. Blood-Mimicking Solution

Optical requirements of the visualization method of LIF make the use of a transparent blood analogue a requirement. The working fluid consisted of a glycerin and water (40/60 vol%) mixture with 0.01% surfactant, the latter determined to be sufficiently small so as not to significantly alter the fluid properties.

Importantly though this fluid does neglect the shear thinning characteristics of blood (shear-rate dependent viscosity). Alternative blood mimicking solutions that do display non-Newtonian characteristics were found to have inferior optical properties or were determined to be incompatible with the restrictions of the piston pump which required a sufficiently lubricated working fluid. However it may be that modelling these non-

Newtonian characteristics is in fact unnecessary. Kolachalama et al. found that despite shear rates below 100 s^{-1} being observed within the flow recirculation zones, the contribution of non-Newtonian characteristics accounted for less than 4% of steady-state drug uptake into the tissue [90].

The viscosity of a glycerol/water solution is temperature dependent and was calculated using the empirical formulation given in literature [131]. The dynamic viscosity, $\mu = \nu\rho$, of water and glycerol at the temperature T between $0 - 100^\circ\text{C}$ is given by:

$$\mu_w = 1.790e^{\frac{T(T-1230)}{36100+360T}} \quad (\beta-1)$$

and

$$\mu_g = 12100e^{\frac{T(T-1233)}{9900+70T}} \quad (\beta-2)$$

The viscosity of the glycerol/water solution is given by;

$$\mu = \mu^\alpha \mu^{1-\alpha} \quad (\beta-3)$$

Where α is given by;

$$\alpha = 1 - \gamma + \frac{ab\gamma(1 - \gamma)}{a\gamma + b(1 - \gamma)} \quad (\beta-4)$$

And γ is the weight fraction between 0 and 1 of glycerol in the solution. a and b are given by;

$$a = 0.705 - 0.0017T \quad (\beta-5)$$

and

$$b = (4.9 + 0.036T)a^{2.5} \quad (\beta-6)$$

Using Cheng's formulation in eqn. (3-1) to eqn. (3-6), the dynamic viscosity at the experimental temperature of 23 ± 0.2 °C , was calculated as 4.39mPa.

Density, ρ , of the glycerol/water solution was determined from known density of glycerol, 1258 kg.m^3 , and water, 997kg/m^3 , at 23°C . The mixture of 40/60 (v/v) glycerol/water solution has a combined density, ρ_{GW} , given by

$$\rho_{GW} = 0.4\rho_G + 0.6\rho_W \quad (\beta-7)$$

Density, ρ , of the glycerol/water solution at 23°C was calculated as 1106 kg.m^3 , similar in magnitude to that commonly assumed for blood (1060 kg.m^3 at 37°C) yielding a kinematic viscosity of $3.99 \text{ cm}^2 \text{ s}^{-1}$, that is also similar to that of blood at 37°C .

3.2.2.4.1. *Temperature Control*

Since transport characteristics (Reynolds, Peclet and Womersley number) are strongly coupled to this viscosity value, it was imperative to control the temperature of the system throughout all experiments at a constant 23°C. A thermocouple ($\pm 0.05^\circ\text{C}$) was placed downstream of the channel outlet to confirm temperature invariance. The thermocouple was calibrated using a water bath between 20 – 40°C and comparison with a highly sensitive platinum resistive thermal device (RTD) with accuracy of $\pm 0.01^\circ\text{C}$. The junction of the dissimilar metals was attached to the outlet copper pipe from the acrylic channel and then insulated. The data acquisition of the recorded signal was via the DataTaker DT500 analogue to digital converter and National Instruments LabVIEW software. Temperature recordings were taken at regular intervals during the experiment to ensure temperature was maintained. Temperature variations in the *in-vitro* experiment were confirmed to vary by less than 0.2 °C above or below system temperature of 23°C.

3.2.2.4.2. *Pulsatile Flow Generation*

Pulsatile flow was incorporated using a positive displacement piston pump (CompuFlow 1000 MR, Shelley Medical Imaging Technologies, London, ON, CA), with its schematic shown in Figure 3-3a.

The piston-pump allowed different flow waveforms to be implemented. Although the 3mm X 3mm channel was designed from a coronary artery, by scaling those non-dimensional numbers (Reynolds and Womersley numbers), the flow fields of a number of arterial beds can be created. Pulsatile waveforms were implemented using a Fourier

series decomposition of suprarenal aortic flow data from literature. For instance the first six harmonics of the flow wave were derived using the data values from Moore Jnr. et al and Taylor et al [112, 132], using the method set out in Appendix 2. The first six harmonics are shown in Figure 3-3b.

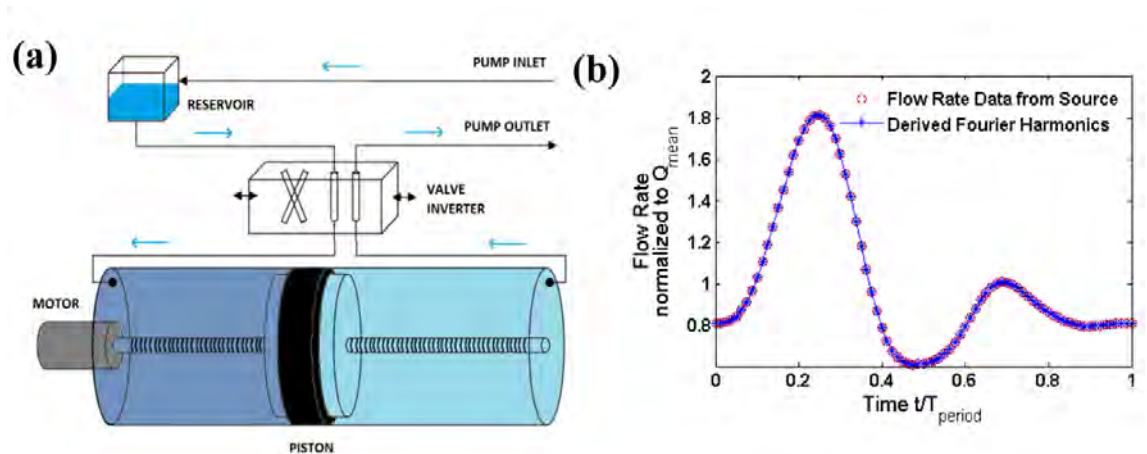


Figure 3-3: Pulsatile-flow generation. a) Schematic Compuflow 1000 Piston Pump and b) the derived Fourier harmonics of suprarenal aortic flow, taken from literature [112].

3.2.2.5. Hydrogel Preparation

For ease of use and repeatability of experimental method, it was determined that tissue specimens would be impractical for use in this *in-vitro* experiment, as they required proper incubation at a working temperature too high for effective use. The tissue substitute was required to be a sink for the eluted drug while also maintaining optical clarity. For this reason a non-biologic poly(vinyl alcohol) (PVA) hydrogel was employed. Crosslinking was optimized to slow diffusion of marker drug so that it was similar to that found *in-vivo* with Paclitaxel. The final PVA-MA macromer was fabricated from poly-(vinyl alcohol) (PVA) (16kDa, 98% hydrolysed) functionalised

with 7 methacrylate crosslinks via reaction with 2-isocyanatoethylmethacrylate (ICEMA), using the method by Bryant et. al [133].

The method of preparation of PVA-MA (7-cross-links) hydrogels from the macromer solution involves dissolving 20% of functionalised PVA-MA macromers in 75% deionised water (Milli-Q) in a heat bath at 80°C for 2 hours. After removal from the water bath, a further 5% of deionised water containing 0.05% (wt%) of photo initiator (Irgacure 2959, Ciba) was added to solution. This solution was then photo polymerised using a UV radiation lamp ($\lambda=365\text{nm}$) with intensity of $30\text{mW}/\text{cm}^2$ in an acrylic mould of the recess of flow channel. The hydrogel was radiated for 180 seconds and then swollen in glycerol/water solution for at least 48 hours before use, this was to ensure removal of the sol fraction and exchange the solvent to glycerol/water.

3.2.2.6. Fluorescent Marker Drug

A fluorescent marker (or fluorophores) was required to fluorescently map the distribution of eluted drug, yet there are many restrictions limiting use. First the mercury lamp used is most efficient exciting in the infra-red or Green spectrum, while the use of the hydrogel means that the marker must be hydrophilic. Finally we require a drug of approximately the same size as Paclitaxel ($\sim 900\text{Da}$), since drug size affects transport [134].

Green excitation state molecules include Rhodamine 6G and Rhodamine B. These were, however, found to be impractical for use with the acrylic channel, since Rhodamine was readily absorbed into the acrylic and made repeatability an issue.

While not at its peak efficiency there does exist a reasonable intensity of the Mercury lamp in the blue range. Blue excitation state molecules include the fluorophore Fluorescein with an excitation wavelength of 490nm and emission at 514nm. It is a synthetic organic compound that is small in size (300 Da) but has many larger derivatives, including Fluorescein Sodium (370 Da) and Fluorescein isothiocyanate (FITC) (4kDa-400kDa). While FITC exhibited favourable transport characteristics, it was determined that its large size (4-fold larger than Paclitaxel) made it an unfavourable option as a model drug. On the other hand Fluorescein-Sodium (FS) is small (0.5 X size of Paclitaxel), freely soluble in water and at 23°C displayed transport characteristics similar to that of actual stent based drug delivery (see Section 4.3.1.1). Fluorescein-Sodium (FS) was chosen as the model drug.

3.2.2.7. Drug Coated Stent Strut

A polyurethane elastomer was chosen as a drug carrier that could perform as both a substitute for the polymer drug delivery and stent strut. Since no strength characteristics were required in a two-dimensional reconstruction, the wire was not required and for ease of manufacture it was determined that the strut could be made entirely of cast elastomer polyurethane (Figure 3-4a).

An amorphous polymer, polyurethane represents a matrix delivery system, where molecules are released as they move through the medium. Because of the length these drugs need to travel, drug molecules near the surface will release faster than drugs further from the surface. As a result the rate of release rate tends to be proportional to the \sqrt{t} [118]. The relative loading of the drug in the polymer will modulate the release

profile of the drug; an optimal release profile was found for an initial loading of 1% (wt%) FS that were pre-soaked prior to the experiment (See Section 4.3.1.2).

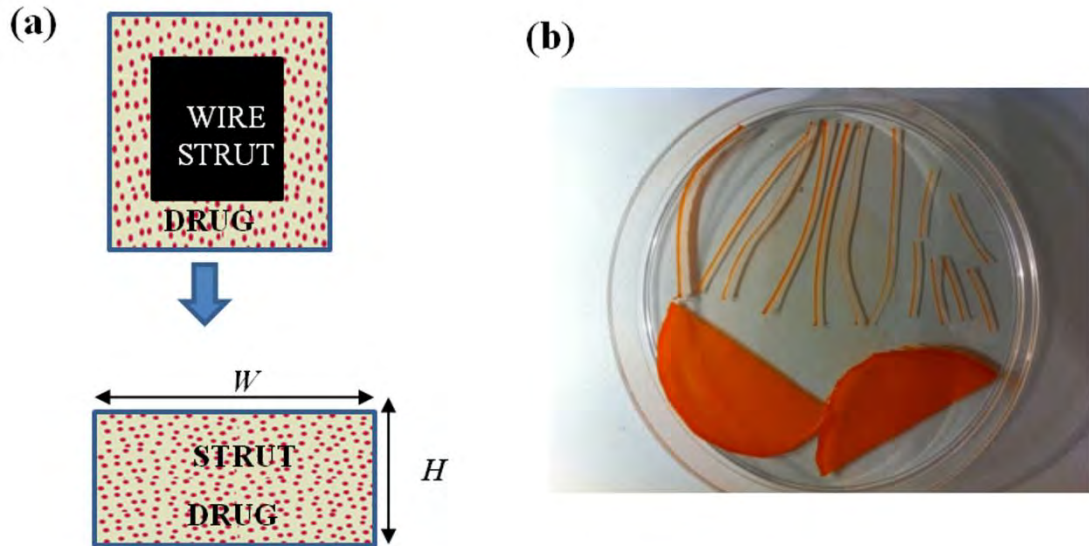


Figure 3-4: The drug-eluting strut used in bench-top model a) Schematic of a standardized drug-eluting stent strut and the drug-eluting strut used in the bench-top method. As it can be seen this is essentially a strut with approximately zero wire thickness. Strut dimensions are $W \times H$. b) Polyurethane strips loaded with Fluorescein-Sodium. Films are shown at the bottom of the dish, and the cut polyurethane strips (“struts”) are shown on top.

Polyurethane films were cast by firstly dissolving pellethane pellets (Pellethane P80A, Dow Chemical La Porte TX) in dimethylacetamide (DMA-c) and then poured into a vial and allowed to mix overnight. FS (1% wt/wt) is then dissolved into the solution and allowed to mix. Finally, the dissolved solution was poured into a 48mm diameter mould and dried in a vacuum oven at 60°C for 24 hours. The outcome of this process was 48mm diameter flexible films (Figure 3-4b).

The polyurethane films were then cut yielding two strut cross sections 0.35 mm X 0.24 mm and 0.70 mm X 0.12 mm, with aspect ratios (W/H) 1.5 and 6, respectively. In reality the cross-sections of drug-eluting stent struts are usually square or circular or somewhere in between (for instance when the corners have been polished). However importantly the aspect ratio [90] and degree of embeddedness [89] will determine arterial drug uptake. It was therefore critical to our analysis that both the geometry and the placement of the strut on the hydrogel be controlled. By employing a square cross section we were able to guarantee controlled apposition with the hydrogel, ensuring repeatability of experiment.

Films were pre-soaked for 30 minutes prior to use in both the release studies and in bench-top experimentation to remove any FS that had aggregated on the surface during the casting process (See Section 4.3.1.2).

3.2.2.8. Laser-induced Fluorescence

Illumination, filtration and detection of fluoresced particles is performed with the inverted epifluorescent microscope (Nikon Eclipse TE2000). Ultraviolet light (blue or green) is passed from a Mercury arc-discharge lamp through an excitation filter, which then is split on the surface of a dichromatic mirror through the microscope objective to the specimen. If this light source is within the excitation wavelength range of the fluorescent marker, the marker will emit a light of nominal frequency. The mercury lamp does not provide even intensity over the entire light spectrum. Peaks in intensity are near the ultraviolet at $\lambda=313\text{nm}$, 334nm , 365nm , 406nm , 435nm , $\lambda=546\text{nm}$ and

$\lambda=578$ nm. While smaller there are still reasonable intensities at the blue excitation intensity $\lambda=480\text{nm}$ to $\lambda=480\text{nm}$, making it less ideal but still usable.

This light is then filtered through an emission filter, where the image is recorded with a photo-detector, in this case a CCD camera. Images were taken at exposure times of 159ms (See Appendix 4), and processed with SPOT software. A 4X magnification is used as this allows 7 strut widths axial resolution around the strut. The channel was mounted on a purpose built stand to decrease working distance of the 4X magnification lens. Spatial resolution of the image, calibrated with a wire of known length, was found to be 600 pixels/mm.

3.2.3. EXPERIMENTAL METHOD

The experimental method includes all of the components described above to form an *in-vitro* model that elucidates drug transport in a mimic arterial segment. The final experimental arrangement includes the piston pump, channel test piece, thermocouple, glycerol/water solution, PVA hydrogel, polyurethane fluorescent strut, and epi-fluorescent microscope. Figure β -1a and Figure β -1b provides a schematic of the experimental arrangement.

Once the pump, thermocouple, microscope, mercury lamp, camera, computer are active and ready, the experimental procedure can begin. In summary this experimental procedure involves the insertion of the PVA-hydrogel into the well of the dry channel. The fluorescently-loaded polyurethane strut was placed on top of the hydrogel, and secured in place with two acrylic blocks which were then secured with M1 screws

(Figure 3-2b). The channel was sealed shut, the flow channel primed and pulsatile flow was introduced. After an experimental run-time of 180 minutes, the hydrogel was fluoresced and imaged using the method described previously. Images at an exposure of 159ms were taken of the longitudinal view, before removal and dissection of the hydrogel to obtain fluoresced images of the cross-sectional view.

3.2.4. MODEL VERIFICATION

It was necessary to verify that transport characteristics of the design were physiologically realistic and similar to that implemented into our computational schema. Diffusion characteristics of the marker drug in both fluid and tissue-mimic domains, as well as the release kinetics of the drug were characterized by considering diffusion of a solute through a medium and diffusion of a solute from a medium, respectively. The methods for the calculation of diffusion coefficients are contained below, and the results and discussion contained in Chapter 4.

3.2.4.1. Defining Transport Characteristics of *in-vitro* System

3.2.4.1.1. Measuring Diffusion Through a Medium

The diffusion coefficients for FS in the working fluid, D_{fluid} , and through the hydrogel, $D_{hydrogel}$, were experimentally determined using a two compartment diffusion cell (SIDE-BI-SIDE, PermeGear). The Side-Bi-Side Cell consists of donor and receptor 3mL fluid chamber surrounded by a water jacket. The internal fluid chambers are open to the side with a flat orifice and to a vertical sample port. The side orifices align with the intention of a membrane to be placed between. The chambers are clamped together

to seal about the orifice opening. Magnetic stir bars keep both chambers consistently mixed over the duration of the experiment. This ensures that both chambers have an even distribution of the solute, and that the concentration gradient is only active over the thickness of the membrane.

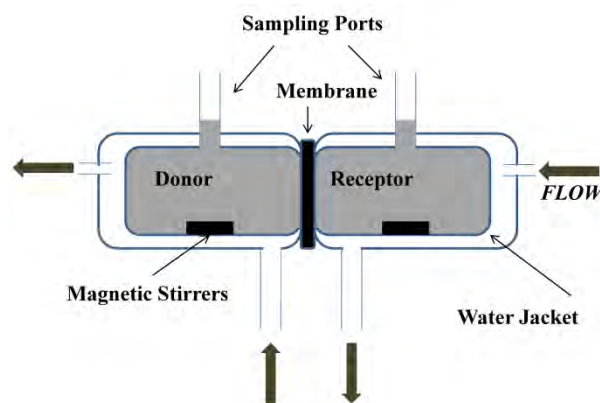


Figure 3-5: Schematic of Side-Bi-Side Diffusion Cell used to measure diffusion through a membrane.

At time zero, both reservoirs were filled with working fluid, however, the donor chamber contained a known concentration of the fluorescein solute. The diffusivity of FS through the working fluid, D_{fluid} , was determined by measuring the rate at which solute transferred over a hydrophilic filter (GV, 0.22 μ m pore diameter, 70% porosity, 0.125mm thickness, Millipore) with a known thickness. The filter membrane was considered to have negligible impedance on the solute due to the pore size being at least two orders of magnitude greater than the FS molecular radius (0.45nm).

A micro plate reader (INFINITE 200PRO, Tecan) measured the intensities of samples taken from the receptor chamber of the diffusion cell over time. To determine the concentration of solute, these readings were compared to a standard dilution series. The

permeability coefficient, P , is given by the solute transfer in relation to the normalised concentration gradient, as given by the equation [135]:

$$\ln\left(1 - \frac{2c_t}{c_0}\right) = -\frac{2A}{V}Pt, \quad (\beta-8)$$

where c_t is the solute concentration in the receptor chamber at time t and c_0 is the initial concentration of the donor chamber. The area, A , of permeation is given by the orifice area (64.6 mm^2) multiplied by the porosity of the membrane, and V is the volume of each chamber (3 mL). The diffusion coefficient, D , can be found by multiplying the permeability, P , by the distance travelled, which in this case was the thickness of the membrane, δ [135]. The experiment was repeated for the filter paper membrane and for a PVA-MA hydrogel membrane (80% porosity, 1mm thickness) to obtain D_{fluid} and $D_{hydrogel}$, respectively. Water jackets surrounding the reservoirs were maintained at a temperature of $23 \pm 0.9^\circ\text{C}$.

3.2.4.1.2. Measuring Release From a Polymer

Characterisation of the drug release from the polyurethane films was also conducted using the two compartment diffusion cell. FS loaded polyurethane film with known thickness, 2δ , was placed between the chambers and both reservoirs filled with glycerin/water solution, controlled at temperature $23 \pm 0.9^\circ\text{C}$, were sampled over time.

The diffusion coefficient, $D_{coating}$, was determined by [118]:

$$\frac{M_t}{M_\infty} \approx 4 \sqrt{\frac{Dt}{\delta^2 \pi}}, \quad (\beta-9)$$

where M_t is the solute released at time t and M_∞ is the amount of solute at time $t=0$.

Three cells were utilised, yielding six exposed films in which to study release from.

CHAPTER 4. CONFIRMING FLOW-MEDIATED ARTERIAL DRUG DEPOSITION

Published computational models of stent based drug delivery have demonstrated how dynamic asymmetries in the localised flow about stent struts, contributes to significant variation in the spatially distributed arterial drug. A novel bench-top experiment has been created to confirm this phenomena. In this chapter we use the experimental method discussed in Chapter 3 to simulate drug release from a single stent strut, under various flow conditions, and visualise drug uptake into both lumen and tissue domains using optical techniques. Results confirm the existence of inhomogeneous and asymmetric arterial drug distributions, with this distribution shown to be sensitive to both strut geometry and flow rate.

4.1. INTRODUCTION

The biologic effect of the DES- and therefore the success of this form of drug therapy - lies in its ability to deliver safe and therapeutically effective levels of drug along the entire lesion length [28]. This spatial distribution of drug is determined by a series of mechanisms post-implantation. Firstly, kinetics of the drug in the polymer drug carrier determine the amount of drug released from the strut coating [81]. Drug is then delivered either directly to the vessel wall, or to the blood stream where convective and diffusive forces can carry it to the mural interface for a secondary source of drug uptake [89]. Spatial drug distribution is governed primarily by the tissue's transport forces, as well as tissue and drug physicochemical properties. For example, protein transport will facilitate circumferential diffusion [115] while hydrophobic interactions can lead to significantly large spatial concentration variations [83, 136].

In determining the relative contributions of local hemodynamics to arterial drug deposition, computational models are frequently employed [82, 90, 92, 137]. However a lack of available computational resources can mean that some dynamic behaviour is excluded, in order to facilitate analysis of other systemic parameters. For instance simultaneously modelling dynamically changing pulsatile flow with realistic transient drug release, over a reasonable time frame has proven elusive, both computationally and experimentally. Therefore our understanding of flow-mediated deposition of drug in the presence of these dynamic couplings is not complete.

The objective of the study in this chapter is to create a dynamically equivalent model of stent based drug delivery. The resulting spatial maps of drug under varying flow conditions, will allow us to elucidate sensitivities in arterial drug deposition to both strut geometry and local flow magnitude around the strut. From these findings we will be able to either negate or confirm those findings in literature by Kolachalama et al. [90] and Balakrishnan et al. [89].

The experiment represents a reconstruction of a stent strut placed perpendicularly opposing axially aligned flow, on a generic vascular bed. A drug-loaded elastomer is used as a model of a drug-coated wire, a hydrogel replicates the vessel wall and pulsatile flow of a blood mimicking solution is utilized. Instantaneous flow rates and profiles in this study are based on the renal artery, as further work (Chapter 6) focuses on drug delivery in non-coronary vasculature.

The system is designed so that transport properties (via the relevant non-dimensional parameters of Peclet, Reynolds and Womersley numbers) are maintained throughout the

experiment, so to keep the system closely related to physiologically realistic stent-based drug delivery. The release kinetics of the marker drug from the model coating are characterized, as are the subsequent convective and diffusive mass transport properties through both the working solution and mimic tissue.

Results take the form of real-time experimental images of spatial drug distribution maps and are compared, qualitatively, with published computational and ex-vivo data. Insight gained from this spatial maps of drug will allow us to appreciate the effects of local hemodynamics on stent based drug delivery.

It was the aim of this chapter to create a dynamically system that replicates the initial mechanisms of drug delivery following implantation of a DES, so that sensitivities to the flow field could be determined. Thus transport processes subsequent to the initial convective/diffusion of drug in the tissue, such as drug interaction with tissue factors, while important to actual stent based delivery, are beyond the scope of the experiment.

4.2. MATERIALS AND METHODS

4.2.1. IN-VITRO PREPARATION

The vessel model, as shown in exploded view in Figure 3-1 (Chapter 3), consists of an acrylic channel containing a hydrogel and polyurethane strip loaded with a fluorescent marker, all in a sealed arrangement. The piston pump with a working fluid of diluted glycerin solution was able to produce pulsatile waveforms through the vessel, and the resulting spatial map of fluorescently labelled drug was visualized using an epi-fluorescence microscope (Figure 3-1b). The working fluid, the channel, the stent strut and the experimental method are explained in full in Chapter 3.

Two strut cross sections were employed, 0.35 mm X 0.24 mm and 0.70 mm X 0.12 mm, with aspect ratios $W/H=1.5$ and $W/H=6$, respectively. As discussed in Section 3.2.2.7, techniques employed in the manufacture of the strut prevented cuts smaller than $W=350 \times 10^{-6}$ m, which were slightly larger than typical commercially available drug-eluting strut widths for coronary interventions (100-200 $\times 10^{-6}$ m). While this prevented the manufacture and study of aspect ratio $W/H=1$, it was only our purpose to demonstrate a sensitivity to strut geometry. A full parameterization study of various aspect ratios is saved for a later date.

The inlet flow profile, shown in Figure β -3b, was programmed into the pulsatile flow pump. The waveform was scaled to give a mean channel Reynolds number of $Re_0 = 427$. Reynolds number was varied to $\frac{1}{2}Re_0 = 213$, by changing the steady flow rate Q_{mean} of the instantaneous flow rate, shown in Figure β -3b.

4.2.1.1.1. *Statistics*

All data is presented as means \pm standard error. Statistical analysis was performed using one-way ANOVA, with differences in measured parameters deemed statistically significant when p -value < 0.05 .

4.3. RESULTS

4.3.1. TRANSPORT CHARACTERISTICS

4.3.1.1. **Transport of marker drug through medium**

The diffusivity of FS in the working-fluid (D_{fluid}) and in the PVA-MA hydrogel ($D_{hydrogel}$) was assessed using the “side-bi-side” diffusion cell as shown in

Section 3.2.4.1.1. The concentration in the receptor chamber (normalized to the initial concentration in the donor chamber) is shown over time in Figure 4-1a for the hydrogel, and in Figure 4-1b for the Millipore filter paper. The diffusion through the hydrogel (Figure 4-1a) is shown to increase with time, with only small error in each time measurement. However this was not the case for the diffusion of drug through the filter paper (Figure 4-1b), which showed large standard deviations in the measurements, with this error increasing (in an absolute scale) with experimental time. Indeed due to the large error in the first experiment (Experiment 1, shown in Figure 4-1b), the experiment was repeated (Experiment 2), with results (mean \pm standard deviation) shown. Error was still consistently large in the latter part of the experiment (4-8 hours) for the second experiment. Reasons for this could not be precisely ascertained, however it was suggested that either the pH of the solution or the photostability of the fluorescein was affected during the experiment under basic laboratory conditions (small changes in ambient temperature, change in light intensity). While efforts were made to reduce these effects (using temperature controlled water baths and covering the samples), their contribution to experimental error could not be discounted. Accordingly only those data points taken in the 0-4 hour interval were included in the calculation. The resulting low standard error in the diffusivity calculation justified this assumption.

The *in-vitro* solute transport parameters, D_{fluid} and $D_{hydrogel}$ were calculated as $1.67 \pm 0.51 \times 10^{-11} \text{ m}^2 \text{ s}^{-1}$ and $1.72 \pm 0.36 \times 10^{-11} \text{ m}^2 \text{ s}^{-1}$ respectively. Values were taken once diffusion reached steady-state and before concentration in the receptor cell reached 5% of the initial donor cell concentration, so that a high concentration gradient across the membrane was maintained. Diffusivity was calculated as the average instantaneous

diffusivity of all data points ($n = \#$ of time points \times $\#$ repeats, $n_{hydrogel}=13 \times 3$, $n_{fluid}=[8+11] \times 3$) from eqn. (3-8).

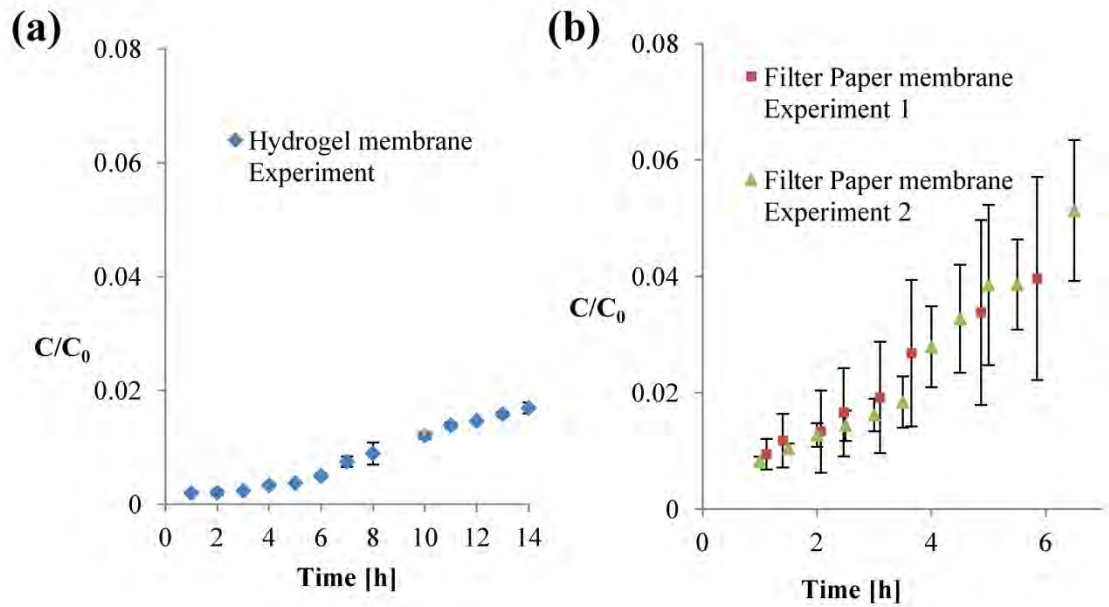


Figure 4-1: Measuring diffusion properties of the system. Concentration of Fluorescein-Sodium, C , in the receptor chamber normalized to initial concentration in the donor chamber, C_0 , at time = 0 shown against time. Results are shown for a) the PVA-MA hydrogel used to measure the diffusivity of FS through the hydrogel (mean \pm sd) and b) the Millipore filter paper membrane used to measure diffusivity of FS in working fluid (mean \pm sd).

4.3.1.2. Release Kinetics of Drug

The drug release of FS from the polyurethane membrane into the working fluid was measured with the “side-bi-side” diffusion cell. Results in Figure 4-2a show an immediate and pronounced burst release of the drug from the surfaces, followed by a steady yet slow release. The rate of release decreases with time since the drug has to traverse length δ to reach the surface. Drug molecules close to the surface will release first, since they have the shortest distance to travel, resulting in a rapid release of the

model drug in the initial stage of the experiment. This release rate tapers off as drug moves through the thickness. The slow release over this time period indicates the polymer matrix amorphous structure creates the necessary impedance for the solute for a sustained and controlled release, similar to that in stent based drug delivery.

This burst release, however, typical for most polymers, is undesirable when a controlled release is required over the short temporal window of the *in-vitro* experiment. The release experiment was repeated (Figure 4-2b), this time determining the effects of casting morphology on release. This was achieved by comparing relative release from the sides exposed to the atmosphere (“top”) during the casting process and those on the underside (“bottom”) that was in contact with the mould wall. Results showed that release from this “top” surface was faster, than that released from the “bottom” surface. This most likely indicates a larger aggregation of drug marker on this top surface, as a result of particles gravitating to the side of the film exposed to the atmosphere during casting, in this case the “top” surface. This variable burst release explains the large amount of error in those results in Figure 4-2a.

When a controlled release is required over the short temporal window this asymmetric burst release on account of casting morphology is not desirable. To negate the effects of the burst release of drug, the strut is pre-soaked for 30 minutes prior to implantation, the resulting release profile is shown in Figure 4-3a. The release profile of the marker drug is shown to be slow but controlled over time, as well as decreasing with a rate that is diminishing with time. Figure 4-3b shows the release profile against the square root of time. The diffusion coefficient is determined from the slope of the linear regression line

fit to the data points ($n = \#$ of time points \times $\#$ repeats, $n_{coating}=7 \times 6$) and substituted into eqn. (3-9) yielding a single diffusivity value of $2.83 \pm 0.04 \times 10^{-16} \text{ m}^2 \text{ s}^{-1}$.

This release coefficient, $D_{coating}$, is of similar magnitude to those reported in stent based drug delivery [89, 117], yielding a realistic release over the three hour experimental time period. Furthermore the small standard error indicates this marker drug release is relatively consistent, for this drug loading/polymer combination.

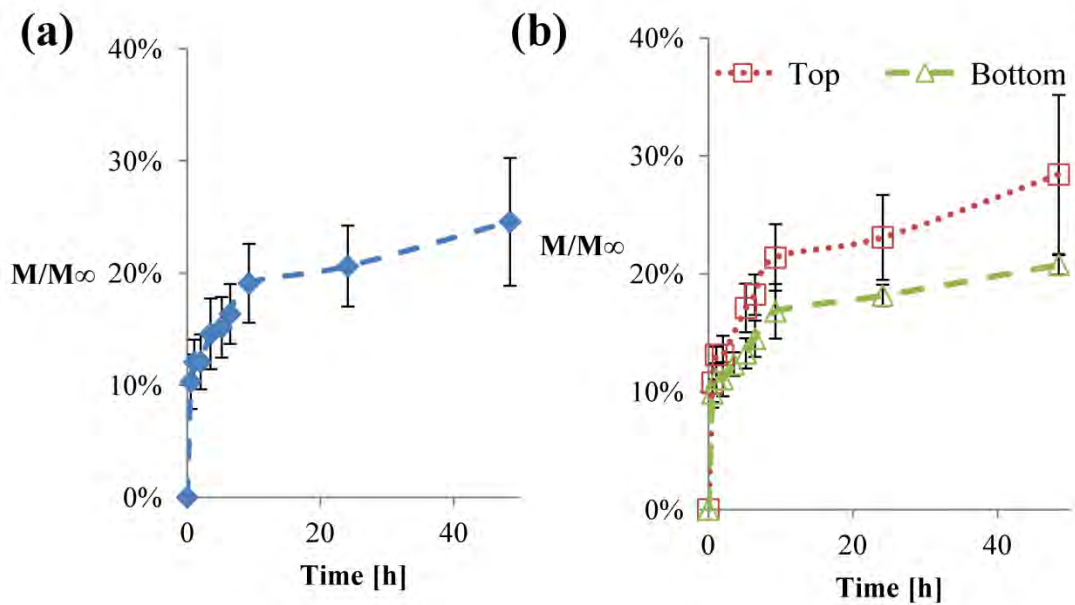


Figure 4-2: Measuring drug release from the polyurethane membrane. a) Cumulative drug released from polyurethane film, M , as a fraction of initial drug loading in the film, M_∞ , (mean \pm sd) over a 50 hour period. b) when the impact of casting morphology is considered, by comparing release

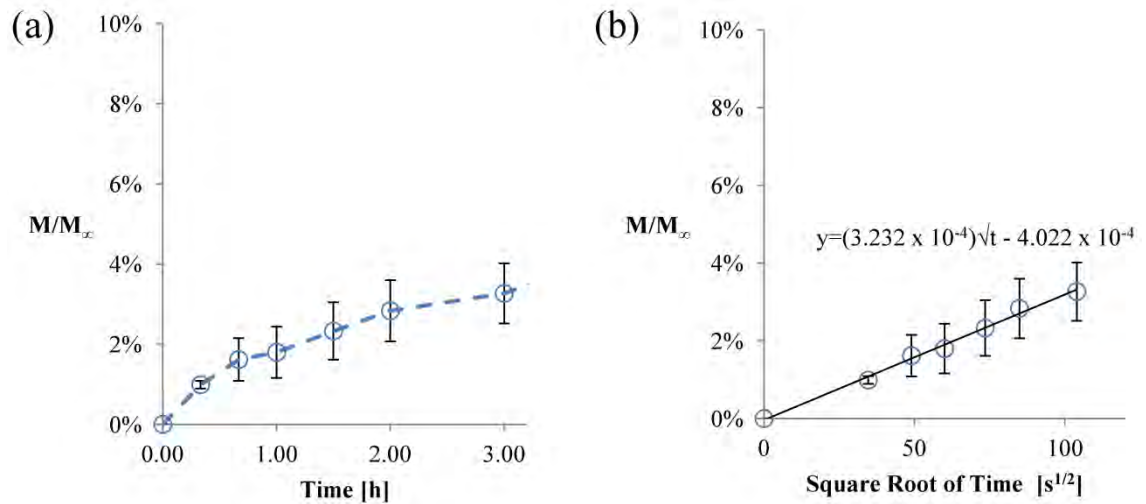


Figure 4-3: Measuring drug release from the polyurethane membrane, after pre-soaking. a) Cumulative drug released from polyurethane film, M , ($n = 6$) (mean \pm sd) as a fraction of initial drug loading in the film, M_∞ , over a 3 hour period and (b) Cumulative drug released ($n = 6$) (mean \pm sd) from the polyurethane film shown against the square root of time. A regression line is fit to all data points, showing a linear relationship with respect to the square root of time, so that the square root of the diffusion coefficient is proportional to the slope of this line eqn. (3-9).

4.4. *IN-VITRO* RESULTS

To confirm computational findings that marker drug deposition is sensitive to the flow field surrounding the stent strut, experiments were performed using the bench-top model. To enable drug penetration depth and spatial distribution to be visualized, images were taken of the longitudinal surface plane of the hydrogel (Figure 4-4a) and also from a cross-sectional cut through the hydrogel (Figure 4-5).

Figure 4-4a shows a longitudinal image of fluorescence at time point 180 minutes, for a flow rate corresponding to $\frac{1}{2}Re_0$. Drug is shown to accumulate in a roughly parabolic shape across the channel (along the y -axis); with larger accumulation in the near wall regions ($y = \pm 1\text{mm}$) and less in the centre ($y = 0\text{mm}$). This is confirmed quantitatively in

Figure 4-4b where a polynomial least squares fit of order 2 is shown to fit the mean concentration data ($n=3$), measured as the average concentration at locations along a line parallel to the y-axis immediately upstream (proximal) and downstream (distal) of the strut.

Figure 4-4b also shows that concentration immediately upstream (proximal) of the strut is larger than that immediately downstream (distal); this difference however did not reach statistical significance.

The disruption to the flow field imposed by the strut was expected to be determined by the strut geometry. A thin, flat strut lying flat against the wall will have minimal protrusion into the flow, while a narrower but taller one will protrude more but will have less contact area with the wall. By comparing these two aspect ratios, the non-contact or convection mediated transport, was differentiated from that resulting from contact-only, and therefore diffusion only processes. The narrow (aspect ratio $W/H = 1.5$) strut was considered equivalent in size to two struts of size $0.35\text{mm} \times 0.12\text{mm}$ that are “stacked”, whereas, the wide strut (aspect ratio $W/H=6$) was equivalent to these same two struts positioned “side-by-side”, as depicted in Figure 4-6a.

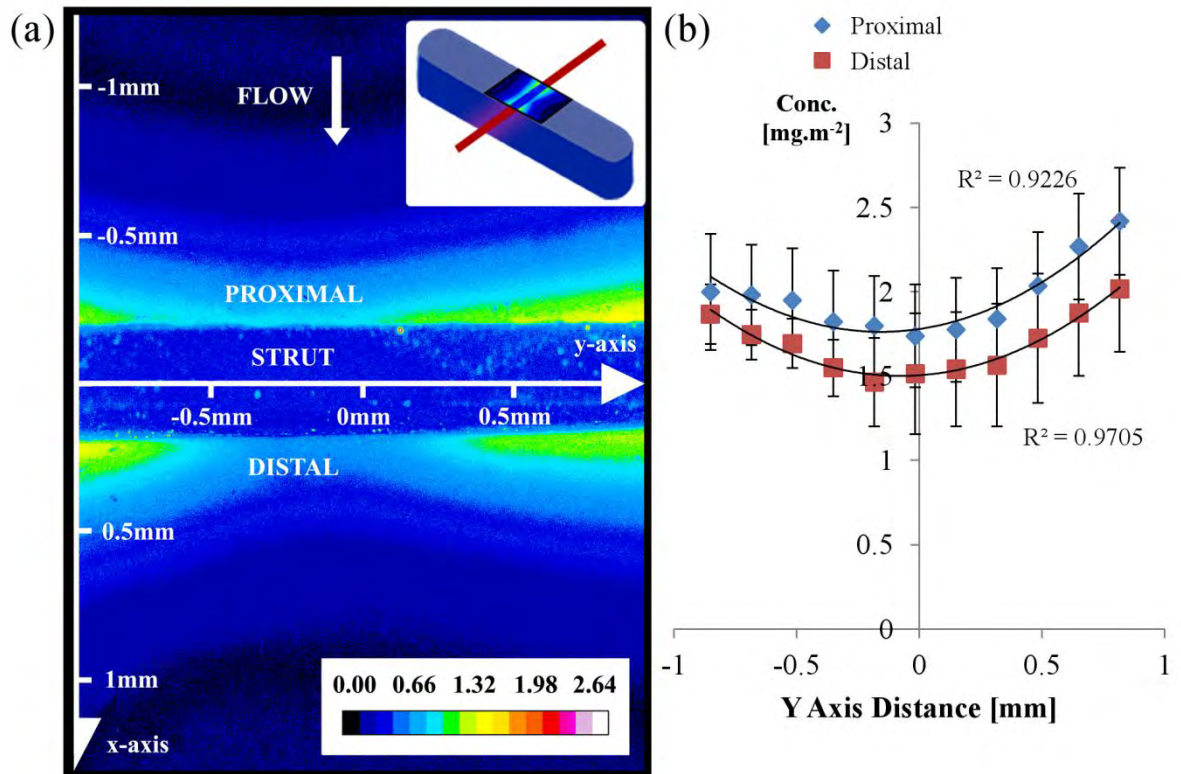


Figure 4-4: Spatial map of marker drug on the surface of hydrogel. (a) Longitudinal images of drug accumulation on the surface of the hydrogel (that surface exposed to the flow and strut domains, the plane $z = 0\text{mm}$), for a single experiment ($n=1$), at 180 minutes. Schematic of section taken is shown inset and concentration is shown in $\text{mg}\cdot\text{m}^{-2}$. (b) Concentration ($n=3$) (mean \pm sd) at points immediately ($\pm 0.01\text{mm}$) upstream (proximal) and downstream (distal) of the strut along the y-axis (across the channel) on the surface of the hydrogel ($z=0$), shows a higher concentration in the proximal region. A polynomial relationship of order 2 was fit to the data points using a least-squares method. R² values are also shown indicating a goodness of fit model. Shown for a Reynolds number of $\frac{1}{2}\text{Re}_0$, with flow acting in the positive x-direction.

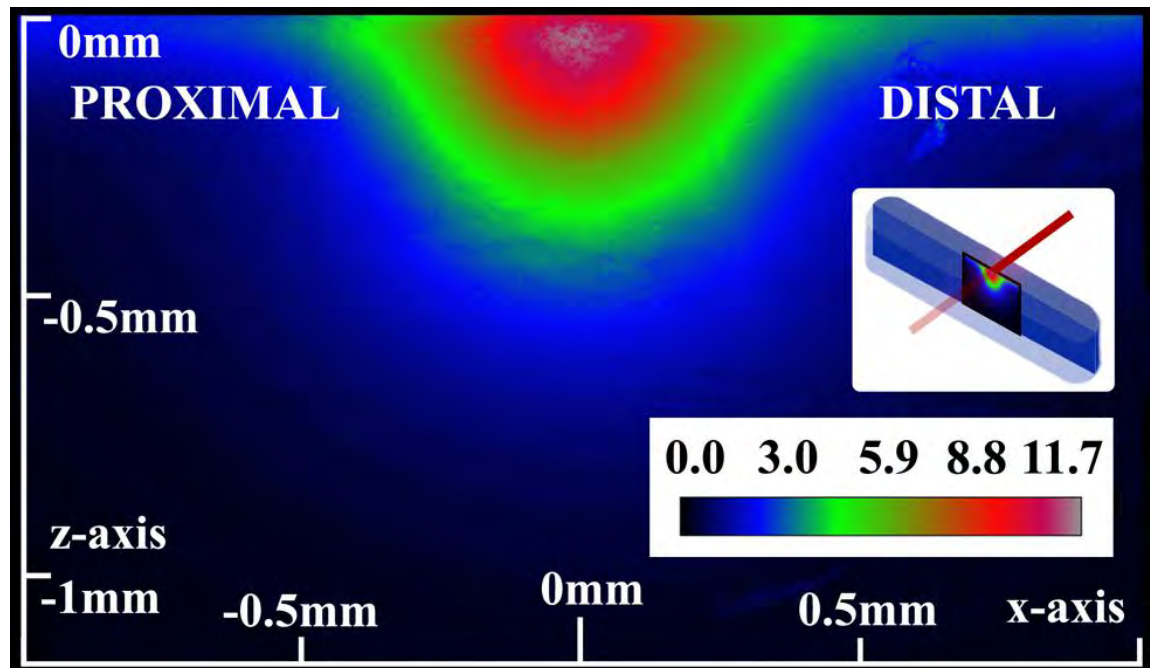


Figure 4-5: Spatial map of marker drug through the cross-section. Cross-sectional images of hydrogel (taken of the plane $x = 0\text{mm}$) at 180 minutes, for an aspect ratio of $W/H=1.5$ (stacked struts). Concentration is shown in mg m^{-1} . Note the surface of the hydrogel exposed to flow domain, occurs at $z=0$.

Spatial concentration measured along a line approximately 0.5mm from the lumen surface for the two cases is shown in Figure 4-6a, and on a logarithmic scale in Figure 4-6b. In both strut configurations, concentration is shown to be larger in the centre and decaying as it moves away from the centre of the strut. Peak concentrations are shown to be similar in magnitude, reflecting deposition as a result of the contact surface; however variations are seen between the two cases away from strut centre. The side-by-side stent strut (aspect ratio of 6) shows a slightly wider, more symmetric distribution of drug. While in the stacked case, there was an asymmetry between the proximal and distal aspects, with concentration found to be 50% ($\pm 10\%$) higher at a point $x =$

+0.9mm about the centre compared to the same point at $x = -0.9\text{mm}$, and thus a distribution that is skewed towards the downstream direction.

The sensitivity of this deposition to the magnitude of flow was also measured, with Figure 4-7 showing area-weighted average concentration decreased with an increase in mean Reynolds number. This difference, though, did not reach statistical significance ($p\text{-value} = 0.18 > 0.05$).

4.5. DISCUSSION

In this chapter a novel bench-top model has been proposed that simulates realistic dynamic behaviour of stent based drug delivery.

Firstly an inhomogeneous distribution of marker drug was observed in the hydrogel, with large concentration gradients observed immediately underlying the strut (Figure 4-5). This variability in tissue drug distribution, in particular the peaks in concentration immediately below the strut decaying with distance from the centre, is consistent with those experimentally-determined results from Hwang et al. [83], indicating that we are in fact accurately representing those initial mechanisms of drug transport following stent placement, as would occur in-vivo

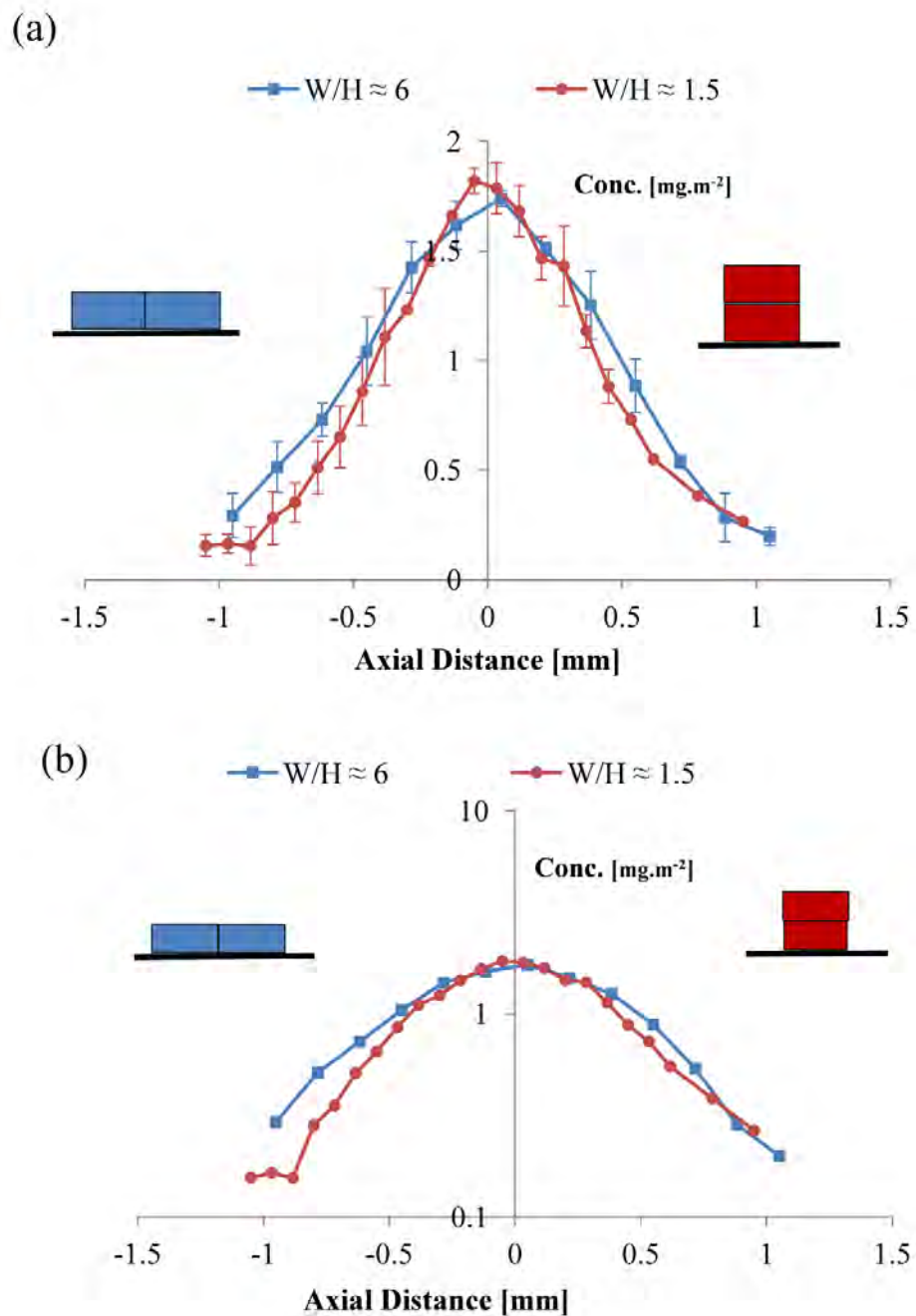


Figure 4-6: Measured spatial marker map drug distribution. (a) Spatial distribution of the drug at a distance approximately 0.5mm into the depth of the hydrogel, for two different aspect ratios $W/H=6$ and $W/H=1.5$, equivalent in size to two struts “side-by-side” or “stacked”. Image has been calibrated to a known 2D concentration, with appropriate length scales. Concentration (mean \pm sd) are shown for a Reynolds number of $Re_0=427$. (b) Concentration (mean), same data as that from (a) plotted on a logarithmic scale.

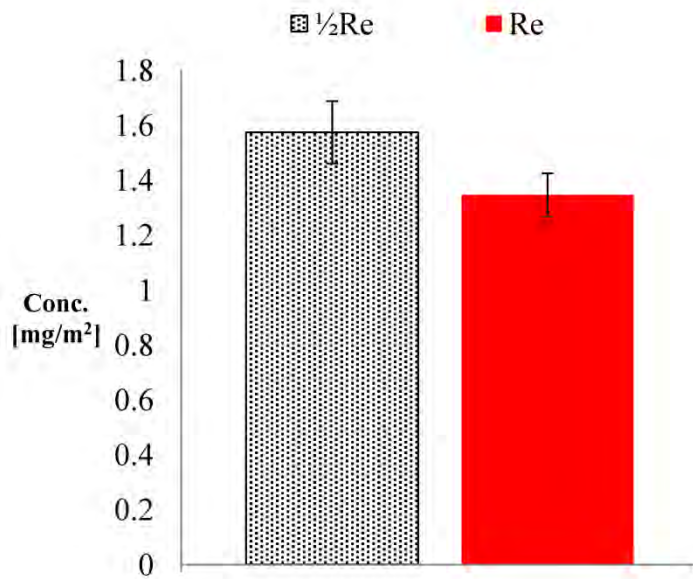


Figure 4-7: Mean concentration in the hydrogel bed, for varying Reynolds number $\frac{1}{2}Re_0$ and Re_0 , shown for an aspect ratio of $W/H=1.5$.

Furthermore it was the aim of this study to determine whether arterial drug deposition was sensitive to strut geometry, flow magnitude and its direction, and in doing so either confirm or negate those earlier findings in simplified computational models of DES by Kolachalama et al. [90] and Balakrishnan et al. [89].

In their 2D computational model of a single drug-eluting stent Kolachalama et al. [90] demonstrated that flow over a lumenally protruding strut, created regions of flow stasis proximal and distal to the strut (shown in Figure 1-5a). Correspondingly, in Figure 1-5b the authors demonstrated that drug is able to pool in these regions, both elevating the concentration and locally extending the pattern of drug in the underlying tissue. There is a complex interplay though, between size of the recirculating region and the extent and magnitude of the mural footprint of drug.

In particular the authors were able to show that, for a positively directed flow, the distribution of drug was skewed towards the downstream (distal aspect) (Figure 4-5b). This was a result of a larger recirculation zone in the distal aspect, extending drug far downstream of the strut. At the same time, because of a larger recirculating region in the distal aspect, mural concentration was diluted (on account of larger volume of fluid). The net result was a distribution of drug in the distal aspect that extended further but was smaller in magnitude, than that in the proximal tissue. An increase in the mean flow rate was shown to decrease total drug uptake in the tissue below, by increasing the dimensions of the recirculating flow regions and thus diluting the pooling surface concentrations.

In our 3D bench-top reconstruction of a single strut residing in axially aligned flow, the pattern of drug distribution in the hydrogel was, indeed, shown to be dependent on the flow field surrounding the strut.

First we saw a sensitivity in spatially distributed drug to the local flow magnitude across the channel (y-axis in Figure 4-4a). It is suggested that this is a result of the differential size of strut-induced recirculating flow across the channel. Due to the parabolic velocity magnitude found across a square based channel [130], the dimensions of the recirculating flow regions adjacent to the strut will decrease with distance away from the centreline. Neglecting drug transport in the y-direction, drug will be able to pool to a much higher concentration in a smaller recirculating flow region (as in the near wall), compared to a larger recirculating flow (as in the centreline), which will act to dilute the pooling drug. We posit, that it was because of those elevated surface concentration in

the near wall regions, when compared to the centreline, that a roughly parabolic footprint of marker drug in the hydrogel below was observed (Figure 4-4b).

At the same time we observed a sensitivity in marker drug deposition to the direction of flow. Figure 4-4b shows that peak concentration on the tissue surface (measured at a point in immediate proximity of the strut) to be larger in the proximal region than in the distal. We suggest that this asymmetry in distributed drug is a result of those asymmetrically sized proximal and distal recirculating regions. As long as flow is forward moving, the proximal recirculating flow region will be smaller than that in the distal aspect. For an equivalent amount of drug released from the coating into these regions, drug will be able to pool to a much higher concentration in the smaller proximal volume. Correspondingly the surface concentrations in the proximal regions will be higher than in the distal, leading to higher concentrations in the underlying hydrogel.

Furthermore this sensitivity to direction was observed in the cross-sectional concentration profile for a strut of aspect ratio $W/H=1.5$, with the distribution of marker drug in Figure 4-6a shown to be skewed towards the distal end. While this difference between proximal and distal aspects was small and best appreciated in a logarithmic scale (Figure 4-6b), it does follow those findings by Balakrishnan et al. [89] and Kolachalama et al. [90], shown in Figure 1-6 (in yellow) and Figure 1-5b, respectively.

We also observed a sensitivity in mean drug uptake into the hydrogel to the net channel flow rate. In particular an inverse relationship between drug uptake and vessel flow rate (Figure 4-7) was revealed, similar to that trend found by Kolachalama et al. [90].

Importantly though the degree to which these flow characteristics modulate drug uptake was found to be dependent on the strut geometry. The side-by-side strut has twice the contact area with the hydrogel as that of the stacked strut, and if a diffusion-only transport model was considered, it would be expected that the side-by-side struts would have a distribution effectively twice as wide as the stacked case. Yet Figure 4-6a showed only a slightly narrower distribution for the stacked case. It is postulated that this is a result of a non-contact mediated mechanism of transport.

Quantitatively more compelling is the asymmetry in FS distribution present in the stacked struts case, (shown in Figure 4-6a, and on a logarithmic scale in Figure 4-6b) compared to the side-by-side struts which produce a more symmetric distribution. This can be understood by considering that two stacked struts pose a larger protrusion into the flow, and thus will create a larger and more intense convective environment surrounding the stent strut. Consequently this geometry will be more sensitive to flow induced asymmetries in drug distribution, than a wider stent strut effectively lying flat against the wall.

Taken together, the results of the *in-vitro* method identify a flow-mediated component that is sensitive to both strut geometry and local flow magnitude and direction. These findings are consistent with computationally determined results presented in literature [83, 89, 90].

Indeed this is the first bench-top method of its kind. While Seidlitz et al. have created a complex multi-compartment model simulating drug release and transport [97], they have been unable to characterize those local concentration gradients following stent placement [83], or demonstrate a sensitivity to flow conditions.

Creating such a bench-top model in which to test flow sensitivities is complex. To accurately characterize the flow mediated contribution of drug deposition from a stent strut, the *in-vitro* system requires high resolution and precision while also being physiologically relevant. Firstly, the anticipated results only differ minimally with variation in the key parameter Reynolds number, as shown by the logarithmic scale used for the concentration fields in the computational results [90], so the system will be required to be able to capture that sensitivity while also being repeatable. Secondly, the temporal window in which to visualize these transport forces is limited in a non-biological environment and thirdly the results must also resemble those in physiologically realistic stent-based drug delivery, so that key transport properties must also match those in-vivo.

Pulsatile flow waveforms were created using the piston pump with flow rates scaled to match instantaneous Reynolds number typical for arterial flow, with a cycle frequency of 1 Hz, resulting in a Womersley number ≈ 2 , typical for a coronary vessel.

Fluorescein Sodium (FS) was selected to mimic anti-proliferative drugs due to its similar molecular size and hydrophilic properties, making it compatible with the PVA-MA hydrogel. The diffusion coefficients of FS in the hydrogel and working fluid were determined to be relatively similar in magnitude, indicating that the hydrogel offered

little barrier to diffusion like that determined *in-vivo* with Paclitaxel [83, 115]. Despite this, their relative magnitudes at experimental conditions indicate they do match the time scale of the diffusion processes in actual stent-based drug delivery. Specifically while FS diffuses readily in water ($4.25 \times 10^{-10} \text{ m}^2 \text{ s}^{-1}$) [138], diffusivity of FS in the glycerin-water solution controlled at 23°C was found to be similar in magnitude to the diffusivity of Paclitaxel in blood at 37°C ($3.89 \times 10^{-11} \text{ m}^2 \text{ s}^{-1}$) [115] and differing only by an order of magnitude to that of Paclitaxel in tissue ($3.65 \times 10^{-12} \text{ m}^2 \text{ s}^{-1}$) [83].

Importantly the hydrogel used offered no binding sites like arterial tissue does, so highly diffusible drugs like Fluorescein Sodium will rapidly diffuse through the medium. Consequently for this *in-vitro* experiment there was a limited timeframe in which to capture the behaviours found in Paclitaxel tissue distribution *in-vivo* and *ex-vivo*, namely the local concentration gradients [83] and flow-mediated spatial asymmetry [89, 90], before the hydrogel is uniformly inundated with drug. This study was limited to 3 hours to capture the initial mechanisms of drug transport, specifically those due to diffusive and convective forces. This also ensures subsequent mechanisms such as molecular interactions of the tissue as would occur *in-vivo* are not misrepresented. Additionally, the short time frame guaranteed a constant concentration gradient over the depth of the hydrogel.

The transient spatial distribution of drug is also intrinsically related to the release kinetics of the drug from the polyurethane strut. DES are designed so that the rate of release of antiproliferative drug is controlled via mechanisms of diffusion, degradation or swelling followed by diffusion [79] in the coating membrane. In order to match the

temporal sequence of the development of neo-intimal hyperplasia, drug-eluting stent coatings are designed to release antiproliferative drug over days to months following implantation. In this experiment, the release of Fluorescein-Sodium (1% wt/wt) from a polyurethane film into the working solution held at 23⁰C, was found to have been sustained and controlled over the 3 hour experimental time, consistent with release from a diffusion controlled membrane [79] and with a release coefficient, $D_{coating}$, of similar magnitude to those reported in stent based drug delivery [81, 117].

In conclusion the bench-top experiment has provided qualitatively equivalent results to computationally determined results in literature. While quantitative comparisons between the *in-vitro* method and an equivalent computational model are attractive, several limitations prevented a full quantitative comparison. Firstly a steady-state distribution would take months to realize, and involves many more events beyond the scope of a bench-top model. At the same time limitations of computational power meant that a full transient model was not possible, since a realistic time period of simulation was truncated far premature of the *in-vitro* endpoint.

4.6. CONCLUSION

In summary, the *in-vitro* model has been demonstrated to be an effective method in which to validate the existence and significance of flow-mediated deposition in local drug delivery elucidated in previously reported computational models. The results confirm the existence of a flow-mediated component in stent-based drug delivery, one that is sensitive to flow magnitude, direction and strut geometry. By incorporating a transport environment that is similar to that determined from *in-vivo* studies, it provides

a platform in which to assess the mechanistic functions governing actual stent based drug delivery.

CHAPTER 5. IMPACT OF FLOW PULSATILITY ON ARTERIAL DRUG DEPOSITION

Drug-eluting stents reside in a dynamic fluid environment where the extent by which drugs are distributed within the arterial wall is critically modulated by the blood flowing through the arterial lumen. Yet several factors associated with the pulsatile nature of blood flow and their impact on arterial drug deposition are not completely understood. In this Chapter we use an integrated framework comprising computational and bench-top models to explore the physical and physiological factors characterizing the time-varying fluid dynamic environment within the vasculature, and their effects on arterial drug distribution.

5.1. INTRODUCTION

As the impact of luminal flow on arterial drug uptake is being increasingly characterized, several aspects associated with blood flow need to be understood. In particular, the time-varying patterns of blood flow caused by the cardiac pulse creates a time-varying (or unsteady flow) environment that in turn may influence the overall arterial drug distribution patterns.

In both Chapters 1 and 4 it was described how luminally protruding stent struts create flow recirculating regions. Drug released from the abluminal surfaces create standing drug rich recirculation zones upstream and downstream of the strut. These act as secondary sources of drug uptake for the underlying tissue. From Chapter 4, it is now known that flow-mediated drug uptake is dependent on the net luminal flow, governed by the mean Reynolds number. However the mechanism by which parameters

governing unsteady flow modulate arterial distribution, are not completely characterized.

In his 1955 paper, J. R. Womersley numerically derived a solution to the unsteady flow harmonics for oscillatory flow in a straight rigid vessel [101]. As part of this solution, a dimensionless parameter denoted as the Womersley number was introduced as a function of vessel radius, flow frequency and the kinematic blood viscosity. The Womersley number provides a qualitative description of the unsteady forces governing luminal blood flow, that in turn are determined from the frequency and magnitude of the driving pressure gradient. Given that the transient arterial pressure gradient and the associated fluid flow are dynamically changing and vascular-bed dependent, the question arises as to whether the parameters governing flow pulsatility affect arterial drug distribution patterns and if so how they can be systematically quantified.

This chapter begins with an introduction to the fluid dynamics of pulsatile flow, including the physical and physiological significance of the Womersley number. Inferences derived by applying Womersley's analytic framework allowed us to derive appropriate parameters for performing computer simulations of pulsatile flow coupled with drug transport, and appreciate a vascular-bed dependent variation in blood flow. Using an integrated framework of a coupled computational fluid dynamics and mass transfer model, along with the bench-top method described in Chapter 3, the factors governing flow pulsatility in model vascular beds were explored and their effects on arterial drug distribution patterns for several deployment settings were investigated.

5.2. BACKGROUND

5.2.1. FLUID DYNAMICS OF PULSATILE FLOW

The pulsatile nature of cardiac ejection results in dynamically changing blood flow through individual vascular beds. Numerically, time-varying luminal flow is expressed as the sum of its steady component and its oscillating (unsteady) Fourier harmonics [101].

$$Q(t) = Q_{mean} + \sum_{n=1}^N Q_n(t) \quad (5-1)$$

Womersley provided an analytical solution for the n^{th} harmonic of oscillating laminar flow through a straight, rigid pipe given a complex oscillating pressure gradient $A_n e^{i\omega t}$ [101]:

$$Q_n(t) = \text{Real} \left\{ \frac{\pi R^2}{i\omega\rho} \left(1 - \frac{2}{\alpha i^{3/2}} \frac{J_1(\alpha i^{3/2})}{J_0(\alpha i^{3/2})} \right) A_n e^{i\omega t} \right\}. \quad (5-2)$$

J_0, J_1 are, respectively, the zero and first order Bessel functions of the first kind. R is the radius of the vessel and ρ is the density. Angular frequency is given as, $\omega = 2\pi n f$, where f is the frequency of the n^{th} harmonic. As part of this solution, a dimensionless frequency parameter (α), now referred to as the Womersley Number was introduced, such that $\alpha = R \sqrt{\frac{\omega}{\nu}}$, where ν is the kinematic viscosity. The Womersley number describes the relative amounts of transient inertial and viscous forces, thus representing

a measure of the unsteady forces in a flow field. When $\alpha \approx 0$, the flow is quasi steady and thus the instantaneous flow rate can be determined from the applied pressure gradient. As the Womersley number is increased, transient inertial forces begin to dominate aspects of flow that resist changes in velocity and act to dampen the instantaneous flow magnitude and increase the phase lag between pressure and flow (eqn. (5-2)). Specifically as α is increased beyond 4 in eqn. (5-2), these transient inertial effects are sufficiently large that the phase difference between pressure and flow waveforms increases to more than 60° .

This phase lag is illustrated in a physiologically realistic example of flow through the renal artery. Figure 5-1 shows the renal arterial waveform, with $\alpha \approx 4$, is out of phase with the driving pressure gradient, with peak flow rates lagging peak systolic pressure (See Appendix 3 for details of the derivation of the pressure gradient from flow data).

Assuming viscosity is fixed, vascular bed-derived variations in the Womersley number occur via changes in the frequency of the oscillating pressure gradient or the vessel size.

Figure 5-2a shows that as α increases with frequency, the amplitude of the unsteady flow rate ($Q(t)/Q_{\text{mean}}$) decreases and thus the unsteadiness of the flow decreases as well. A large α implies a large inertially-driven flow, and so as frequency of the pressure gradient increases, accelerating the inertia is made more difficult. Increasing frequency and thus α from the nominal renal arterial case shows an instantaneous flow that has a significantly damped oscillating flow rate. This implies that in this case high α reflects a fluid mechanic effect that can serve as a close approximation to steady

luminal flow (Figure 5-2b). By decreasing α from the nominal renal arterial case via this frequency change, the flow becomes highly viscous with large changes in amplitude, including periods of reverse flow as the flow moves in phase with the instantaneous pressure gradient (Figure 5-2b).

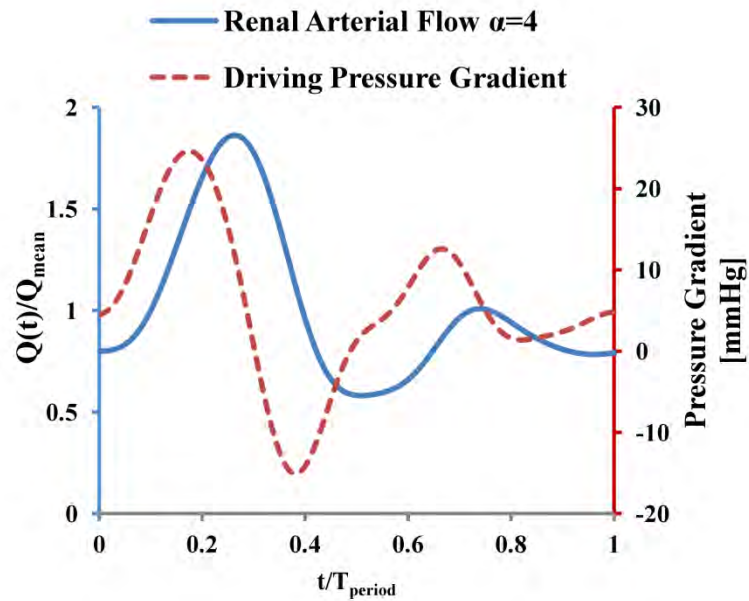


Figure 5-1: Nominal pressure gradient derived from renal flow rate waveform data using Womersley’s framework. Derivation is shown in Appendix 3.

A change in α due to a change in the radius (vessel size) results in a more complex fluid mechanical effect. Specifically as α increases with radius, the time varying flow rate as defined by Womersley, monotonically increases as well (Figure 5-2a). Critically, though, by increasing radius we are also increasing the Reynolds number of the vessel which can affect both the steady and unsteady components of the flow. Indeed then increasing the radius in eqn. (5-2) reflects a contrived case (Figure 5-2a). To illustrate a change in vessel size in a physiologically realistic setting, we present the

case of two vessels located in close proximity: the renal artery ($R = 3$ mm) which branches off the suprarenal aorta ($R = 10.5$ mm), where basal Womersley numbers ($f = 1$ Hz) are approximately 4 and 16, respectively. Despite variations in the size of α in both branches, high peripheral resistance during rest [99] diverts a large volume of cardiac output through the renal branch, so that their unsteady flow rates, $Q(t)/Q_{\text{mean}}$, are similar in shape and magnitude [99, 132, 139]. This will not be the case for a change in a vascular bed to a more remote location. Whilst a constant pressure can be assumed across bifurcations of large arteries [140, 141], like the aorta-renal bifurcation, this pressure gradient will change in both shape and magnitude with movement through the arterial tree, giving rise to completely distinct and dissimilar flow waveforms altogether. This highlights the complexity involved with systematically varying the Womersley parameter in a way that is both mathematically complete and physiologically realistic.

The variable α also denotes the degree of deviation from a Poiseuille velocity profile. For flows that are considered steady and viscous, the Navier-Stokes equations can be simplified to yield a Poiseuille velocity solution. However, flow never truly realizes a steady state condition, since Poiseuille steady flow ($\alpha \rightarrow 0$) represents an asymptotic process. Alternatively, for pulsatile flows, the boundary layer thickness (δ), and therefore the vessel's fully developed profile is a function of α such that oscillating boundary layer length of each harmonic is given as $\delta = R/\alpha$. For very low frequency and thus at approximately steady flows ($\alpha < 1$), Stokes' boundary layer thickness for the fundamental harmonic still exceeds the radius of the vessel and hence extends beyond the flow centreline. Even under these conditions, the Poiseuille solution is valid. However, for fully developed pulsatile flow with $\alpha > 1$, the viscous boundary layer of

the fundamental harmonic is smaller than the radius, so that an inviscid core flow develops which exhibits characteristics that are blunt or plug-like. This boundary layer thickness decreases with increasing α , such that the flow becomes more inviscid and consequently can no longer be solved analytically.

Changing α via either vessel size or frequency will give rise to disparate flow profiles across the vessel. This was investigated by simulating typical pulsatile renal arterial flow in a straight channel (no-slip walls), under varying conditions of flow frequency and vessel dimensions. For the nominal case of renal arterial flow ($\alpha \approx 4$, Figure 5-2a) Figure 5-3a shows that the resulting instantaneous velocity profile is indeed not Poiseuille parabolic, but rather has more of a blunt shape as the viscous boundary layer decreases in thickness, leaving a large inviscid region moving through the centreline of the vessel. For a decrease in α as a result of frequency change (Figure 5-3b), the unsteady boundary layer is made larger with flow becoming entirely viscous. Velocity profiles vary significantly at each time point, with periods of reverse flow during systole. The magnitude of these variations in the centreline flow is consistent with large changes in the instantaneous flow rate.

By increasing the frequency so that $\alpha \approx 16$ (Figure 5-3c), viscous effects are now restricted to a significantly smaller viscous boundary layer. Profiles are blunt through the middle of the vessel (centreline velocity ≈ 1.2) and vary little over the cycle, reflecting only a small magnitude in the oscillations about the mean flow rate. Considering now the flow-field in the aorta (Figure 5-3d), while the Womersley number is still 16, the comparatively large amplitude in the time-varying flow rate implies that

the flow fields vary significantly to that of the case shown in Figure 5-3c. While the boundary layer thickness remains small compared to the radius, so that the inviscid core flow is blunt, there is significantly large shear in the near wall viscous region following the periodic deceleration and acceleration of the vessel flow rate. In particular we see during systole ($0.45T_{\text{period}}$) that the faster decelerating convective flow in the boundary layer separates and breaks away, resulting in periodic reverse flow in the near wall, while that in the centreline remains positive.

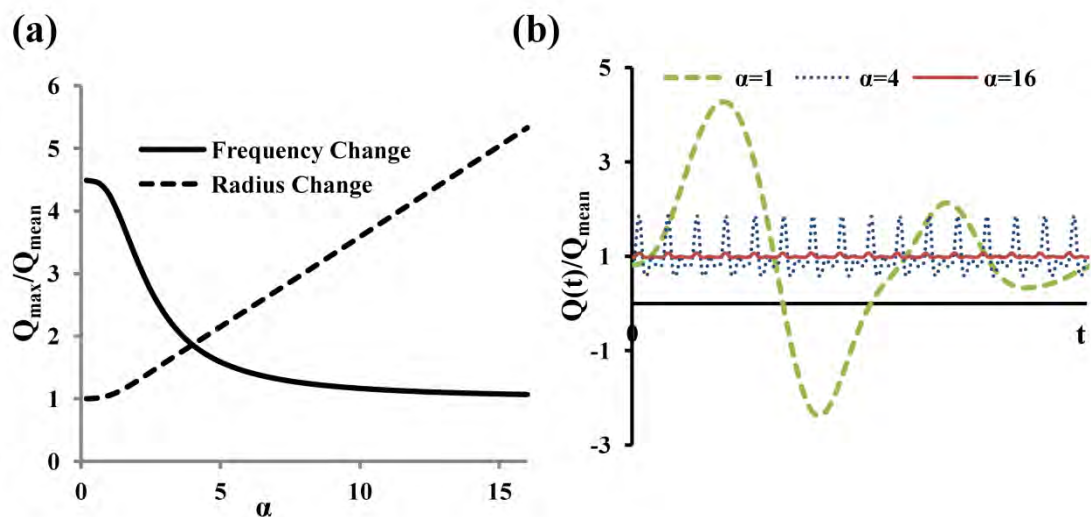


Figure 5-2: Effects of Womersley number on different flow regimes. a) The amplitude of the pulsatile waveform, measured as the maximum instantaneous flow rate in each cycle [$\text{Max}(Q(t))$] as a fraction of the mean flow component Q_{mean} , changes as a result of changing α by either varying frequency or radius in equation (5-2). Because a change in anatomical position is coupled with a change in the amplitude of the pressure gradient, the relationship with radius represents a contrived case. (b) Flow waveforms as a result of varying α via frequency of pressure gradient in equation (5-2). Nominal case is shown for the renal artery [132]. As α increases from the nominal case, unsteadiness decreases while a decrease in α acts to increase the amplitude of the unsteady component of flow

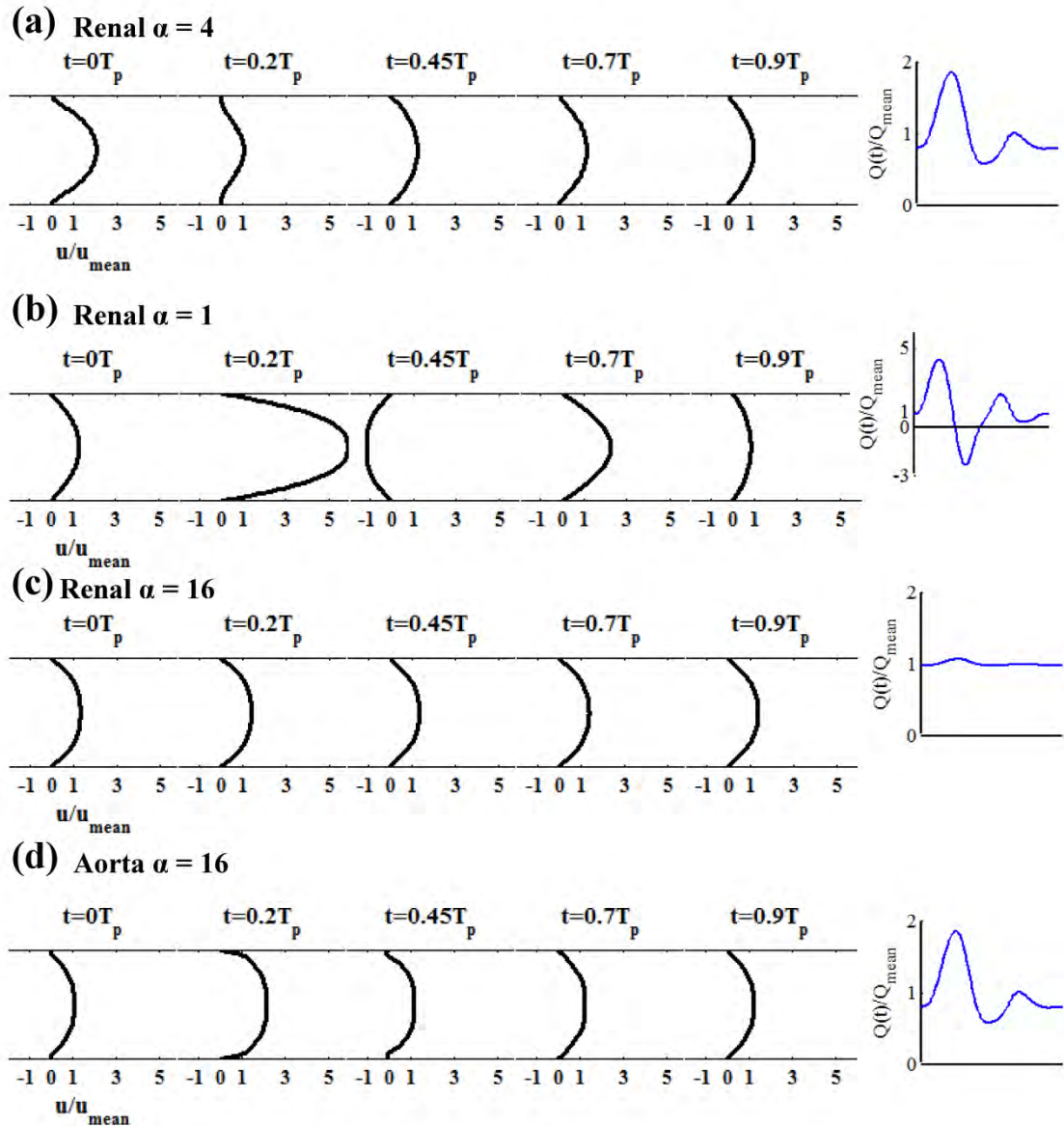


Figure 5-3: Effect of a change in the Womersley number on the velocity profiles, for a prescribed individual flow waveforms for one time period (T_{period}) (shown on the right of each sub-plot). a) Renal velocity profiles scaled to a mean velocity component presented in literature [98], results in the nominal case with $Re=427$ and $\alpha=4$. The velocity profiles as a result of varying frequency of the pressure waveform in eqn. (5-2) to b) $\alpha=1$ and c) $\alpha=16$. d) Flow field for suprarenal aortic flow ($\alpha=16$) (Radius of 10.5mm) [98], that is scaled to provide a mean Reynolds number of 427.

5.2.2. RELEVANT PARAMETERS GOVERNING PULSATILITY AROUND A STENT STRUT

Large changes in the dynamic flow field associated with a change in the vessel α will be significant to a stent strut residing in the boundary layer of the flow. In determining to what extent these dynamic changes in the flow field affect mass transport from a stent strut, it will be necessary to derive those parameters that represent the unsteadiness of the flow environment surrounding the strut.

Physically, a stent strut represents a surface-mounted obstruction to the boundary layer of a vessel, and flow over this barrier separates at a point upstream and reattaches downstream, creating two pockets of recirculating flow proximal and distal to the strut (Figure 11-5a). Under a pulsatile arterial flow regime, the instantaneous size of these regions will be governed by geometric and local dynamic flow parameters based on the characteristic length scale of the strut height (S_H). Locally, Reynolds and Womersley numbers are expressed in terms of this length such that $Re_L = \frac{S_H V}{\nu}$ and $\alpha_L = S_H \sqrt{\frac{\omega}{\nu}}$, respectively, where V is the characteristic flow velocity.

Changes in the local dynamic flow field are derived from dynamic changes in the greater vascular flow. However critically, these physical parameters are in turn derived from the physiological pressure-flow relations defined by Womersley; in the previous section we have demonstrated that changes in the dynamic flow field in a rigid pipe are a result of a change in either the frequency of the cardiac pulse or a change in vessel size. Changes in the vessel α , or these local dynamic parameters, α_L and Re_L , on account of these physiological changes are neither intuitive nor independent. First we have demonstrated how a change in vascular bed will act to change both the steady and

unsteady flow magnitude (Figure 5-3d) and therefore describes a change in the local instantaneous Reynolds number Re_L . On the other hand a change in the frequency of the oscillating pressure gradient, ω , will lead to a change in the local Womersley number α_L however it will also be coupled with a change in the unsteady amplitude of the instantaneous velocity (as shown in Figure 5-2b) and thus Re_L .

Alternatively it is proposed that the frequency of the cardiac pressure pulse be used as an index of flow pulsatility; since not only is it both physiologically and physically measurable, but it also fully characterises the extent of unsteady behaviour in the system. Figure 5-2b shows that by changing the frequency from the nominal pressure gradient, both the unsteady magnitude, $Q(t)/Q_{\text{mean}}$, and the time-scale of changes, ω , varies, thus scaling the overall unsteadiness of the system. In particular, it was demonstrated that a low frequency system represents a truly unsteady flow environment with large instantaneous changes in flow, while a system with sufficiently high ω represents a steady fluid mechanic effect.

Simulated unsteady flow profiles were therefore parameterised in terms of cardiac frequency, ω , but characterised in terms of their associated Womersley number, α . A change in the mean flow rate, Q_{mean} , and thus the steady flow field, was described by a change in the mean vessel Reynolds number Re .

5.3. METHODS

5.3.1. NUMERICAL SIMULATIONS

The computational domain (shown in Chapter 2, Figure 2-1) comprised two rectangular channels simulating the arterial lumen and the wall. Arterial wall thickness was prescribed as $A_W = 1\text{mm}$ and the radius of the lumen was set at $R = 3\text{mm}$ for the nominal case of a model renal arterial flow [98]. Both channels were of length $L = 3R$. A single strut of unit aspect ratio ($S_H \times S_H = 0.1 \times 0.1\text{mm}^2$) was placed at the lumen-wall interface. The artery was assumed to be symmetric with respect to a centreline. Blood was modelled as a laminar fluid with a shear-dependent dynamic viscosity, shown in eqn. (2-1), used to systematically account for the non-Newtonian characteristics [93] and a density of 1060 kg/m^3 . Transient luminal blood flow was modeled by utilizing the continuity and momentum relations, in eqn. (2-2) and eqn. (2-3), respectively. The arterial wall was assumed to behave as a homogeneous porous medium. Transport of interstitial fluid was modelled numerically using the continuity equation, eqn. (2-4) as well as Darcy's momentum equation, eqn. (2-5). Darcy's permeability coefficient was assumed to be $K = 1.43 \times 10^{-18}\text{m}^2$ [129].

The scalar transport model in eqn. (2-6) was employed to simulate drug transport, with diffusivities in fluid and tissue set to $D_f = 3.89 \times 10^{-11}\text{ m}^2\text{ s}^{-1}$ and $D_t = 3.68 \times 10^{-12}\text{ m}^2\text{ s}^{-1}$, respectively [83, 90, 115].

At the lumen-tissue and lumen-strut interfaces, a no-slip condition was imposed. Continuity of flux was assumed through the lumen-tissue interface.

Drug release was handled with a Dirichlet boundary condition on the surface of the strut with flux prescribed by Higuchi's model for drug release, shown in eqn. (2-7), with diffusion coefficient prescribed as $D_c = 1 \times 10^{-15} \text{m}^2/\text{s}$ [117]. The Higuchi model assumes a release rate that is constant with respect to the square root of time and is commonly used to describe the initial release of drug from diffusion controlled membranes [118].

The initial concentration was set at unity, $C_0 = 1 \text{ mol/m}^3$. A zero flux boundary condition was prescribed at the tissue upstream and downstream aspects, and perivascular wall aspects. A zero concentration was applied at the inlet.

The sensitivity of arterial drug deposition to the local fluid dynamic parameters, α and Re , was investigated independently by considering physiologically realistic changes in these variables. This was achieved by implementing an inlet velocity boundary condition based on either a frequency change of the pressure gradient using Womersley's framework (eqn. (5-2)) to represent a change in α , or a decrease in the mean flow rate, Q_{mean} , by a nominal factor representing a change in Re . Fully developed transient velocity profiles were derived by letting a time varying plug flow (uniform velocity),

$$\bar{u}(t) = \frac{Q(t)}{\pi R^2} \quad (5-3)$$

to develop over an entrance length. A conservative estimate of the entrance length for the range of α was based on the vessel radius and peak instantaneous Reynolds number

($Re_{max} = 2Ru_m/v$, where u_m is the mean velocity of the cross-section of the channel and v is the kinematic viscosity of blood) [142]. The nominal driving pressure gradient from which the frequency ($\omega = 2\pi f$), and thus α was varied, was derived from literature values for renal artery flow waveform [98, 132] (Figure 5-1a). The cardiac frequency for this nominal case was set to 1Hz. Using this pressure gradient, flow rates ($Q(t)$) were determined for a given frequency (and thus α) and scaled for a mean vessel Reynolds number ($Re = 427$), consistent with flow in a renal vessel [98]. A zero pressure condition was applied at the lumen outlet.

A Streamline Upwind/Petrov-Galerkin method [121] with second order accurate time integration [124], was used to solve for the momentum and mass transport variables using finite element software (COMSOL 4.0a, Comsol Inc.) (See Section 2.5.1). The chosen time step was required to be sufficiently small so that both transient drug release and cyclical changes in flow for each time period were properly resolved (See Appendix 5). The solution was found to be independent of the time-step when Δt was the maximum value of either 0.06 s or $0.05 * T_{period}$.

Iterations at each time-step were performed until there was a 10^{-8} reduction in the relative error. Numerical simulations were run for a total solution time of 50 s regardless of position in cycle. Running the solution any longer would have required in excess of 400 hours of computational wall time (using a shared memory parallel platform, over 8 CPUs), and therefore was considered impractical for a full parameterization study.

A Delaunay triangulation scheme was used to mesh the interior regions of the lumen and the arterial wall, with quadrilateral elements on the domain boundaries and local refinement in areas of expected high concentration gradients. Linear basis functions were assumed for the pressure variable, while for velocity and drug concentration variables quadratic basis functions were used. A solution was determined to be mesh-independent when there was less than 2% change in the Area-Weighted Average Concentration (AWAC) within the tissue at five strut widths either side of the stent strut at a solution time of 50 s, for a further sequential refinement (Appendix 5). The total number of elements that yielded a mesh independent solution, was found 2.8×10^4 , corresponding to 1.12×10^5 degrees of freedom.

5.3.2. IN-VITRO MODEL

The bench-top model described in Chapter 3 (shown in Figure 3-1) was used here. A single strut of cross section 0.35 mm X 0.24 mm, (equivalent to an aspect ratios $W/H=1.5$) was employed.

By changing the frequency of a pulsatile flow-generating pump (CompuFlow 1000 MR, Shelley Medical Imaging Technologies, London, ON, Canada) (Figure 5-4), time-varying flow reflecting a change in the Womersley number was simulated. Two flow waveforms were prescribed as inputs to the pump. The first profile was based on the nominal pressure gradient of the computational model ($f = 1\text{Hz}$) and corresponded to $\alpha \approx 2$. The frequency (ω) was then adjusted to the maximum allowable pump speed of 12 Hz yielding the second profile, representing a higher vessel Womersley number ($\alpha \approx 6$). Note that the values $\alpha \approx 2$ and $\alpha \approx 6$ simulate an unsteady and approximately

steady fluid mechanic regime, respectively, which allowed us systematically quantify the effects of pulsatility on arterial drug patterns.

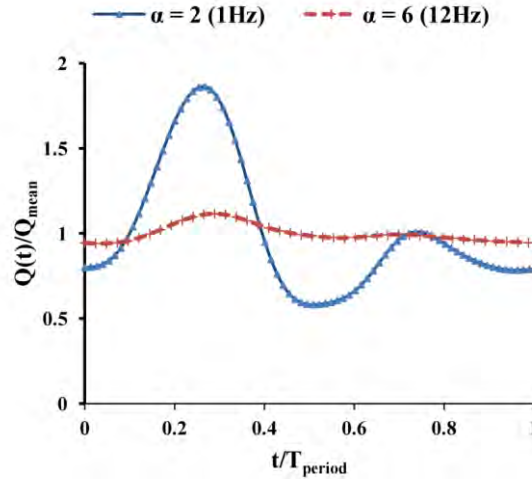


Figure 5-4: Flow profiles used in *in-vitro* validation, demonstrating a change in frequency in eqn. (5-2). These profiles are prescribed as inputs into the pulsatile flow generating pump, with cycle frequency set to 1 Hz ($T_{\text{period}} = 1 \text{ s}$) for $\alpha \approx 2$ and to 12Hz ($T_{\text{period}} = 1/12 \text{ s}$) for $\alpha \approx 6$.

After an experimental run-time of 180 minutes, the hydrogel was removed from the channel and bisected and cross-sectional images obtained. Experiments were performed in triplicate ($n = 3$) and shown in units of concentration mg/m^2 . Results are presented with mean \pm standard deviation.

5.4. RESULTS AND DISCUSSION

Unsteady flow modulates the behaviour and magnitude of the viscous boundary layer inside an arterial vessel. Endovascular stent struts are positioned so that they reside within the vicinity of this region and impose local alterations to the flow field. Given

the large differences in fluid regimes between vascular beds, it becomes natural to ask as to how the unsteady forces affect arterial drug distribution patterns. It is known that transport of drug into the tissue is driven by the concentration gradient on the mural surface, and the drug-rich recirculating regions juxtaposed to the struts, act to extend the contact area of the drug and enhance concentration in the tissue below [89, 90, 93]. As the length and intensity of these recirculating regions is coupled to the instantaneous flow field surrounding the stent strut, we explored the effect of dynamically changing pulsatile flow patterns (as governed by frequency) on stent-based drug delivery. This was done by first describing the instantaneous flow field surrounding the stent generated by a change in the unsteady flow environment. These instantaneous changes are then related to overall drug distribution from a model stent strut, followed by experimentally validating these observations.

5.4.1. PULSATILITY MODULATES LOCAL FLOW MILIEU AROUND STENT STRUTS

Pulsatile flow over a stent strut introduces dynamically changing recirculation lengths proximal and distal to the stent strut (Figure 5-5a), the lengths of which track the extent and direction of the instantaneous flow past the stent strut. The direction of the flow is fundamental to the fluid mechanics surrounding the stent strut. In particular while flow is positive, the proximal flow disruption will remain at least 2-fold smaller than the distal region, however when flow reverses these regions are now reverse in aspect.

This will be critical when we consider that a change in the frequency of the pressure gradient can either introduce significant periods of reverse flow when frequency is decreased (Figure 5-3b), or create an almost static positive flow environment when

frequency is increased sufficiently (Figure 5-3c). Correspondingly, about the stent strut at $\alpha=1$ (Figure 5-5c), we see large changes in the sizes of the proximal and distal recirculation regions over the cycle. In particular, while local flow magnitude is positive, the distal recirculation region will remain at least two times larger than the proximal. However when flow reverses, the proximal region increases dramatically in size. This is in contrast to $\alpha=16$, shown in Figure 5-5d, where equivalent steady, standing recirculation regions are observed. This increase in the area of the proximal flow disruption on account of reverse flow, meant that a change in α from 16 to 1 yielded a cycle-averaged proximal region length that increased in size by 74% (Figure 5-5b). Cycle-averaged lengths in the distal region did not show the same sensitivity, since net flow remains positive (Figure 5-5b).

While it is a non-intuitive finding that unsteady periodic flow characteristics can induce both temporal changes as well as changes to the time-averaged flow field surrounding a stent strut, it will be critical to our understanding of the effects of pulsatility on local drug delivery.

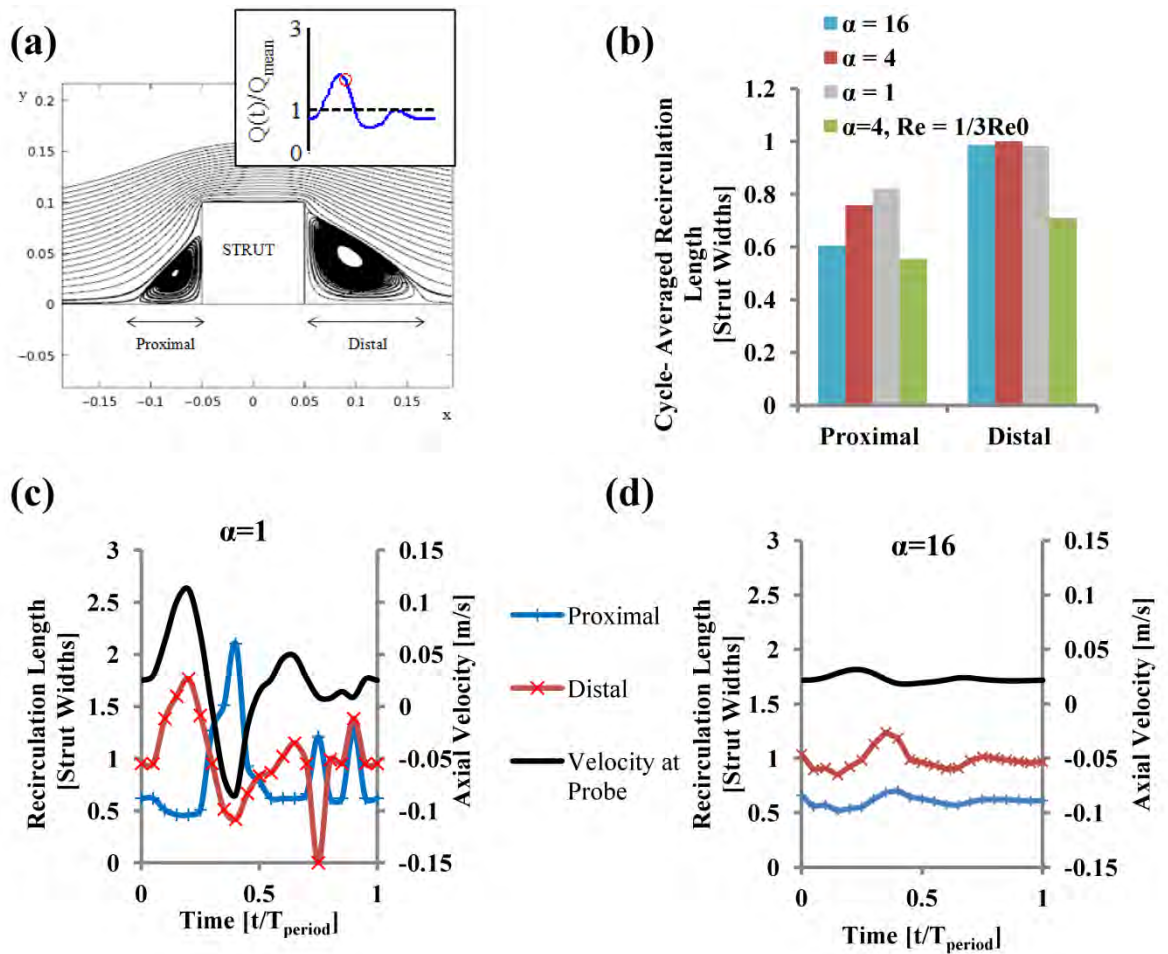


Figure 5-5: Instantaneous flow field surrounding a stent strut. a) Flow path lines for the nominal case of $\alpha=4$ at an instantaneous time point during systole ($t=0.3T_p$) show the respective lengths of the strut-induced recirculation flow regions in the proximal and distal. b) Cycle-averaged proximal and distal recirculation lengths for each of the cases of a Womersley number change. c) Instantaneous lengths of recirculating flow in the proximal and distal segments were plotted for a decrease in frequency of the pressure gradient, and d) an increase in frequency to $\alpha = 16$. Shown on the right axis is the local velocity in the boundary layer measured at a probe one-strut width into the flow ($y=0.1\text{mm}$) far upstream of stent strut.

5.4.2. *IMPACT ON STENT-BASED DRUG DELIVERY*

Dynamically changing recirculating regions throughout the cycle, lead to alterations in the amount of pooled drug in contact with the mural surface. Considering first the spatial concentration for the nominal case $\alpha \approx 4$, large concentrations are evident immediately below the stent strut with variations in the areas proximal and distal to the strut (Figure 5-6a). While the spread of drug is wider in the distal aspect, drug concentration appears higher in magnitude in the proximal portion of the tissue. This is because the mass released from both aspects of the stent strut is equivalent at each time point, and so a proximal recirculation region which at this time point has a length that is $\sim 2X$ times smaller than the distal length, will correspondingly allow drug to increase to a much higher concentration at the mural surface. The direction of the flow also means that drug is carried from the surface into a concentration boundary layer downstream of the strut. The overall effect for a net downstream luminal flow is a distribution of drug skewed towards the distal segment, following the trend determined in literature [89, 90, 93] and those results found in Chapter 4.

A change in the steady Reynolds number of the flow results in a larger deposition in both proximal and distal aspects of the tissue and lumen. Following a scaling of the flow rates by $1/3$, instantaneous recirculation lengths are decreased yielding a larger pooling concentration of drug and less washout of the drug into the bulk flow (Figure 5-6b). Correspondingly in the tissue, a similar pattern of drug is observed but in a higher concentration in both aspects for the smaller Reynolds number (Figure 5-6c). The net result of a decrease in Re , is an increase in total drug uptake, measured as the Area-Weighted Average Concentration (AWAC) in the tissue (Figure 5-6d).

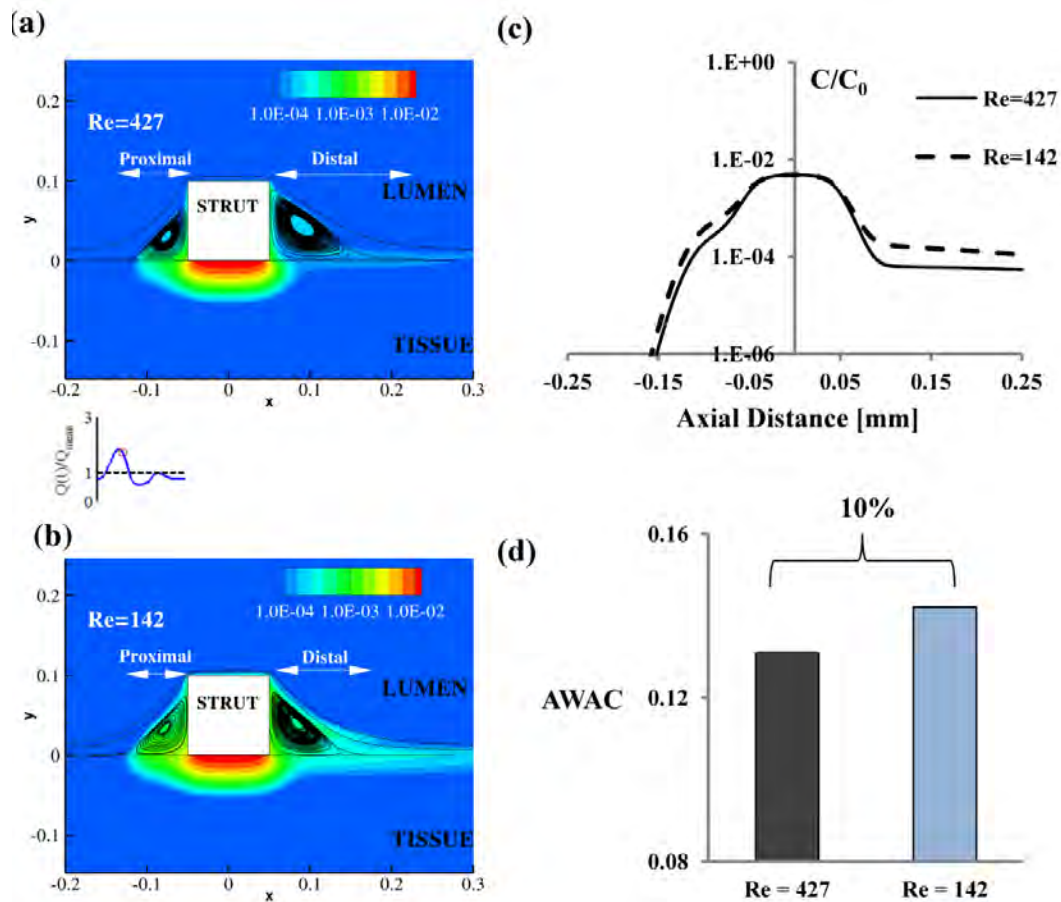


Figure 5-6: Arterial drug deposition for a change in the steady flow parameter. a) Drug distribution and flow path lines (in black) indicating recirculating flow proximal and distal to the stent strut where drug accumulates for the nominal case of $\alpha=4$, shown at a time period of $t=50s$, with inset showing the instantaneous time point in the cycle. b) When the instantaneous flow rate was scaled by a factor of $1/3$ yielding an equivalent decrease in the mean Reynolds number (Re). Recirculation lengths decrease in size with decreasing flow rate, with the decrease most obvious in the distal region. Drug concentration contours also show a larger amount of drug for the lower flow rate. c) When Re is decreased the spatial drug distribution in the tissue, measured at a distance $y=-0.2mm$ (or $1/5W_t$) below the mural surface, shows a similar pattern but different magnitudes in proximal and distal regions of the strut. Results are shown in units of normalized concentration. The strut lies between $-0.05mm < x < 0.05mm$. d) Area-weighted average concentration of the accumulated drug in the tissue increased by 10% at 50s when Re of the nominal case decreased by $1/3$. α is kept constant for a Re change.

In contrast, sensitivity to flow pulsatility was found to be relatively insignificant. When α was varied by changing the frequency of the cardiac pulse, there was only a small difference in the net drug deposition at $T = 50$ s (Figure 5-7a). Spatial variation of the drug in the tissue (Figure 5-7b) shows peak concentration to be similar while small variations appear in the proximal and distal portion of the tissue. As α is decreased from 16 to 1, the local concentration falls in the proximal region but the length by which it is spread increases by 3-fold. This phenomenon can be understood by considering the instantaneous flow field for different α (Figure 5-5); the introduction of reverse flow at low α will increase the proximal region's length, this will act to dilute the instantaneous magnitude of the mural surface concentration and concomitantly, extending the length of the mural interface exposed to drug.

The distribution in the distal aspect of the tissue shows a similar pattern however in larger quantities for the steady equivalent case of $\alpha = 16$ (Figure 5-7b). This trend implies that **drug uptake in a dynamically changing flow field will be inferior in magnitude to that with approximately steady standing recirculation zones.** Systematic dilution via instantaneous changes in the distal recirculation length, when coupled with the exponentially decreasing rate of drug release from the stent coating, will mean that cycle-averaged surface concentrations, and thus tissue uptake are time-dependent. In this case, larger oscillations over a longer time period ($\alpha = 1, T_{period} \approx 17.1$ s) will act to decrease the efficiency of this distal zone in its contribution to total drug uptake (Figure 5-7b) when compared to a flow with only small instantaneous changes in their length ($\alpha = 16, T_{period} \approx 0.068$ s).

Despite these small differences in distal zone efficiencies, when the combined proximal and distal recirculation lengths (total cycle-averaged lengths) are plotted against AWAC in the tissue (Figure 5-7c), we see that an inverse and approximately linear relationship exists between the cycle-averaged recirculation region and net drug deposition.

That transient variations are explained well by the cycle-averaged size of the recirculation region implies a relative **insensitivity to the prevailing instantaneous changes** in the flow field. This lack of a significant temporal response under pulsatile flow was observed by others as well who studied the effects of species transport with low diffusivities (high Schmidt number, $Sc > 10^3$) in both straight vessels [95] and those with secondary flows [96]. Both studies reported only weak effects due to the pulsating flow. Importantly though, these differences in total drug uptake for a change in α are small in magnitude when compared to those due to a change in Reynolds number. This indicates a strong correlation between arterial drug distribution patterns and steady flow characteristics but only a weak correlation due to unsteady fluid forces.

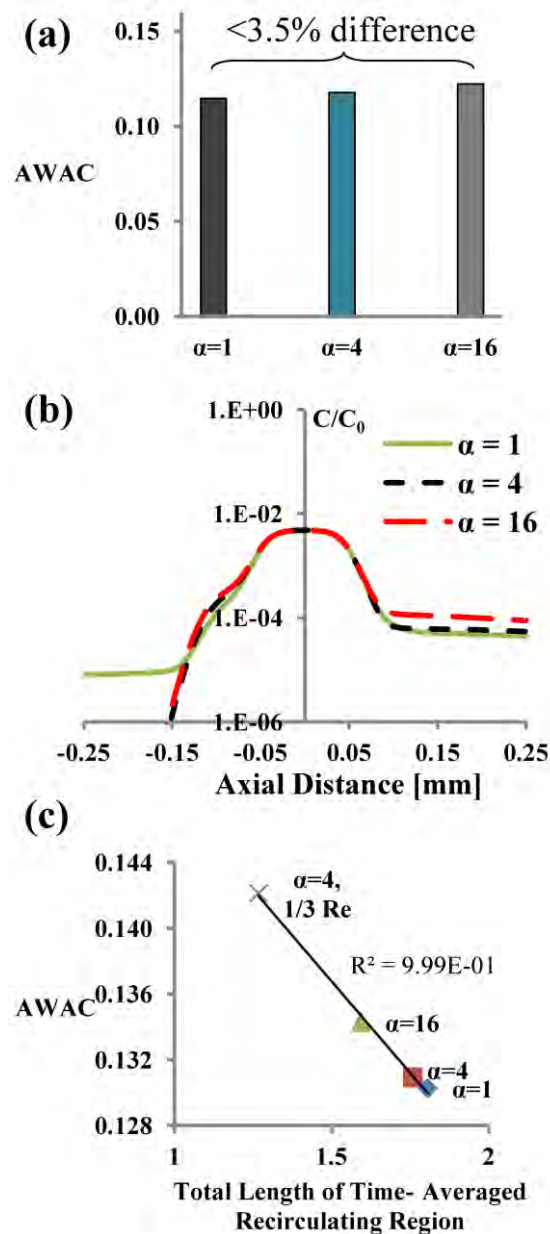


Figure 5-7: Arterial Drug deposition for a change in the unsteady flow parameter. a) Area weighted average concentration (AWAC) in the tissue at a time $T=50$ s for varying Womersley number as a result of a frequency change in the driving pressure gradient (shown in units of concentration normalized to initial concentration C_0). b) Womersley number changes the spatial drug distribution in the tissue, measured at a distance $y=-0.2$ mm (or $1/5W_t$) below the mural surface, with stent strut residing between -0.05 mm $<x<0.05$ mm. c) AWAC versus total length (proximal + distal) of the cycle-averaged recirculating region for each Womersley number, showing linear relationship with negative slope. The high R^2 value indicates a strong linear relationship between total drug uptake and steady flow equivalent recirculation lengths.

5.4.3. IN-VITRO VALIDATION

A representative analogue of a single stent strut residing in a standardized vascular bed, the *in-vitro* design provided a platform by which to appreciate the modulating effects of dynamic flow parameters on local drug delivery. After exposure to a controlled flow waveform simulating a frequency-dependent change in the Womersley number, the synthetic arterial tissue bed was sectioned to yield a spatial map of the marker drug in the cross-sectional plane. When α was increased from 2 to 6, little change in the drug distribution was observed.

The spatial distribution of drug was similar for both cases (Figure 5-8a), while the change in total drug uptake shows little sensitivity to a change in the unsteady flow field (Figure 5-8b). Furthermore, this difference was also small compared to that from a change in the Reynolds number (Figure 5-8b). A decrease in the inlet flow rate ($Q(t)$) by a factor of 2 ($1/2Re = 213$) yielded an increase in the total marker-drug uptake by approximately 28%. While this difference did not reach statistical significance, it does indicate a relationship already determined from the computational model (Figure 5-6d). Taken together, these results for a single stent strut underscore the dependence on net flow rate but offer no significant evidence of a relationship with the unsteady flow field. These sensitivities imply a vascular bed dependency that is defined by those factors associated with a change in net luminal flow and not pulsatility.

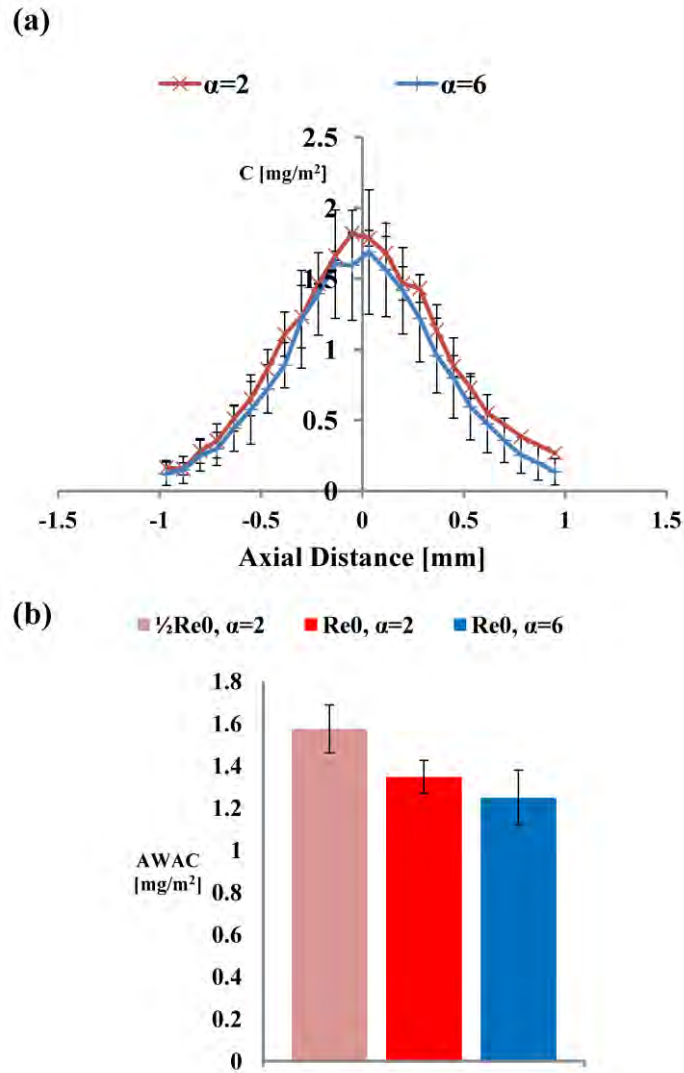


Figure 5-8: *In-vitro* validation of sensitivity to unsteady flow. Arterial drug distribution remains invariant due to changes in the unsteady flow field. a) Spatial concentration profiles measured at a distance $z=-0.5\text{mm}$ into the thickness of the hydrogel, for the two waveforms demonstrating a change in the unsteady flow. Fluorescein-Sodium concentration was found to be consistently higher at an axial location downstream ($x=+0.68\text{mm}$ or 2.0 strut widths) compared to the same point upstream ($x=-0.68\text{mm}$) ($29.9 \pm 6.82\%$ for $\alpha=2$, and $28.3 \pm 5.08\%$ for $\alpha=6$). b) AWAC measured as the mean concentration over the x - z plane (similar to that in Figure 4-5), for a change in Womersley number and the mean Reynolds number. AWAC was shown to decrease by 7.3% ($\pm 17.3\%$) when α was decreased. This difference is small compared to a change in the mean Reynolds number. Where AWAC was shown to increase by 28.8% ($\pm 18.0\%$) when Reynolds number was decreased by a factor of $\frac{1}{2}$.

5.4.4. IMPACT OF SUBOPTIMAL DEPLOYMENT

So far it has been demonstrated how factors characterizing flow pulsatility play a relatively insignificant role in governing arterial drug distribution for fully-apposed strut configurations. However, not all stents undergo ideal deployment and moreover, arterial wall negative remodelling may occur in some cases; both leading to stent struts being positioned away from the vessel wall. To fully appreciate the role of flow pulsatility in stent-based drug delivery, it is useful to consider sub-optimal interventional settings (such as strut malapposition) in the context of a change in the unsteady flow field. Simulations performed on varying degrees of strut malapposition for a given Womersley number ($\alpha = 4$) showed that malapposed struts create unique local flow disruptions that in turn act to modulate the amount and pattern of drug absorbed within the tissue (Figure 5-9a-c). For instance, a strut displaced by a distance $h = R/300$ (equivalent to 1/10 of strut width) sees drug deposition in the tissue decrease by almost 93% (Figure 5-10) yet still has drug levels in appreciable concentrations in the immediate vicinity of the strut (Figure 5-9a). As the strut is moved further away from the wall, these flow disruptions with pooled drug, move further into the free stream and away from contact with the mural interface (Figure 5-9b). Accordingly, we see drug uptake into the tissue decreasing exponentially with h (Figure 5-10). At wall displacement of $R/30$, strut-adjacent flow-disruptions were contained wholly in the free stream resulting in negligible mural surface concentrations and thus insignificant drug uptake into the tissue below (Figure 5-9c).

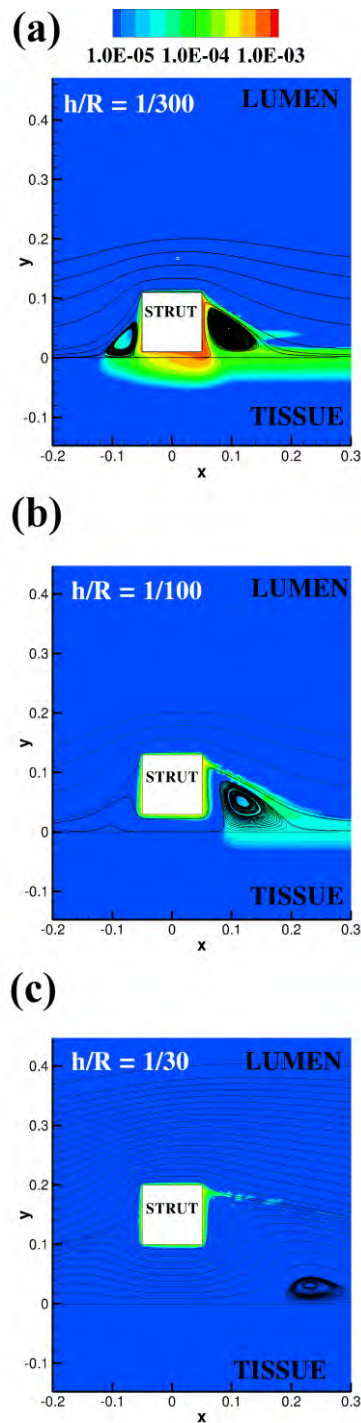


Figure 5-9: Arterial drug distribution for suboptimal interventional settings. (a-c) A single stent strut for $\alpha=4$ with various wall displacements is shown to create individually unique instantaneous flow fields, and thus varying degrees of flow stasis where drug is shown to pool. Drug contours and flow streamlines are shown at a time point of $t=50s$, and malapposition is measured as wall displacement, h , normalized to the radius of the vessel, R .

Simulations also demonstrated that arterial drug levels of a malapposed strut were sensitive to changes in the unsteady flow parameter. When α changed from 4 to 1, via a change in frequency, arterial drug uptake from a strut malapposed by a distance of $R/300$, increased by 10% (Figure 5-10). Sensitivity to α increased further with distance between vessel wall and drug source, until finally the strut-adjacent flow disruptions lost contact with the vessel wall. Since drug uptake for a malapposed strut is only via drug pooling within the flow recirculation zones, sensitivity to the unsteady flow parameter implies that the pulsatile nature of blood flow does in fact play a role in modulating arterial drug uptake, but only as a function of device deployment settings. Moreover it is the stent-wall interaction that will define the extent to which pulsatile flow patterns affect arterial drug deposition. Only under ideal device deployment settings can those effects of pulsatile flow on arterial drug distribution be neglected; highlighting the importance of stent deployment settings in our understanding of the dynamically changing luminal flow environment and its impact on stent-based drug delivery.

The results showed that even subtle changes in stent wall malapposition had profound effects on uptake. Our bench-top models was inadequate in resolving these changes in wall position (of the order of 10 microns), and it is only through computational modelling that these small changes in deployment can be appreciated. Indeed computational models have proved as useful tools in understanding the mechanisms governing drug delivery from stents [82, 137].

The method used in this study utilized an integrated approach. Given the strong qualitative evidence in the results of Chapter 5 indicating a correlation between our benchtop and numerical results, it is therefore natural to question why a full quantitative comparison was not pursued. While quantitative comparisons between the *in-vitro* method and an equivalent computational model are attractive and would, indeed, yield a thorough validation of our numerical method, several limitations prevented a full quantitative comparison. Firstly a steady-state distribution would take months to realize, and involves many more events beyond the scope of a bench-top model, including drug interaction with tissue elements, as discussed in Section 1.4.2.

At the same time, we were prevented in our transient computational model to simulate over any realistic period of time. In particular, we saw that the time-scale of realistic unsteady blood flow (of the order of 1/10 second) required the numerical simulation to be truncated at a solution time of 50 seconds- so as harness available computational power- a time far premature of the *in-vitro* endpoint (3 hours). As more computational power becomes available, a thorough validation may be possible and should be investigated.

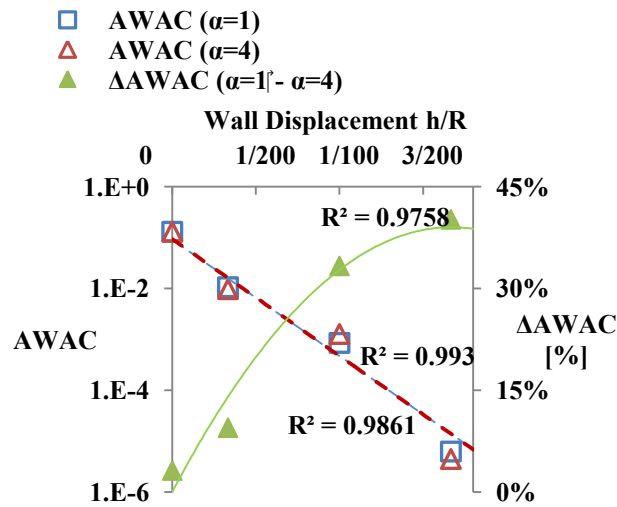


Figure 5-10: Malapposition and the unsteady flow parameter. Drug deposition, measured as AWAC, decreases exponentially with increasing wall displacement. AWAC increased by 10% when a strut displaced by a distance $h/R=1/300$ had a change in α from 4 to 1, and decreasing by 33% for the same α change when the strut was displaced by $h/R=1/100$.

As with any computational model assumptions were necessary to accommodate available computational resources and to facilitate analyses. For instance, theoretical aspects of pulsatile fluid mechanics have been utilized along with an idealized fluid and geometry to determine physiologically realistic boundary conditions, whereas actual circulatory flow is a complex milieu of platelets, plasma and cells, in vessels with highly irregular geometry. Furthermore, biological aspects of a change in vascular bed have been neglected; tissue wall architecture and lesion morphology will all vary with a change in anatomical location. Future work is aimed to add insight into these aspects by considering models incorporating pathophysiologic settings.

5.5. CONCLUSION

Pulsatile luminal flow leads to instantaneous changes in the flow field that are in turn dependent on both arterial bed geometry and flow frequency. When struts releasing drugs are placed within different arterial beds, drug uptake is sensitive to parameters governing flow pulsatility as a function of stent position relative to the arterial wall. A change in Womersley number via a frequency change contributed minimally to total drug deposition for a well-apposed strut, while a similar change for a strut offset from the vessel wall lead to significant changes in arterial drug uptake. These findings suggest that one could approximate the effects of pulsatile flow on arterial drug distribution using its steady flow equivalent, only under ideal device deployment settings. In turn this paves way for better appreciation of stent-based drug delivery under dynamically changing physiologic and procedural settings and it's utilization to other beds beyond the coronary vasculature.

CHAPTER 6. ARTERIAL DRUG DEPOSITION AT THE AORTA-RENAL OSTIA

In this chapter we investigate how vascular geometry induced changes to the flow field can effect local drug distribution, with a focus on stent positioning at the Aorta-Renal Ostia. Results will aim to determine how stent position relative to the ostia acts to influence the local extent and uptake of spatially distributed drug. The chapter begins with a short review of the literature presented in Chapter 1.

6.1. INTRODUCTION

A change in vascular bed can introduce large changes in the core flow due to complex geometry changes, for instance with bifurcation and tapering of the vessels. How stent placement modulates arterial drug uptake in the instance of these large geometry induced changes in local hemodynamics is unknown.

In the present Chapter we expand our understanding of flow mediated transport and its sensitivity to flow direction and magnitude (Chapter 4), and unsteady flow factors (Chapter 5) to consider the effects of large scale flow misalignments (axially asymmetric), characteristic of flow at the Aorta-Renal Ostia (ARO). While the effect of flow mediated drug transport has been extended to small angled bifurcations [93], the flow field within the Aorta-Renal branch is unique. The 90 degree bend, coupled with low resistance at the kidneys, leads to significant axial flow skew with large near wall velocities on the caudal side and regions of separation, recirculation and stagnation on the cranial side. The effect of this flow discontinuity on drug transport, together with the

smaller scale flow perturbations caused from the strut obstruction to the boundary layer, is yet to be appreciated with respect to placement of DES in the renal artery.

Moreover stent deployment in the renal artery is unique to this vascular bed. Clinical evidence shows that 80% of Atherosclerotic Renal Artery Stenosis (ARAS) occur proximal to the ostium [105], and are most often stenosis caused by aorta plaque encroaching on the renal branch. Suggested treatment in the instance of angioplasty failure includes placement of an endovascular stent so that it protrudes 1 - 2mm into the aorta lumen [106] so as to prevent elastic recoil of the vessel [107-109]. Recent developments have also seen the introduction of trumpet-shaped, side branch specific stents which aim to conform and round the ostial walls [18]; both methods of implantation are likely to significantly change the flow field in the renal branch.

Understanding efficacy of the DES in the ARO is of great clinical concern: 7% of American's over the age of 65 suffer from ARAS [143], with rates significantly higher in patients with peripheral [144] or coronary artery disease [145, 146]. High rates of restenosis following balloon angioplasty [108] have meant that stent revascularization is now the preferred method of treatment for ARAS [109, 147], however there is little evidence of its safety and efficacy in reducing restenosis rates [45, 52, 88]. Despite uncertain clinical outcomes, the use of DES is being considered for treatment of renal artery disease [45]. Certainly evidence supports the on-label use of DES in coronary interventions [68, 148] but are current revascularizations strategies for on-label use of DES sufficient for applications in the treatment for ARAS?

In this study a coupled two-dimensional computational fluid and mass transport model was used to analyse spatial drug distribution at sites downstream of the ostium. It is postulated that stent placement in the vicinity of the ARO will lead to asymmetries in the locally distributed drug, the extent of which will be modulated by geometry. Appreciating these variations in arterial drug patterns on account of non-linear flow, may help ensure appropriate device selection and design.

6.2. METHODS

6.2.1. FLUID AND MASS TRANSPORT MODEL

The computational domain, shown in Figure 6-1, models stent struts as blocks with unit aspect ratio, drug-laden surfaces of unit dimensions, 0.1mm X 0.1mm, fully-apposed to tissue wall on the abluminal side [81, 89, 93, 128]. Model aorta and renal branch radii, R_a and R_r respectively, were based on values taken from previous experiments [112]. The renal branch was assumed to be of length $6R_a$, such that the outlet is far enough downstream of any disturbances to the flow (for instance that caused by the stent placement or arterial branching in the computational model). It was assumed that implantation of a stent introduces sufficient rigidity to assume rigid wall. Furthermore it was assumed that positioning the proximal portion of the stent at the ostium created a sharp transition at the corner of the tissue-lumen interface. The model geometry for a curved inner wall was created using higher order splines with a prescribed radius of curvature, R .

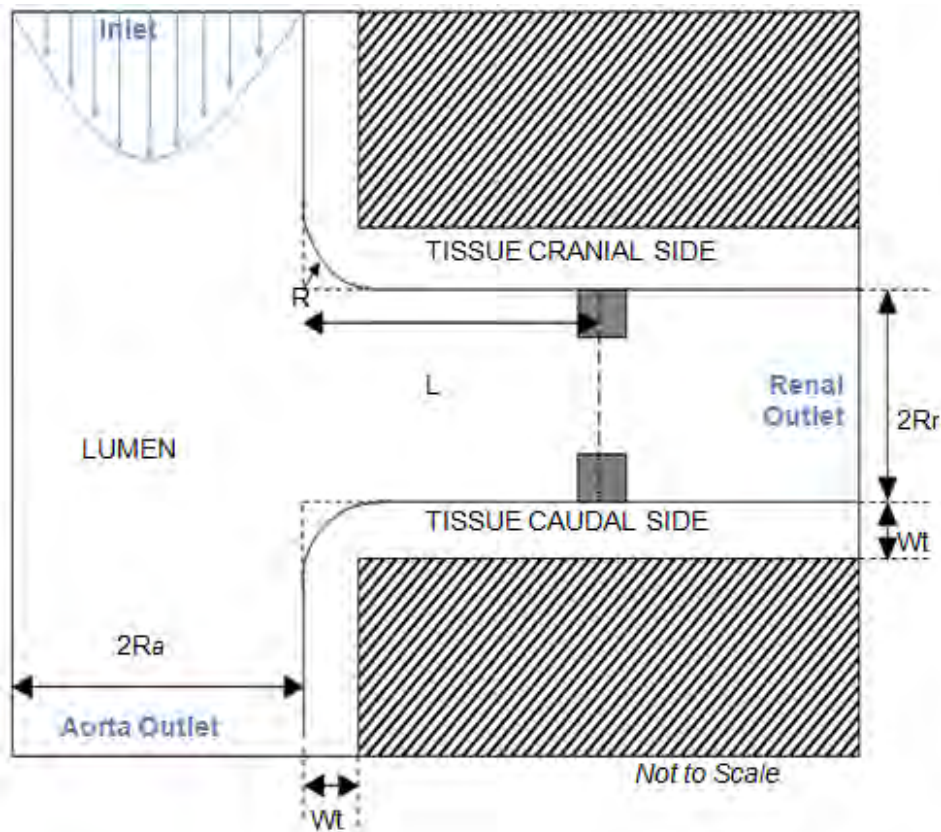


Figure 6-1: Computational domain for the DES at the aorta-renal ostium. A stent strut is placed on either side of the vessel at the lumen-tissue interface, where L downstream of ostium is the distance from ostium to stent strut. R_a and R_r are the radii of the Aorta and renal branches, respectively, and W_t is arterial wall thickness of the tissue cranial and caudal sides. Curvature with radius R is introduced to smooth the corners of the bifurcation.

Blood was assumed to be a fluid with density $1.06g/cm^3$ and a shear-dependent dynamic viscosity (eqn. (2-1)) to systematically account for its non-Newtonian characteristics, especially significant in boundary layer flow [90, 93]. Luminal blood flow was governed by the continuity and Navier Stokes equations (eqn. (2-2) and eqn. (2-3)). Transport of interstitial fluid through the porous medium was modelled using

the continuity and Darcy's equations for tissue fluid transport (eqn. (2-4) and eqn. (2-5)), with volume porosity available to interstitial flow set at 0.61 [94, 129], and drug permeability was set to $K = 1.43 \times 10^{-14} \text{cm}^2$ [129]. Drug concentration was specified as a normalized concentration (i.e. $c_i = \frac{c_i}{c_{strut}}$), and modeled using a general equation for passive scalar transport of a solute (eqn. (2-6)). The model drug used in this simulation assumes fluid and tissue drug diffusivity as $D_f = 3.89 \times 10^{-7} \text{cm}^2/\text{s}$ [115] and $D_t = 3.68 \times 10^{-8} \text{cm}^2/\text{s}$ [83], respectively.

Simulations were run under steady state conditions (time derivatives of the governing equations were neglected). A constant (steady) flow inlet condition was considered valid here, given that unsteady flow effects were shown in Chapter 5 to be relatively insignificant in determining drug deposition when the stent strut was fully-apposed to the wall, as is the case in this study.

Boundary conditions for the aorta and renal outlets were based on expected mass flow splits of 24% proximal aortic flow in the renal artery branch in three-dimensions [112], corresponding to an average velocity of 0.236 m/s ($Re_{mean} = 250$) through the renal branch outlet. Mean inlet velocity was set at 0.0835 m/s ($Re_{mean} = 584$). Blood flow in large arteries is not Poiseuille parabolic but instead has an inviscid core flow that tends to be blunt in shape. The cycle-averaged velocity profile of characteristic pulsatile flow in the supra-renal aorta, taken from our earlier work (Figure 5-3d in Chapter 5), was prescribed at the inlet.

It was assumed that left renal flow has no fluid mechanical interactions with downstream aortic flow and therefore a zero relative pressure outlet condition was applied at the aorta outlet. The perivascular wall was modelled with an impermeable boundary condition, and continuity of flux was assumed at all domain interfaces. Drug elution from the stent strut surface was modelled with a Dirichlet boundary condition with unit concentration applied to the strut surfaces.

6.2.2. NUMERICAL SOLUTION

Computational simulations were performed with ANSYS CFX v12.1 (ANSYS Inc.), which uses a fully coupled solver to solve the transport equations as a single system, with solver settings described in Computational Methods in Section 2.5.2. In particular pressure-velocity coupling was handled with a Rhie-Chow algorithm [127] and spatial discretization of momentum and mass transport variables was performed with a bounded second order accurate upwind scheme based on that of Barth and Jespersen [126]. Steady state solutions were taken after there was a 10^{-7} reduction of the transport variable between each iteration.

6.2.3. MESH DEPENDENCE STUDIES

In order to accurately capture the concentration boundary layer, a highly resolved mesh was required in the regions close to the walls and surrounding the stent struts. Furthermore, the relative size of the stent struts with respect to the computational geometry also contributed to overall mesh size. A mesh independent solution, defined as less than a 5% change in total drug deposition for successive refinements, was obtained with a structured mesh element thickness 1.3% of strut width at the boundary,

and 5% of strut width in the remaining domain (See Appendix 6 and Figure 7-5). Further refinement changed the solution by less than 5% so that the final volume mesh was approximately 650,000 hexahedral elements for each case of individual stent struts, and 3.8 to 5.4 million elements for the multistrut analysis.

6.3. RESULTS

6.3.1. FLOW IN A LEFT RENAL ARTERY BRANCH

Simulations of the flow in a bifurcated sharp-edged (“No Radius”) renal branch, in the absence of stent struts, show the fundamental patterns of characteristic flow around a 90 degree bend [110, 111, 149, 150], with large areas of separated recirculating flow on the cranial side (Figure 6-2), distal to the ostium, and high speed flow on the caudal wall. Flow becomes separated (“S”) at the cranial side of the ostium and as the flow streamlines move into the renal branch, skewing the velocity profile towards the caudal side, an adverse pressure gradient causes a recirculating separation region to form on the cranial side. Flow reattachment (“R”) is seen to occur at approximately 3 diameters downstream (“3D”), then finally the velocity profile axially realigns itself at four diameters (at “4D”).

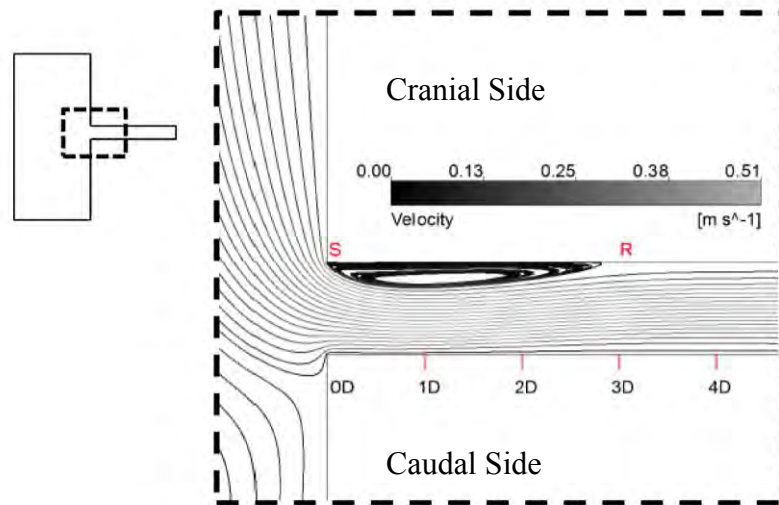


Figure 6-2. Velocity pathlines of flow through a 90 degree branch with separation point labelled S and reattachment point at R.

In order to assess the geometrical sensitivity of the model, the sharp edge on the junction corners was rounded into two shapes, and expressed in terms of renal branch radius, $R/R_R=0.5$, $R/R_R=1$. Consistent with literature [111], the radius of curvature on the inner wall decreased the size and strength of the separation region. For a radius of curvature $R/R_R=0.5$ (or half the renal radius) (Figure 6-3a), a small recirculating separation region on the inner wall persists (between “S” and “R”), smaller in size than the case of no radius however larger than that for $R/R_R=1$ (Figure 6-3b). Furthermore by increasing the inner wall radius to $R/R_R=1$, boundary layer separation was significantly smaller and the reverse flow, evident in Figure 6-2 and Figure 6-3a, was no longer apparent.

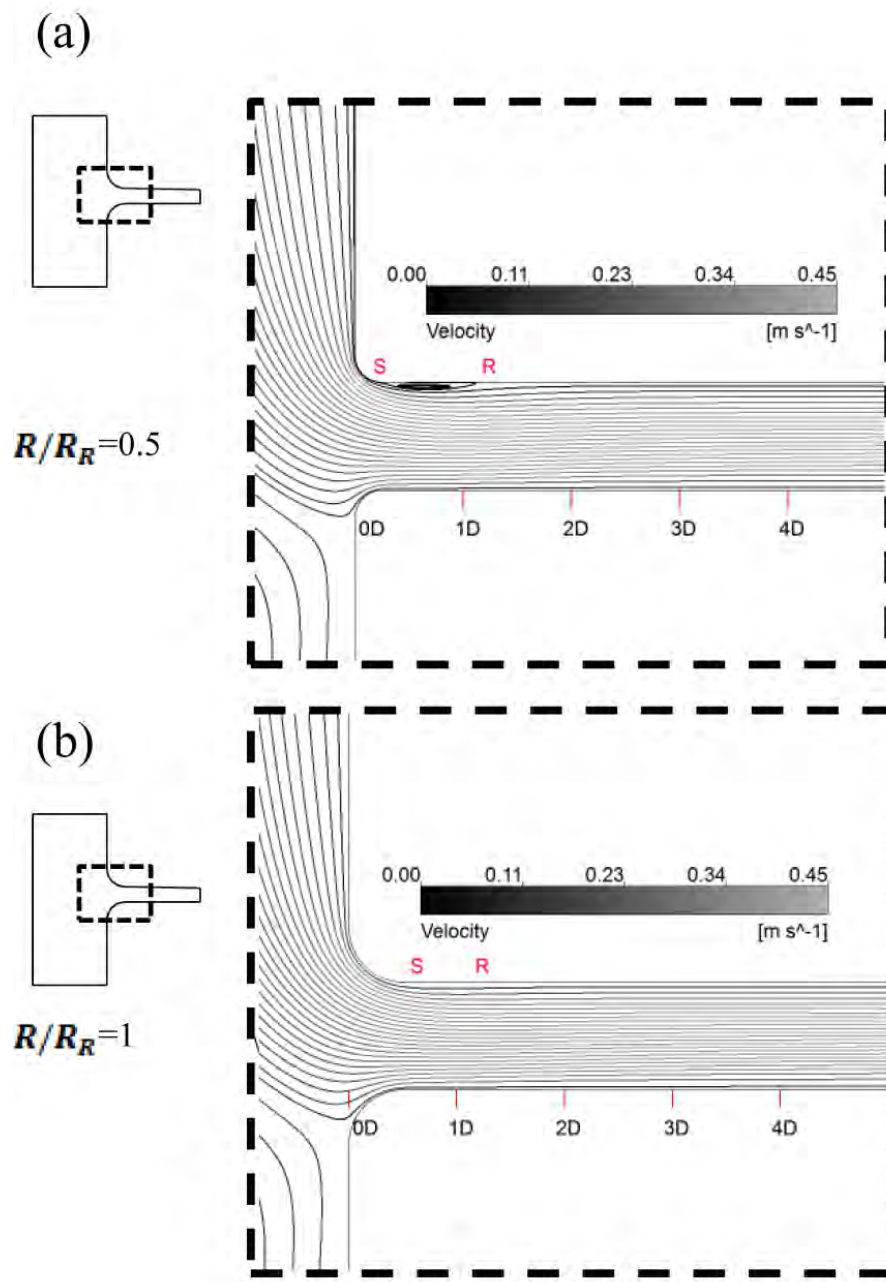


Figure 6-3: Velocity pathlines of flow through a 90 degree branch with curvature. a) $R/R_R=0.5$ and b) $R/R_R=1$. Separation point is labelled S and reattachment point is at R.

6.3.2. *ARTERIAL DRUG DEPOSITION IN THE RENAL BRANCH*

Flow discontinuity leads to a locally variable spatial drug distribution for single a stent strut. For a model of drug elution, there are two significant events taking place in the renal branch affecting drug transport. Locating the drug laden strut within the boundary layer will create local flow alterations [38] and consequently improve drug deposition through flow mediated transport [90].

Absorption of drug into the tissue is driven by the concentration gradient on the mural surface. We have previously shown (Chapter 1, Chapter 4 and Chapter 5) that the presence of drug-rich recirculating regions either side of the strut, acts to extend the contact area of the drug, drug uptake in the tissue is enhanced. However unique to a renal bifurcation is a large separation region on the cranial wall and distorted high speed flow on the caudal side. In the presence of this flow separation, the resulting concentration field surrounding the stent strut is more complex than that located in a straight arterial segment. The examples shown in Figure 6-4a & b illustrate the drug concentration fields for stent struts located on the caudal and cranial sides at 1D and 4D downstream of the ostium. Conducive with a scalar transport model, the drug concentration field correlates with the direction of flow as well as with areas of fluid separation and recirculation. Since the flow field is non-uniform, drug is shown to be heterogeneously distributed circumferentially and varies considerably between axial locations.

A stent strut located on the caudal side at 1D shows larger drug accumulation in the recirculation zone distal to the strut, and correspondingly drug deposition is larger in the

distal tissue segment, compared to that proximal (Figure 6-4a). This is in contrast to a stent strut located on the cranial side at 1D, where local flow is in reverse to that in the bulk flow, and consequently shows a larger drug accumulation in the area proximal to the stent strut.

For a stent located at 4D, luminal drug concentration is spread downstream of the stent strut (Figure 6-4b) and therefore arterial drug concentration is elevated in the distal portion of the tissue. At this axial location flow is forward moving (with respect to bulk flow direction) and approximately axially symmetric (Figure 6-2a). The concentration field is therefore independent of the flow separation, resulting in a roughly symmetric drug concentration distributions on either side of the vessel.

6.3.3. *STENT POSITION DETERMINES DRUG UPTAKE*

Simulations of arterial drug deposition at the site of the ARO predicted that local efficacy of drug uptake into the vessel was dependent on its location relative to the flow discontinuity. For the case of no radius, local drug uptake was found to be consistently higher on the cranial side. Specifically we can see that stent struts located within the separation region 0D to 3D (Figure 6-2) had the highest rate of drug uptake (Figure 6-5a). Drug uptake was least on the caudal wall proximal to the ostia, where large local velocities and a large radial component directing flow away from the wall resulted in significantly impaired drug uptake.

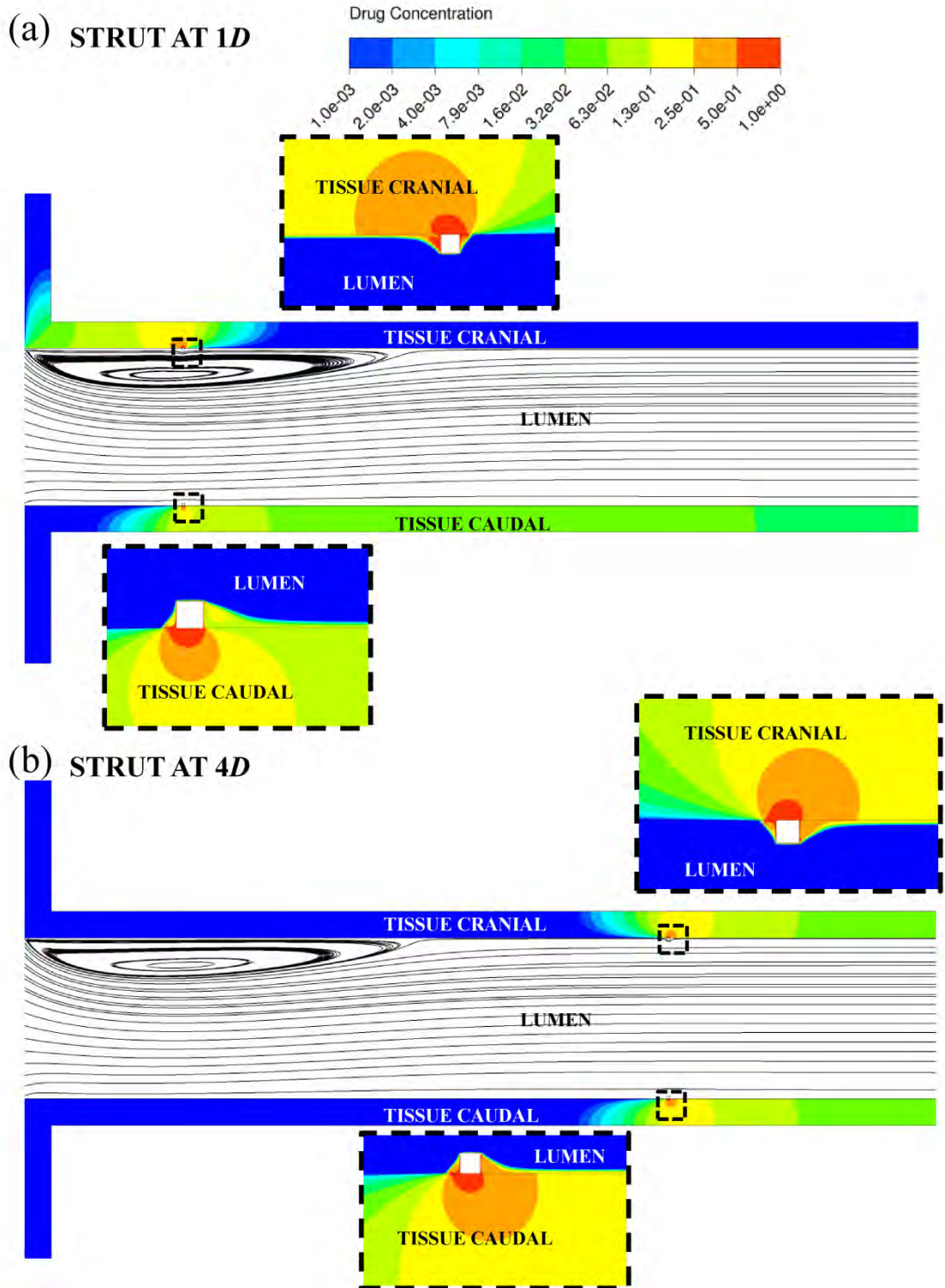


Figure 6-4: Contours of the drug concentration field surrounding a stent strut positioned at a) $L = 1D$ and b) $L = 4D$ downstream of ostia in a 90 degree branch with No Radius of Curvature ($R/R_R=0$).

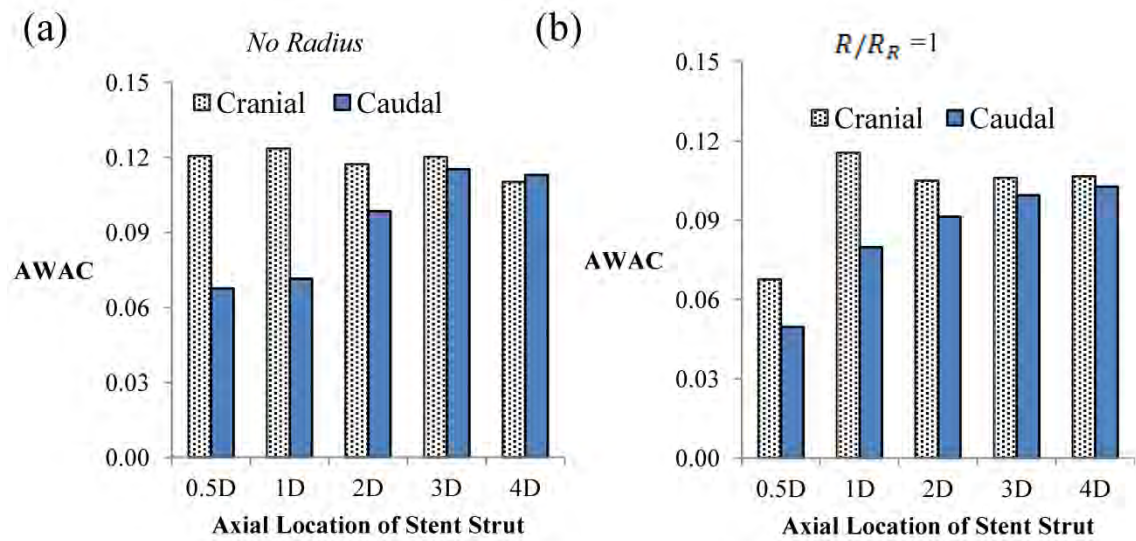


Figure 6-5: Local drug uptake from a single stent strut at axial locations downstream of ostia, measured as the ratio of AWAC in the tissue within 20 struts widths of stent location.

This asymmetry was similarly obvious for the case of curvature on the inner wall. Struts located inside the separation region (1D on the cranial side) experienced drug uptake that was 1.8-fold larger than a stent strut upstream of separation point (0.5D) on the same side (Figure 6-5b), and 1.45-fold larger than the same axial location on the caudal side.

Circumferential asymmetry (cranial / caudal) decreased in magnitude with distance away from the ostium. In the case of no radius, drug distribution was relatively symmetric again at 4D, once flow realigned itself (Figure 6-2). While asymmetry was still persistent for the case of a rounded inner wall (Figure 6-5b) it was smaller in scale, coinciding with a smaller recirculation region. Generally the maximum difference between cranial and caudal sides of the vessel was found to coincide with deviation of

core flow streamline from geometrical centreline (Figure 6-2 and Figure 6-3b), indicating that circumferential asymmetry in drug uptake scaled with asymmetry in axial flow. In other words the more skewed the axial velocity profile, the larger the difference in drug uptake between struts located longitudinally and circumferentially apart.

6.3.3.1. Multiple Struts

Individual stent struts will form part of a larger network comprising a stent. We see on the cranial side a localization of drug within the stent length (Figure 6-6a and Figure 6-7), spread relatively evenly along this length, following the results of the single stent strut distribution (Figure 6-5a). Low local flow rates, as well as circulation of solubilised drug within the recirculation region, increases total uptake on the cranial side, so cranial tissue uptake was approximately 1.4-fold higher than that on the caudal side (Figure 6-10a). On the caudal side drug is significantly smaller in concentration proximal to the ostia compared to that in the distal portion, or even downstream of the stent, resulting in a deposition that is skewed towards the distal segment (Figure 6-7).

While this circumferential asymmetry (cranial / caudal) is improved with a curvature on the inner wall (Figure 6-10a and Figure 6-6b), longitudinal asymmetry (proximal/distal) is in fact worse (Figure 6-10b); proximal drug uptake within the stented region of tissue falls by 28% (Figure 6-10b), and distal drug uptake increases by more than 14% (Figure 6-10b). There was found to be no improvement in total drug uptake as a result of including curvature (Figure 6-10a).

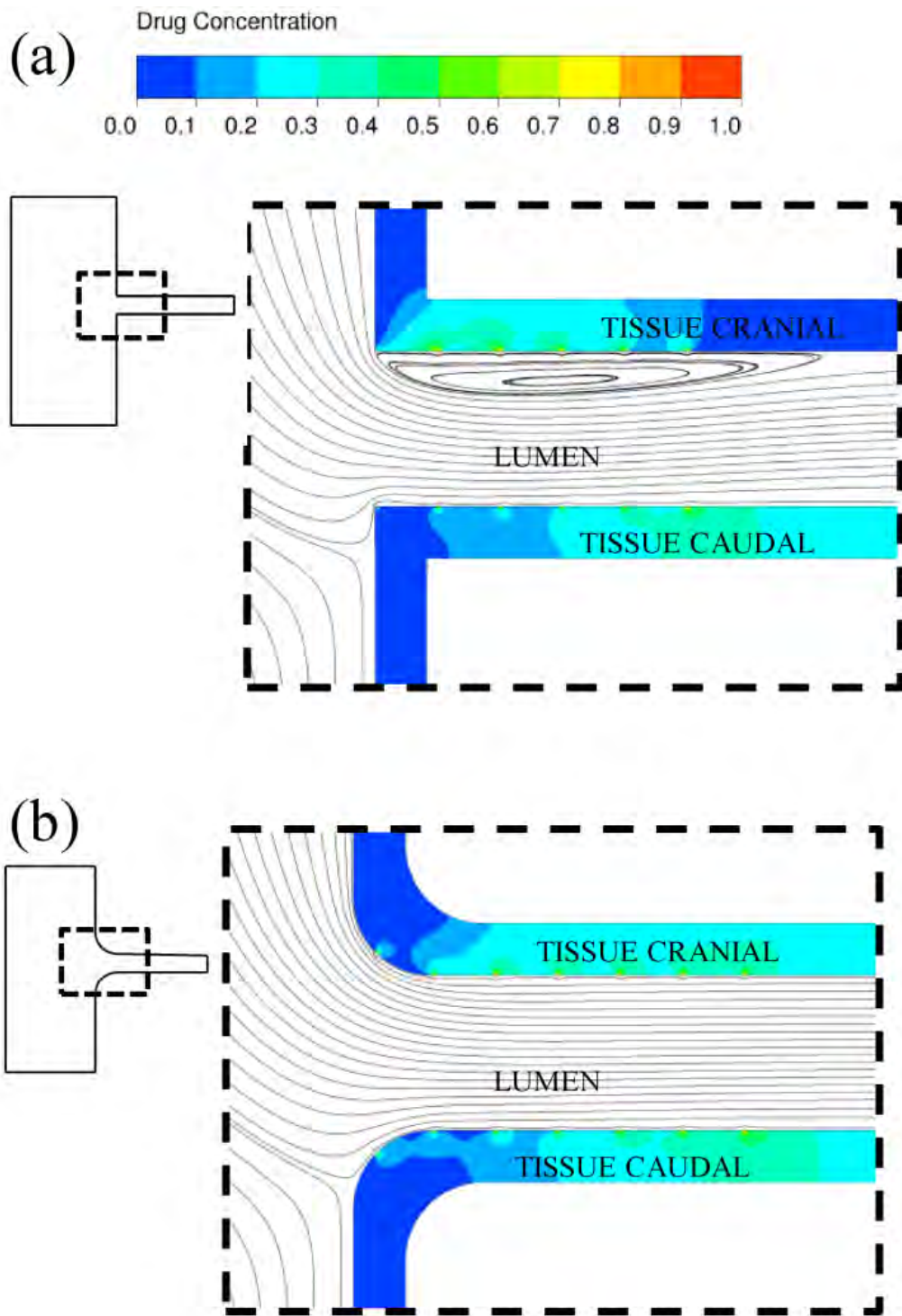


Figure 6-6: Multiple stents struts placed at the ARO. Concentration contours, shown with flow streamlines, with multiple stent struts placed at a distance 20 strut widths apart, for a) No Radius and b) $R/R_R = 1$

The placement of DES creates large drug concentration gradients within the vessel wall (Figure 6-7). Peak concentrations indicated by small local peaks (appear as bumps in the concentration profile Figure 6-7) occur immediately below the strut, and local concentration gradients between the struts are dependent on position relative to flow discontinuity. Indeed this variability in the interstrut region is induced by local asymmetries in proximal and distal recirculation regions about each stent strut, the size of which is determined by the direction and magnitude of the local flow field. Figure 6-8 shows that for struts located immediately at the site of the ostium (at 0D) flow, the deranged flow field acts to significantly impede drug delivery. This is most extensive on the caudal side, where large recirculating flow acts to prevent drug from pooling in the lumen in any significant quantities. The concentration profile in the tissue on the caudal side increases from negligible quantities at the ostium, to its peak downstream just downstream of the last stent strut (Figure 6-7). This is in contrast to the cranial side, where flow rates in this near wall region are in reverse to the bulk flow and consequently concentration decreases as we move proximal to distal. Furthermore since flow rates are consistently low in the recirculating region, the concentration gradient is not as steep as that on the caudal side, with concentration in the distal aspects (approximately 2D) only decreasing by 2 fold when compared to the proximal (approximately 0.5D) (Figure 6-10b).

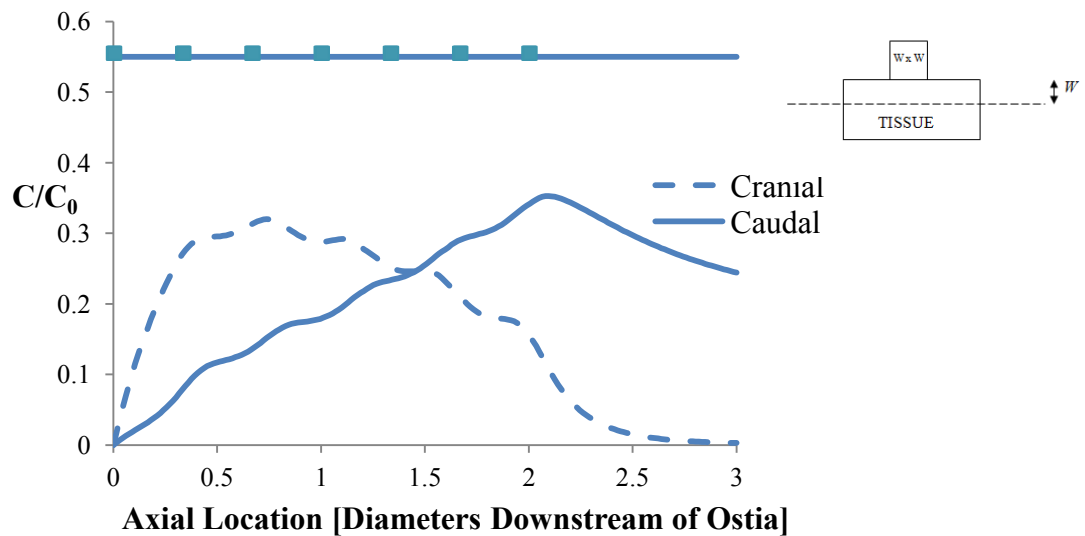


Figure 6-7: Spatial drug concentration profiles for multiple struts placed at the ARO. Shown for the case of no radius (sharp-edged corner). Stent struts are placed sequentially apart at a distance $d=20$ strut widths apart, for a total length of 12 mm. Concentration is measured at a line located at 1 strut width (0.1mm) below surface (indicated as the dotted line on the schematic inset).

Importantly this variability decreases, with decreased strut spacing (Figure 6-9a and b). At smaller spacing the underlying tissue is exposed to consistently larger mural concentrations as a result of both increased number of struts and the smaller distance between obstructions. Figure 6-9a and b shows that by decreasing distance between two consecutive struts, less drug is washed out by the luminal flow. Consequently we see that when strut spacing is halved, the footprint of this interstrut pooling drug increases 3-fold. The net result is a 2-fold decrease in circumferential asymmetry when strut distance is halved (Figure 6-11a). While longitudinally asymmetry (distal/proximal) does decrease, it is not by a significant amount (Figure 6-11b). Interestingly too when the number of struts was doubled, total drug uptake only increased by 50% (not shown).

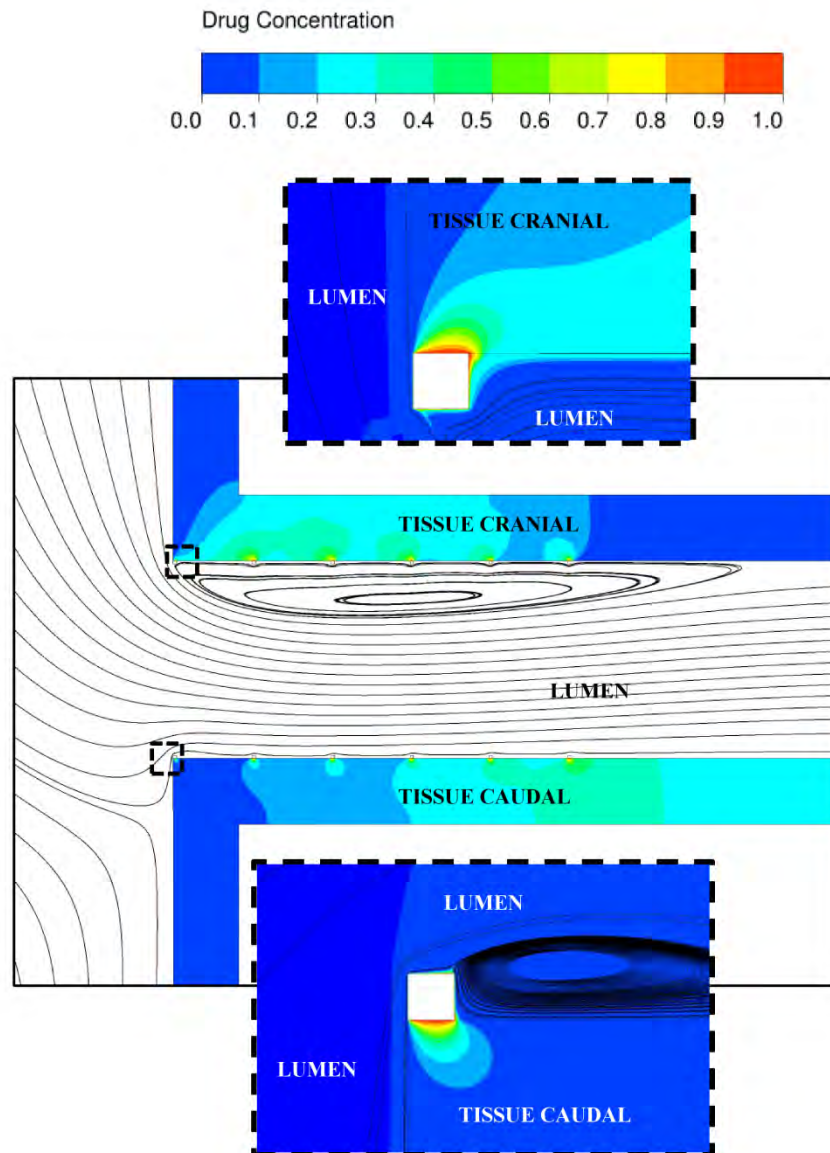


Figure 6-8: Multiple stents struts placed at the ARO, showing strut placed at the ostia. Concentration contours with flow streamlines for ARO with multiple stent struts (zoomed in), for the case of no radius, showing inset that region where a strut is located immediately at the bifurcation (0D). Flow travelling around the bifurcation impedes drug transport, while this is similar, but not to the same extent on the cranial side. The net effect is significantly impaired uptake on the proximal side.

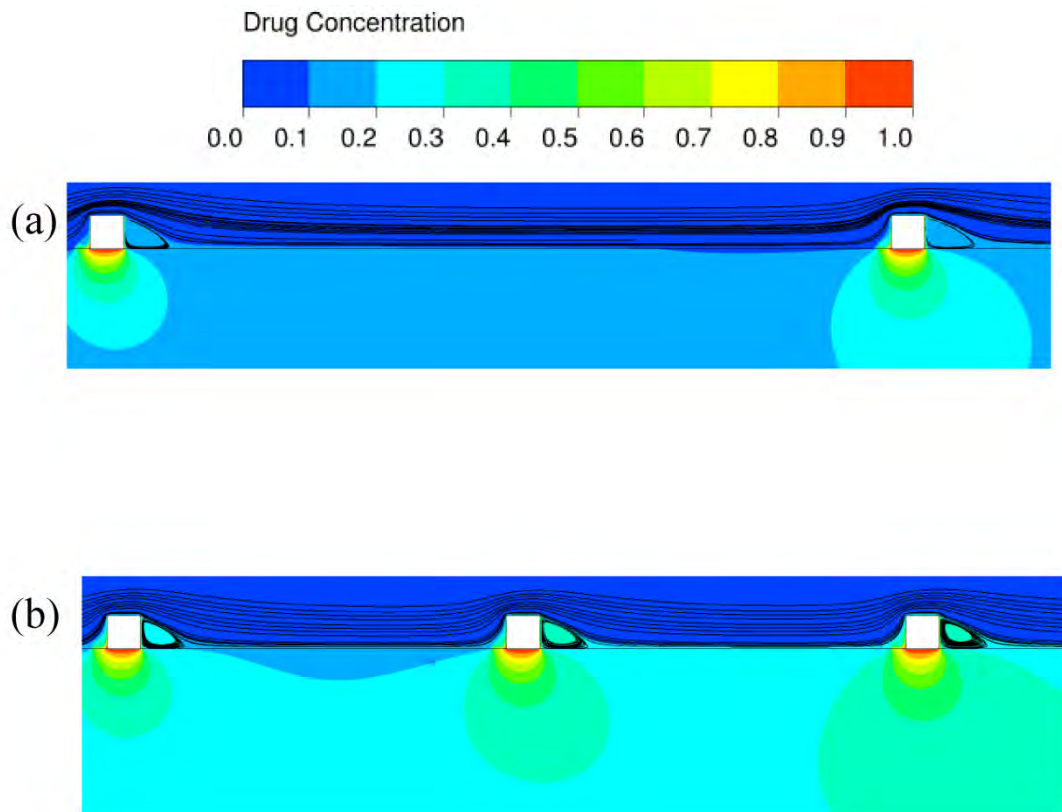


Figure 6-9: The effect of strut spacing on variability in drug concentration. a) For stent struts positioned 20 strut widths apart on the caudal wall, there is large variation in the distributed drug especially in the inter-strut regions with local peaks below the struts, and only fractional amounts of drug in the interstrut region. b) when strut spacing is decreased to 10 strut widths spatial variation in drug in the inter-strut region is greatly reduced.

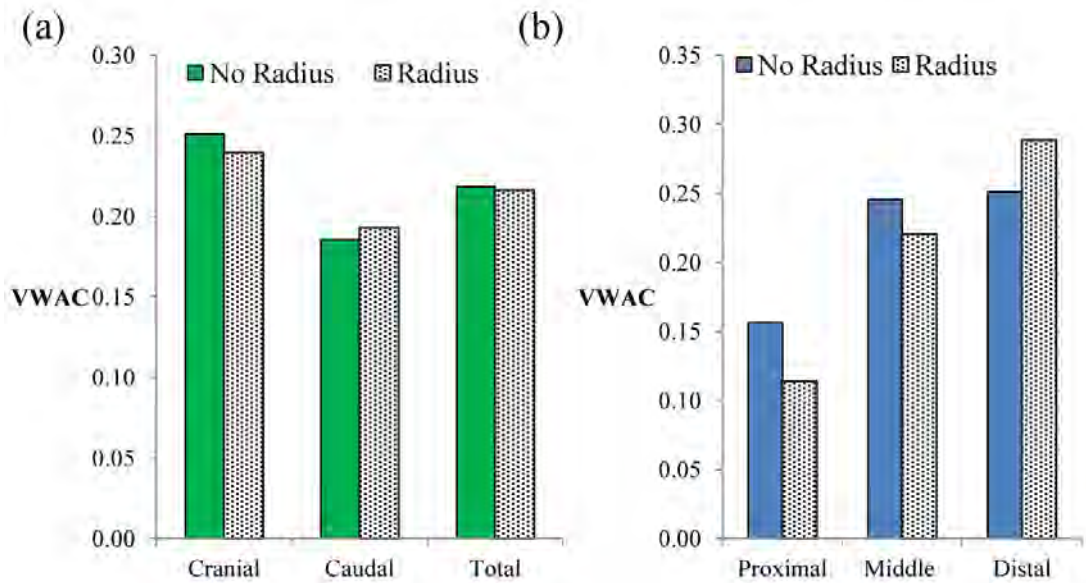


Figure 6-10: Arterial drug uptake and position relative to ostia. Volume-Weighted Average Concentration (VWAC) in the tissue for stent struts placed at a distance 20 strut widths apart, for No Radius and $R/R_R = 1$. Arterial drug is asymmetrically distributed both a) circumferentially and b) longitudinally. This asymmetry is dependent on both strut spacing and relative amounts of curvature at the ostium.

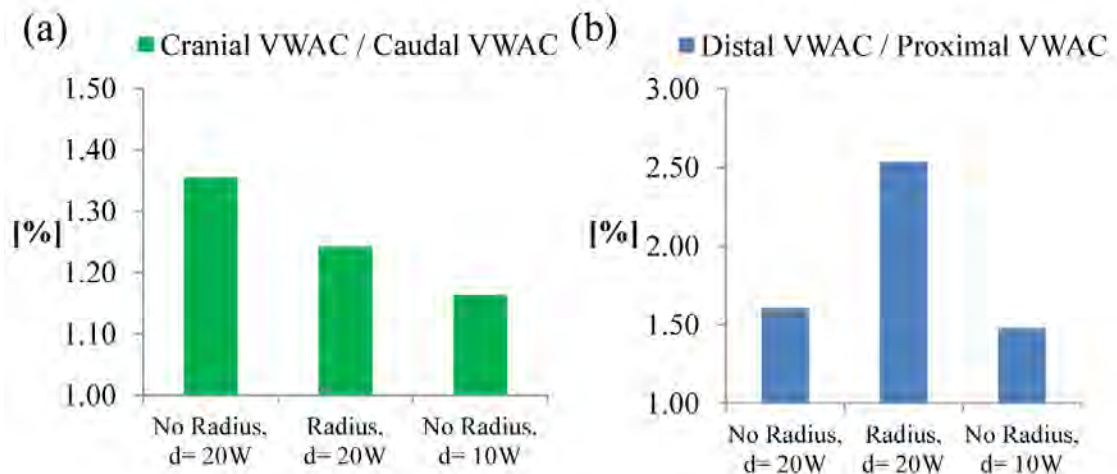


Figure 6-11: Arterial drug uptake and strut spacing. Asymmetry a) circumferentially and b) longitudinally measured as the proportionate uptake (VWAC) in the cranial and caudal tissue parts and the distal and proximal tissue parts, respectively. Results are shown for each case of curvature and when the distance between stent struts, d , decreased from 20W to 10W (Increasing the number of struts).

6.4. DISCUSSION

6.4.1. *STENT PLACEMENT AT THE ARO RESULTS IN A SPATIALLY ASYMMETRIC DISTRIBUTION OF DRUG*

The case for DES in the renal artery vasculature is unclear. Despite positive outcomes in treatment using DES over BMS, there is little statistical evidence supporting this [52] and because of already low rates of restenosis associated with bare metal stenting in the renal vasculature of diameter 6mm or larger, the recommendation is that DES should only be used in patients with smaller diameters, a single functional kidney or bilateral RAS [26, 27].

While clinical experience of percutaneous coronary- interventions with DES have been shown to be clinically successful, indications are that treatment in the use of bifurcations leads to poor clinical outcomes [50, 65]. Why exactly this occurs is not fully known.

A recent study by Nakazawa et al. of 40 autopsy cases of bifurcation sites in the coronary tree revealed key findings [70]. When comparing the relative sides of a bifurcation, the side exposed to flow separation (the flow divider) had both delayed healing (measured as uncovered struts) and 2 fold smaller neo-intima growth, when compared to the lateral side. This asymmetry in both neo-intima coverage and delayed healing was not obvious in the case of the patients treated with BMS, indicating some flow mediated mechanism of the DES accelerating these biological outcomes. Already we know flow disruptions caused by placement of the stent increase generation of thrombin [73], fibrin and platelet deposition [151], however there are also those effects

of the non-linear flow effects modulating transport of drug which are yet to be appreciated.

We know that delayed healing of the vascular bed follows high drug doses [152], and thus variations in the drug distribution will lead to altered healing states across the vessel. Results from our study confirm our hypothesis that asymmetric drug distribution follows placement of the DES at the ARO. Significant localization and concentration of drug on the side of the vessel with flow separation, and significantly impaired drug on the sides on the caudal side where the flow is highly skewed was observed. In fact drug uptake was found to be 1.4-fold larger on the side exposed to flow separation (cranial side), explaining well the observations of Nakazawa et al. at the coronary bifurcation [70].

On a single strut level, the amount of drug delivered locally was determined by its position relative to the ostia and thus degree of asymmetry in the local flow field. Drug was shown to be spread in the direction of the flow field, with local uptake found to be highest in locations within or immediately downstream of the separation region, and lowest immediately upstream where flow separates and on the outer wall where flow is highly skewed. This is consistent with our understanding of the effects of flow magnitude and directionality on drug deposition [90], but also now lets us appreciate how large scale changes to the flow field in the immediate vicinity of the stent strut can create varying environments of flow stasis and drug pooling.

Circumferential asymmetry in tissue drug uptake along the vessel was shown to persist as long as flow was axially misaligned. Once flow has recovered from bifurcation only

the flow alterations from stent obstruction to the flow remain, resulting in a circumferentially symmetric drug distribution.

6.4.2. GEOMETRICAL CHANGES TO THE BIFURCATION IMPROVE FLOW AND SPATIAL DISTRIBUTION OF DRUG

New methods of intervention are being used in the treatment of bifurcation lesions. Flaring of the proximal stent at the ostia either by post-dilation or with a trumpet shaped stent is one technique being incorporated by clinicians to improve the mechanical characteristics of the stent and overall patency of the vessel [24, 25, 153], however this will also act to alter the local hemodynamic environment and therefore flow mediated transport of drug. There has been commentary of the hope for a drug treatment platform on these side-branch specific stents [18] however the effects of these changes when coupled to a drug treatment platform are still unknown.

Our results show flaring the vessel improves the circumferential symmetry in drug uptake by decreasing the size of the recirculation region and therefore allowing full flow recovery to occur earlier (Figure 6-3b). The size of the radius is, however, important. Only once a critical radius of curvature is reached will reverse flow be sufficiently reduced and since the development of reverse flow in the separation region is dependent on physical flow parameters, vessel and stent geometry and boundary conditions (such as downstream resistances), quantifying the actual amount of rounding necessary may be a patient-specific exercise. Importantly and crucially, longitudinal asymmetry persists, and is in fact worse in the presence of curvature. As flow moves around the now rounded ostia, the boundary layer flow is distorted and we see large local flow

rates immediately at this ostia, acting to decrease overall uptake in this proximal region by approximately 28% (Figure 6-10b).

Impaired uptake in the proximal portion of the caudal side is not favourable. In the case of ARAS, atherosclerotic lesions have been shown to initiate on the caudal side of the ostia. Lesion state affects binding sites for hydrophobic drugs such as Paclitaxel and Sirolimus by affecting elastin content and therefore drug uptake and distribution [87]. A porcine model of ARAS showed significantly depleted elastin and increased collagen at this caudal side [8]. Furthermore a collagen rich tissue is likely to cause its own mechanical strength and the mechanical injury from flaring the vessel is likely to induce its own biological response. The latter is especially important, given that simulations showed drug deposition in the presence of curvature was actually inferior.

6.4.3. STRUT SPACING CAN IMPROVE SYMMETRY OF TISSUE DRUG DISTRIBUTION

While the arterial drug distribution of any given strut may in isolation be assessed, this happens in the broader context of a surrounding network of struts and indeed the stent as a whole. Relative spacing between the struts will remain a critical determinant of arterial drug distribution [89]. By decreasing the strut spacing our results showed that variability in drug concentration decreased both longitudinally and circumferentially. This will be critical to our understanding, since by decreasing this variation, the sensitivity to position relative to the ostia decreases. This implies that by decreasing strut spacing, we can decrease the sensitivity of arterial drug distribution to geometry induced changes to the flow.

Utilising the benefits of small strut spacing in areas of large scale flow alterations (like the separation region at the ARO), provides a novel opportunity for using non-uniform spacing to improve uniformity of drug deposition. Already non-uniform spacing has been employed to improve mechanical properties of ostial stents (Jostent®, Abbott Vascular), however we posit that if combined with drug-eluting therapy, it may have benefits in improving uniformity of arterial drug in areas of large flow discontinuities.

6.4.4. THE ARO AS AN INDICATOR FOR OTHER VASCULAR BEDS

The aorta-renal geometry is significant in that it represents an extreme of fluid mechanics in the human circulation. The aorta is a large vessel $\alpha \approx 16$, and branching off this is the renal artery, a medium sized vessel where $\alpha \approx 4$. Furthermore flow around the 90 degree aorta-renal bifurcation, when coupled with low flow rates in the kidneys, causes a significant and prominent separation region. By representing the most extreme of geometry-induced flow changes, one can begin to understand the impact of altered flow environments on arterial drug deposition in the extent of the vasculature.

Computational studies allow us to obtain mechanistic insights into those processes governing arterial drug distribution, consequently assumptions are necessary in order to facilitate analysis and may require some processes to be excluded so as properly optimise computational resources. In this study we have neglected the pulsatile characteristics of blood flow. In the presence of pulsatility, the size and intensity of the fluid separation region at the ARO will be time-dependent (Figure 1-9), as well as those local flow fields surrounding the stent strut. However our results in Chapter 5 indicate that when struts are well-apposed, sensitivity to the instantaneous changes in

the fluid field is not significant. This is agreement with earlier transient scalar transport models [90, 96] which have shown transient distributions to be well approximated by their steady- flow equivalents.

A single strut based analysis in an idealised 2D geometry is inherently limited given the broader biophysical context in which the strut resides. Interactions between clusters of stent struts as well as those interactions of local and three-dimensional bulk flow fields (Dean Flow) will be present. While earlier work in a small angled bifurcation did show greater variability in arterial drug distribution on account of these three-dimensional flow characteristics [154], it is believed that this variability will be much smaller in scale that that imposed by flow separation in this longitudinal plane.

Patient and lesion specific factors have been neglected when using idealised geometries and transport processes. The presence of both lesion and mechanical injury, caused by stent expansion, will act to significantly alter tissue properties at the site of implantation [88]. These are yet to be accounted for.

6.5. CONCLUSION

Spatial variations in the tissue drug concentration arise from geometry dependent flow alterations, and will be an artefact of any separated flow. Stent position relative to flow discontinuity was found to determine drug uptake, with simulations showing high tissue drug concentrations in areas of separated and disturbed flow and much smaller concentrations on the opposite side of the vessel. The findings correlate well with

published morphological data showing increased biological response in the disturbed flow regions of the coronary bifurcation.

Simulations demonstrated that by creating curvature on the inner wall, circumferential distribution of drug could be improved. Critically though the results showed longitudinal asymmetry in drug deposition persisted and was in fact worse in the case of a rounded inner wall, with significantly impaired drug uptake in the tissue proximal to the ostia. In fact simulations showed that in the presence of curvature at the ostia, total drug uptake into the tissue was actually inferior to that with a sharp edged corner. Finally sensitivity to the large scale flow misalignments can be minimized with optimal stent design; a decrease in strut spacing resulted in a more symmetric tissue drug distribution.

CHAPTER 7. CONCLUSIONS

7.1. SPECIFIC FINDINGS

The central hypothesis of this thesis was that the hemodynamic environment local to the vascular bed will determine the extent of the tissue drug distribution. This was investigated by considering the role of key fluid dynamic parameters in determining drug deposition.

In Chapter 4, the existence of a flow-mediated component in stent-based drug delivery, was confirmed using a novel bench-top method. Results obtained from this custom-designed method revealed a marker drug distribution that was sensitive to net flow magnitude, flow directionality and strut geometry. In particular the distribution of marker drug shown to be extended in regions downstream to the strut, and with variation across the 2D channel, following the velocity profile. Furthermore by creating a greater obstruction to the flow, we observed a greater flow-mediated component to the flow. The *in-vitro* model was demonstrated to be an effective method in which to appreciate the existence and significance of flow-mediated deposition in local drug delivery.

In Chapter 5 we examined the effect of pulsatility on arterial drug patterns. Theoretical considerations of pulsatile blood flow elucidated a vascular-bed dependent variation in Womersley number and allowed us to derive relevant parameters for exploring the flow-mediated effects on arterial drug deposition. Simulations on two-dimensional computational models of stent struts within arterial beds revealed a relative

independence of drug distribution to variations in the unsteady flow environment, under fully-apposed deployment settings, with these findings validated using the bench-top framework. However in contrast, models simulating suboptimal deployment settings revealed a complex interplay between arterial drug distribution, pulsatility and the extent of malapposition.

In Chapter 6, we investigated how stent placement in non-linear flow field determines arterial drug deposition, considering the specific case of stent placement at the Aorta-Renal Ostia (ARO). The results showed that further to those local flow alterations induced by the stent strut, geometry-induced flow separation at the ARO lead to significant spatial variation in tissue drug uptake. Stent position relative to flow discontinuity was found to determine the extent of these variations. Specifically simulations showed disproportionately higher tissue drug concentrations in areas of separated and disturbed flow when compared the opposite wall. This correlates well with morphological data of explanted coronary bifurcations, showing detectable patterns of denuded endothelium persisting in regions within the flow disruption and evidence of a more neointimal hyperplastic response on the lateral wall [70]. The role of fluid mechanics is therefore critical to our understanding of device efficacy in these vessels.

The extent of the flow disruption could be minimized by creating curvature on the inner walls. However most interestingly, computational modelling revealed that while circumferential uniformity of drug improved with a rounded inner, local arterial drug uptake was *not improved*. The results showed that longitudinal uniformity of drug patterns could be improved by decreasing strut spacing. Together the results imply that

these sensitivities to the large scale flow misalignments can be minimized through optimal stent design.

7.2. GENERAL FINDINGS

Through sophisticated computational models and implementation of a novel benchtop framework, we have been able to demonstrate sensitivity to the arterial drug that is defined by vascular geometry, procedural settings and flow pulsatility. It is then natural to ask, how these results may change or modify the existing *state of the art* of computational models? Furthermore, do they have any implications for pre-clinical device design and testing? What are the implications for the clinic? We explore several ways our results may impact the scientific and medical communities.

7.2.1. COMPUTATIONAL MODELS ARE INVALUABLE TOOLS IN STENT-BASED RESEARCH

Simulating physiological transport systems is becoming increasingly popular in research [91], especially as it relates to stent based drug delivery. However realistic physiological function span a wide range of space and time scales, and so assumptions and simplification are often necessary to harness available computational power. Because of this, computationally derived solutions are, on their own, limited in their impact, so are often paired with experimentally determined results. However a less appreciated fact is that computational simulations offer resolution where animal models and sophisticated bench top models can't: offering critical insight into those biophysical mechanisms driving outcome.

This was the case in Chapter 5, where computational results revealed a dependence on pulsatility that was defined by wall displacement. However critically the highly

idealised bench top model was incapable of resolving those micro element changes in wall displacement, and it was only through computational modelling that this relationship between device settings, pulsatile flow and arterial drug delivery could be appreciated. Indeed it is the case that computational models offer unparalleled resolution, and this is precisely why they are invaluable research tools in the area of stent-based drug delivery.

7.2.1. CAN WE RUN SIMPLIFIED MODELS?

Numerical models are often employed in biomedical device-related research, yet the multi-scale nature and mathematical complexity of physiological function requires the use of large amounts of computational resources- sometimes prohibitively so. From a simulation perspective, being able to run models of stent based drug delivery in simplified forms would significantly reduce computational cost and time, and thus enable greater scope of study.

The aim of this thesis was to determine which of those hemodynamic parameters are essential to our understanding of arterial drug deposition in stent-based delivery. Summarizing these effects we found the following. The evidence suggests that pulsatility is not a significant determinant of arterial drug deposition, but only in so far as the device *is ideally apposed*. Thus one could approximate the effects of pulsatile flow on arterial drug distribution using its steady flow equivalent under ideal device deployment settings only. The Reynolds number is important- the net-direction and magnitude of the flow, governed by steady flow parameter Re , significantly affects drug deposition patterns and net uptake. Stent position in the vessel does matter. Position relative to a vessel geometry induced- flow disruptions will determine the extent of

local variations of drug. In this way, predicting arterial drug distribution will be specific to stent design and patient.

Thus in simulations of DES, where the stented vessel geometry is reconstructed from patient specific data, accurate resolution of stent strut malapposition and non-linearity's in the vascular geometry should be an imperative; high resolution imaging tools, such as optical coherence tomography, should make this possible in the future.

7.2.2. BLOOD FLOW PULSATILITY AND THE BENEFITS OF LOCAL DRUG DELIVERY

Part of the benefit of DES is that flow establishes a locally extended drug distribution, however this relies on some kind of flow separation simultaneously adjacent to strut coating and wall. The larger the flow disruption, the larger the extent of the distribution of drug. How the pulsatility of luminal flow affects the extent of this distribution, and thus the benefit of DES, in the context of physiologically realistic flow, has yet to be appreciated.

The analysis in Chapter 5 revealed a complex interplay between frequency and arterial drug distribution. A change in frequency varies not only the time scale of changes in the local flow disruptions but also the magnitude of these changes. Consequently a variation in the vessel Womersley number via a change in cardiac pressure pulse frequency, changed not only the instantaneous extent of the flow disruption but also their time-averaged behaviour. Specifically when frequency decreases, we see larger oscillations over a longer time period. This will simultaneously act to extend drug uptake proximally and decrease drug quantity in the distal aspect, when compared to a flow with only small instantaneous changes in their length. Together the results imply that

drug uptake in a dynamically changing flow field will be lesser in magnitude but larger in extent to that with approximately steady standing recirculation zones. Therefore if we define an effective stent-based drug therapy to be a locally extended distribution of drug, we can say that *effect of DES* is lost with an increase in α via a frequency change. This effect is lost even further with stent malapposition: where drug levels drop off dramatically with displacement of the strut away from the vessel wall. These results indicate that both pulsatility *and* deployment settings are integral to understanding the effect of drug delivery from endovascular stents.

7.2.3. GUIDING PRECLINICAL STUDIES FOR DES IN PERIPHERAL VASCULATURE

Prior to any clinical trial, drug dosing and kinetics of the stent must be characterized using *in-vitro* and *in-vivo* (animal) models [78, 155]. Preclinical models are essential to understand safety and efficacy of the DES in the peripheral vasculature, much the same way as they were for the coronary stent. Understanding the sensitivity to different hemodynamic conditions may help guide these preclinical studies in peripheral vasculature.

As a guide for animal models: Our results showed that arterial drug distribution patterns were significantly affected by geometry, flow rates and device settings. Selecting animals that have similar geometry and net flow rates (Reynolds number) to humans, will therefore be essential to understand exactly how drug dosage and local variation in spatially distributed drug determines biologic effect in humans. We found drug deposition to be relatively independent of cardiac frequency, as long as the device

is ideally deployed. Deployment settings (malapposed/well-apposed) should thus be carefully considered.

As a platform for correlating *in-vitro* and *in-vivo* data: *In-vitro* and *in-vivo* preclinical models are critical in determining an optimal drug dosage and release strategy [155]. The two are distinctly different though. Where the *in-vitro* measures elution with time into an aqueous environment, *in-vivo* drug release is characterised by measuring arterial drug levels locally and systematically *in-vivo* [155]; requiring stent removal and residual drug content to be analysed at given time points [117]. Poor correlations have been reported between release studies and animal models, and animal models with human data [79], most likely due to the fact arterial drug deposition is dependent on many complex processes post-elution (See Section 1.4). Due to the limited resolution of measuring drug release and distribution in animal *in-vivo* models, a bench-top model that allows for transient examination of both luminal and tissue compartments, would be extremely valuable in preclinical evaluations of drug pharmacokinetics.

In this thesis we present a novel, dynamically equivalent and physiologically realistic bench-top model of stent based drug delivery. The first of its kind, this model allows for the pharmacokinetics to be appreciated while also accounting for sensitivities in the hemodynamic microenvironment (caused by stent protrusion into the flow). We believe that this method has the potential to fill the knowledge gap between *in-vitro* release studies and *in-vivo* animal models, by transiently mapping spatial drug distribution in the controlled bench-top method with *in-vivo* response.

7.2.4. SPECIFIC CASE OF STENTING IN THE RENAL ARTERY.

The results presented in Chapter 6 provide further insight into the mechanisms governing local drug delivery, in particular how both local and core flow disruptions lead to significant heterogeneity in the spatially distributed drug. When coupled with the published experimental study [70] discussed in Section 6.4.1, the results point to an association between vascular geometry induced flow patterns, arterial drug deposition and biological response not yet appreciated.

Yet on their own, these mechanistic insights are, indeed, both pre-clinically and clinically relevant. How exactly can these scientific underpinnings of local vascular drug delivery found in Chapter 6, be utilized in both the design of the devices specific to the renal artery and in the clinic?

We postulate that the blood flow field caused by the intervention will determine arterial drug maps. Thus physiologic flow should be used as guide procedurally, to improve uniformity of locally eluted drug. In the presence of a flow discontinuity, both near-wall and regional flow acts to significantly vary the distribution of drug along the length of the artery, leading to areas proximal to ostia with significantly impaired drug uptake. Adding curvature at the ostia (flaring) was shown not to improve this. On the other hand, it may be possible to improve this deposition of drug by incorporating a release strategy that is tailored to the flow physics. In particular we recognize that utilizing non-uniform strut spacing or variable drug loading may improve the asymmetry in drug deposition caused by changes in the flow field along the length of the stent.

Furthermore, the advent of high resolution vascular imaging means that opportunities exist for clinicians to create patient specific predictive models of local drug delivery. In particular, high resolution optical coherence tomography has been recently made available, and using these patient-specific images and data we could create predictive flow models and drug distributions.

Importantly though, without a clear and validated association between vascular flow and clinical outcome, stent use in the renal artery remains uncertain. Our hope is that future studies will more thoroughly investigate the predictive power of physiologic flow and drug distribution, with measures of biological response and clinical outcome.

7.3. FUTURE DIRECTIONS

The computational models used in this thesis have included many simplifications and assumptions so as to facilitate analysis. One of these has been to use a model to simulate the non-Newtonian characteristics of blood flow. In this thesis we considered only the Carreau model to simulate the shear-thinning characteristics of blood flow, however there exist many other models of such behaviour, especially as it relates to a realistic range of hematocrit values. Future work should consider running a sensitivity analysis on those various models available.

Stenting in vascular beds outside of the coronary vasculature requires many other considerations beyond those flow-related changes. First there are those changes associated with tissue architecture; simply there are those changes due to a change in vascular bed- where diffusive transport will be modulated by relative amounts of

elastin. Drug diffusivities are yet to be characterised for the renal and other peripheral vasculature. In order to create predictive and physiologically realistic computational models, quantitatively characterising the diffusion properties in the non-coronary vasculature should be an imperative of any future work

There are also lesion and patient specific factors that will change with anatomical position that were not considered in this thesis. In the renal artery the disease manifests preferentially on the caudal side [8]. Lesion length in the superficial femoral artery is long (approximately 30cm) and often significantly calcified [88]. As data on these arterial wall morphologies and lesion state becomes available, it is hoped that they can be implemented into the computational model.

The mechanical injury induced by stenting in the peripheral vasculature has also been neglected from this work. The superficial femoral artery undergoes significant and chronic loading variations with movement of the leg, including extension, contraction, compression, elongation, flexion and torsion. Stenting the artery introduces a rigid segment in a seemingly compliant region- which is exacerbated by the instance of atherosclerosis which contributes further rigidity- risking stent deformation, for instance abrupt kinks [156] or even fracture. The Sirocco II trial reported stent fracture rate SFA at 9% [14]. While fractures occur only in a small percentage of cases, it is the chronic mechanical trauma that is considered a significant predictor for in-stent restenosis. This chronic stent-vessel interaction and hyperproliferation may require higher doses and longer drug release profiles [88], as well as the fact that larger devices used in SFA treatment require larger overall drug loads, and thus has a potential for local toxicity.

Understanding how mechanical injury impedes/facilitates/modulates drug deposition should be a key focus of further research into peripheral stenting with DES.

REFERENCES

1. Davies, M.J., *A macro and micro view of coronary vascular insult in ischemic heart disease*. *Circulation*, 1990. **82**(3 Suppl): p. II38-46.
2. Cooper, C.J., T.P. Murphy, A. Matsumoto, M. Steffes, D.J. Cohen, M. Jaff, R. Kuntz, K. Jamerson, D. Reid, K. Rosenfield, J. Rundback, R. D'Agostino, W. Henrich, and L. Dworkin, *Stent revascularization for the prevention of cardiovascular and renal events among patients with renal artery stenosis and systolic hypertension: rationale and design of the CORAL trial*. *American Heart Journal*, 2006. **152**(1): p. 59-66.
3. Ross, R., *Atherosclerosis--an inflammatory disease*. *New England Journal of Medicine*, 1999. **340**(2): p. 115-26.
4. Nakashima, Y., H. Fujii, S. Sumiyoshi, T.N. Wight and K. Sueishi, *Early human atherosclerosis - Accumulation of lipid and proteoglycans in intimal thickenings followed by macrophage infiltration*. *Arteriosclerosis Thrombosis and Vascular Biology*, 2007. **27**(5): p. 1159-1165.
5. Glagov, S., C. Zarins, D.P. Giddens and D.N. Ku, *Hemodynamics and atherosclerosis. Insights and perspectives gained from studies of human arteries*. *Archives of Pathology and Laboratory Medicine*, 1988. **112**(10): p. 1018-31.
6. Ku, D.N., D.P. Giddens, C.K. Zarins and S. Glagov, *Pulsatile flow and atherosclerosis in the human carotid bifurcation. Positive correlation between plaque location and low oscillating shear stress*. *Arteriosclerosis*, 1985. **5**(3): p. 293-302.
7. Nguyen, N.D. and A.K. Haque, *Effect of hemodynamic factors on atherosclerosis in the abdominal-aorta*. *Atherosclerosis*, 1990. **84**(1): p. 33-39.
8. Neufeld, E.B., Z.X. Yu, D. Springer, Q. Yu and R.S. Balaban, *The renal artery ostium flow diverter: Structure and potential role in atherosclerosis*. *Atherosclerosis*, 2010. **211**(1): p. 153-158.
9. Houle, S. and M.R. Roach, *Flow studies in a rigid model of an aorto-renal junction - a case for high shear as a cause of the localization of sudanophilic lesions in rabbits*. *Atherosclerosis*, 1981. **40**(3-4): p. 231-244.
10. Yamamoto, T., Y. Ogasawara, A. Kimura, H. Tanaka, O. Hiramatsu, K. Tsujioka, M.J. Lever, K.H. Parker, C.J. Jones, C.G. Caro, and F. Kajiya, *Blood*

velocity profiles in the human renal artery by Doppler ultrasound and their relationship to atherosclerosis. Arteriosclerosis, Thrombosis, and Vascular Biology, 1996. 16(1): p. 172-7.

11. Defeyter, P.J., P.P.T. Dejaegere and P.W. Serruys, *Incidence, predictors, and management of acute coronary-occlusion after coronary angioplasty. American Heart Journal, 1994. 127(3): p. 643-651.*
12. Sigwart, U., J. Puel, V. Mirkovitch, F. Joffre and L. Kappenberger, *Intravascular stents to prevent occlusion and restenosis after trans-luminal angioplasty. New England Journal of Medicine, 1987. 316(12): p. 701-706.*
13. Holmes, D.R., M. Savage, J.M. LaBlanche, L. Grip, P.W. Serruys, P. Fitzgerald, D. Fischman, S. Goldberg, J.A. Brinker, A.M. Zeiher, L.M. Shapiro, J. Willerson, B.R. Davis, J.J. Ferguson, J. Popma, S.B. King, A.M. Lincoff, J.E. Tchong, R. Chan, and J.R. Granett, *Results of prevention of restenosis with tranilast and its outcomes (PRESTO) trial. Circulation, 2002. 106(10): p. 1243-1250.*
14. Duda, S.H., M. Bosiers, J. Lammer, D. Scheinert, T. Zeller, A. Tielbeek, J. Anderson, B. Wiesinger, G. Tepe, A. Lansky, C. Mudde, H. Tielemans, and J.P. Beregi, *Sirolimus-eluting versus bare nitinol Stent for obstructive superficial femoral artery disease: The SIROCCO II trial. Journal of Vascular and Interventional Radiology, 2005. 16(3): p. 331-338.*
15. Lederman, R.J., F.O. Mendelsohn, R. Santos, H.R. Phillips, R.S. Stack and J.J. Crowley, *Primary renal artery stenting: Characteristics and outcomes after 363 procedures. American Heart Journal, 2001. 142(2): p. 314-323.*
16. Carr III, T.M., S.S. Sabri, U.C. Turba, A.W. Park, W.E.A. Saad, J.F. Angle and A.H. Matsumoto, *Stenting for atherosclerotic renal artery stenosis. Techniques in Vascular and Interventional Radiology, 2010. 13(2): p. 134-145.*
17. Lutsep, H.L., S. Barnwell, M. Mawad, D. Chiu, M. Hartmann, W. Hacke, J.R. Reul, R. Biniek, L. Guterman, A. Yahia, C. Weiller, H. Zeumer, S. Bracard, X. Ducrocq, J. Dion, O. Samuels, C.R. Gomez, P. King, and S.S. Investigators, *Stenting of symptomatic atherosclerotic lesions in the vertebral or intracranial arteries (SSYLVIA) study results. Stroke, 2004. 35(6): p. 1388-1392.*
18. Sheiban, I., P. Omedè, G. Biondi-Zoccai, C. Moretti and G.P.S. F.and, *Update on dedicated bifurcation stents. Journal of Interventional Cardiology, 2009. 22: p. 150-155.*
19. Goldstein, J.A., R. Kolluri and K. Rocha-Singh, *Technical considerations for renal artery stenting. Vascular Disease Management, 2006. 3(3): p. 260-265.*
20. Kawarada, O., Y. Yokoi and K. Takemoto, *The characteristics of dissemination of embolic materials during renal artery stenting. Catheterization and Cardiovascular Interventions, 2007. 70(6): p. 784-788.*

21. Serruys, P.W., B.H. Strauss, K.J. Beatt, M.E. Bertrand, J. Puel, A.F. Rickards, B. Meier, J.J. Goy, P. Vogt, L. Kappenberger, and U. Sigwart, *Angiographic follow-up after placement of a self-expanding coronary-artery stent*. New England Journal of Medicine, 1991. **324**(1): p. 13-17.
22. Hoffmann, R., G.S. Mintz, G.R. Dussailant, J.J. Popma, A.D. Pichard, L.F. Satler, K.M. Kent, J. Griffin and M.B. Leon, *Patterns and mechanisms of in-stent restenosis - A serial intravascular ultrasound study*. Circulation, 1996. **94**: p. 1247-1254.
23. Komatsu, R., M. Ueda, T. Naruko, A. Kojima and A.E. Becker, *Neointimal tissue response at sites of coronary stenting in humans: Macroscopic, histological, and immunohistochemical analyses*. Circulation, 1998. **98**(3): p. 224-233.
24. Regar, E., G. Sianos and P.W. Serruys, *Stent development and local drug delivery*. British Medical Bulletin, 2001. **59**: p. 227-248.
25. Welt, F.G.P. and C. Rogers, *Inflammation and restenosis in the stent era*. Arteriosclerosis, Thrombosis, and Vascular Biology, 2002. **22**(11): p. 1769-1776.
26. Hong, S.J., M.H. Kim, T.H. Ahn, Y.K. Ahn, J.H. Bae, W.J. Shim, Y.M. Ro and D.S. Lim, *Multiple predictors of coronary restenosis after drug-eluting stent implantation in patients with diabetes*. Heart, 2006. **92**(8): p. 1119-1124.
27. Waller, B.F., P.J. Palumbo, J.T. Lie and W.C. Roberts, *Status of the coronary arteries at necropsy in diabetes mellitus with onset after age 30 years. Analysis of 229 diabetic patients with and without clinical evidence of coronary heart disease and comparison to 183 control subjects*. American Journal of Medicine, 1980. **69**(4): p. 498-506.
28. Schampaert, E., E.A. Cohen, M. Schluter, F. Reeves, M. Traboulsi, L.M. Title, R.E. Kuntz and J.J. Popma, *The Canadian study of the sirolimus-eluting stent in the treatment of patients with long de novo lesions in small native coronary arteries (C-SIRIUS)*. Journal of the American College of Cardiology, 2004. **43**(6): p. 1110-1115.
29. Sullivan, T.M., S.D. Ainsworth, E.M. Langan, S. Taylor, B. Snyder, D. Cull, J. Youkey and M. Laberge, *Effect of endovascular stent strut geometry on vascular injury, myointimal hyperplasia, and restenosis*. Journal of Vascular Surgery, 2002. **36**(1): p. 143-149.
30. Dussailant, G.R., G.S. Mintz, A.D. Pichard, K.M. Kent, L.F. Satler, J.J. Popma, S.C. Wong and M.B. Leon, *Small stent size and intimal hyperplasia contribute to restenosis - a volumetric intravascular ultrasound analysis*. Journal of the American College of Cardiology, 1995. **26**(3): p. 720-724.

31. Kearney, M., A. Pieczek, L. Haley, D.W. Losordo, V. Andres, R. Schainfeld, K. Rosenfield and J.M. Isner, *Histopathology of in-stent restenosis in patients with peripheral artery disease*. *Circulation*, 1997. **95**(8): p. 1998-2002.
32. Vignali, C., I. Bargellini, M. Lazzereschi, R. Cioni, P. Petruzzi, D. Caramella, S. Pinto, V. Napoli, V. Zampa and C. Bartolozzi, *Predictive factors of in-stent restenosis in renal artery stenting: A retrospective analysis*. *Cardiovascular and Interventional Radiology*, 2005. **28**(3): p. 296-302.
33. Rees, C.R., *Stents for atherosclerotic renovascular disease*. *Journal of Vascular and Interventional Radiology*, 1999. **10**(6): p. 689-705.
34. Süselbeck, T., A. Latsch, H. Siri, B. Gonska, T. Poerner, S. Pflieger, B. Schumacher, M. Borggreffe and K.K. Haase, *Role of vessel size as a predictor for the occurrence of in-stent restenosis in patients with diabetes mellitus*. *American Journal of Cardiology*, 2001. **88**(3): p. 243-247.
35. Zeller, T., A. Rastan, M. Kliem, U. Schwarzwälder, U. Frank, K. Bürgelin, T. Schwarz, P. Amantea, C. Müller and F.J. Neumann, *Impact of carbon coating on the restenosis rate after stenting of atherosclerotic renal artery stenosis*. *Journal of Endovascular Therapy*, 2005. **12**(5): p. 605-611.
36. LaDisa, J.F., L.E. Olson, R.C. Molthen, D.A. Hettrick, P.F. Pratt, M.D. Hardel, J.R. Kersten, D.C. Warltier and P.S. Pagel, *Alterations in wall shear stress predict sites of neointimal hyperplasia after stent implantation in rabbit iliac arteries*. *American Journal of Physiology-Heart and Circulatory Physiology*, 2005. **288**(5): p. H2465-H2475.
37. Wentzel, J.J., R. Krams, J.C. Schuurbiers, J.A. Oomen, J. Kloet, W.J. van Der Giessen, P.W. Serruys and C.J. Slager, *Relationship between neointimal thickness and shear stress after Wallstent implantation in human coronary arteries*. *Circulation*, 2001. **103**(13): p. 1740-5.
38. Berry, J.L., A. Santamarina, J.E. Moore, S. Roychowdhury and W.D. Routh, *Experimental and computational flow evaluation of coronary stents*. *Annals of Biomedical Engineering*, 2000. **28**: p. 386-398.
39. Frank, A.O., P.W. Walsh and J.E. Moore, *Computational fluid dynamics and stent design*. *Artificial Organs*, 2002. **26**(7): p. 614-621.
40. Srinivas, K., T. Nakayama, M. Ohta, S. Obayashi and T. Yamaguchi, *Studies on design optimization of coronary stents*. *Journal of Medical Devices-Transactions of the Asme*, 2008. **2**(1).
41. Duraiswamy, N., B. Jayachandran, J. Byrne, J.E. Moore, Jr. and R.T. Schoepfoerster, *Spatial distribution of platelet deposition in stented arterial models under physiologic flow*. *Annals of Biomedical Engineering*, 2005. **33**(12): p. 1767-77.

42. Rogers, C. and E.R. Edelman, *Endovascular stent design dictates experimental restenosis and thrombosis*. *Circulation*, 1995. **91**(12): p. 2995-3001.
43. Seo, T., L.G. Schachter and A.I. Barakat, *Computational study of fluid mechanical disturbance induced by endovascular stents*. *Annals of Biomedical Engineering*, 2005. **33**(4): p. 444-456.
44. Jeremias, A. and A. Kirtane, *Balancing efficacy and safety of drug-eluting stents in patients undergoing percutaneous coronary intervention*. *Annals of Internal Medicine*, 2008. **148**(3): p. 234-238.
45. Sapoval, M., M. Zähringer, P. Pattynama, C. Rabbia, C. Vignali, G. Maleux, L. Boyer, M. Szczerbo-Trojanowska, W. Jaschke, G. Hafsaht, M. Downes, J.P. Beregi, N. Veeger, and A. Talen, *Low-profile stent system for treatment of atherosclerotic renal artery stenosis: The GREAT trial*. *Journal of Vascular and Interventional Radiology*, 2005. **16**: p. 1195-1202.
46. Stone, G.W., J.W. Moses, S.G. Ellis, J. Schofer, K.D. Dawkins, M. Morice, A. Colombo, E. Schampaert, E. Grube, A.J. Kirtane, D.E. Cutlip, M. Fahy, S.J. Pocock, R. Mehran, and M.B. Leon, *Safety and efficacy of sirolimus- and paclitaxel-eluting coronary stents*. *New England Journal of Medicine*, 2007. **356**(10): p. 998-1008.
47. Spaulding, C., J. Daemen, E. Boersma, D.E. Cutlip and P.W. Serruys, *A pooled analysis of data comparing sirolimus-eluting stents with bare-metal stents*. *New England Journal of Medicine*, 2007. **356**(10): p. 989-997.
48. Roy, P., A.N. Buch, A. Javaid, T. Okabe, V. Raya, T.L. Pinto Slottow, D.H. Steinberg, K. Smith, Z. Xue, N. Gevorkian, L.F. Satler, K.M. Kent, W.O. Suddath, A.D. Pichard, J. Lindsay, and R. Waksman, *Impact of "off-label" utilization of drug-eluting stents on clinical outcomes in patients undergoing percutaneous coronary intervention*. *American Journal of Cardiology*, 2008. **101**(3): p. 293-9.
49. Beohar, N., C.J. Davidson, K.E. Kip, L. Goodreau, H.A. Vlachos, S.N. Meyers, K.H. Benzuly, J.D. Flaherty, M.J. Ricciardi, C.L. Bennett, and D.O. Williams, *Outcomes and complications associated with off-label and untested use of drug-eluting stents*. *Journal of the American Medical Association*, 2007. **297**(18): p. 1992-2000.
50. Win, H.K., A.E. Caldera, K. Maresh, J. Lopez, C.S. Rihal, M.A. Parikh, J.F. Granada, S. Marulkar, D. Nassif, D.J. Cohen, and N.S. Kleiman, *Clinical outcomes and stent thrombosis following off-label use of drug-eluting stents*. *Journal of the American Medical Association*, 2007. **297**(18): p. 2001-2009.
51. Uder, M. and U. Humke, *Endovascular therapy of renal artery stenosis: where do we stand today?* *Cardiovascular and Interventional Radiology*, 2005. **28**(2): p. 139-47.

52. Zähringer, M., M. Sapoval, P.M.T. Pattynama, C. Rabbia, C. Vignali, G. Maleux, L. Boyer, M. Szczerbo-Trojanowska, W. Jaschke, G. Hafsahl, M. Downes, J.-P. Beregi, N.J.G.M. Veeger, H.-P. Stoll, and A. Talen, *Sirolimus-eluting versus bare-metal low-profile stent for renal artery treatment (GREAT trial): Angiographic follow-up after 6 months and clinical outcome up to 2 years*. *Journal of Endovascular Therapy*, 2007. **14**: p. 460-468.
53. Zeller, T., C. Müller, U. Frank, K. Bürgelin, L. Sinn, B. Horn and H. Roskamm, *Gold coating and restenosis after primary stenting of ostial renal artery stenosis*. *Catheterization and Cardiovascular Interventions*, 2003. **60**(1): p. 1-6.
54. Karnabatidis, D., S. Spiliopoulos, A. Diamantopoulos, K. Katsanos, G.C. Kagadis, S. Kakkos and D. Siablis, *Primary everolimus-eluting stenting versus balloon angioplasty with bailout bare metal stenting of long infrapopliteal lesions for treatment of critical limb ischemia*. *Journal of Endovascular Therapy*, 2011. **18**(1): p. 1-12.
55. Siablis, D., D. Karnabatidis, K. Katsanos, A. Diamantopoulos, N. Christeas and G.C. Kagadis, *Infrapopliteal application of paclitaxel-eluting stents for critical limb ischemia: Midterm angiographic and clinical results*. *Journal of Vascular and Interventional Radiology*, 2007. **18**(11): p. 1351-1361.
56. Siablis, D., D. Karnabatidis, K. Katsanos, A. Diamantopoulos, S. Spiliopoulos, G.C. Kagadis and J. Tsolakis, *Infrapopliteal application of sirolimus-eluting versus bare metal stents for critical limb ischemia: Analysis of long-term angiographic and clinical outcome*. *Journal of Vascular and Interventional Radiology*, 2009. **20**(9): p. 1141-1150.
57. Siablis, D., D. Karnabatidis, K. Katsanos, G.C. Kagadis, P. Kraniotis, A. Diamantopoulos and J. Tsolakis, *Sirolimus-eluting versus bare stents after suboptimal infrapopliteal angioplasty for critical limb ischemia: Enduring 1-year angiographic and clinical benefit*. *Journal of Endovascular Therapy*, 2007. **14**(2): p. 241-250.
58. Siablis, D., P. Kraniotis, D. Karnabatidis, G.C. Kagadis, K. Katsanos and J. Tsolakis, *Sirolimus-eluting versus bare stents for bailout after suboptimal infrapopliteal angioplasty for critical limb ischemia: 6-Month angiographic results from a nonrandomized prospective single-center study*. *Journal of Endovascular Therapy*, 2005. **12**(6): p. 685-695.
59. Scheinert, D., M. Ulrich, S. Scheinert, J. Sax, S. Braunlich and G. Biamino, *Comparison of sirolimus-eluting vs. bare-metal stents for the treatment of infrapopliteal obstructions*. *EuroIntervention*, 2006. **2**(2): p. 169-74.
60. Iakovou, I., T. Schmidt, E. Bonizzoni, L. Ge, G.M. Sangiorgi, G. Stankovic, F. Airolidi, A. Chieffo, M. Montorfano, M. Carlino, I. Michev, N. Corvaja, C. Briguori, U. Gerckens, E. Grube, and A. Colombo, *Incidence, predictors, and outcome of thrombosis after successful implantation of drug-eluting stents*.

- Jama-Journal of the American Medical Association, 2005. **293**(17): p. 2126-2130.
61. Windecker, S. and B. Meier, *Late coronary stent thrombosis*. Circulation, 2007. **116**(17): p. 1952-1965.
 62. Ong, A.T.L., E.P. McFadden, E. Regar, P.P.T. de Jaegere, R.T. van Domburg and P.W. Serruys, *Late angiographic stent thrombosis (LAST) events with drug-eluting stents*. Journal of the American College of Cardiology, 2005. **45**(12): p. 2088-2092.
 63. Morice, M.C., P.W. Serruys, J.E. Sousa, J. Fajadet, E. Ban Hayashi, M. Perin, A. Colombo, G. Schuler, P. Barragan, G. Guagliumi, F. Molnar, and R. Falotico, *A randomized comparison of a sirolimus-eluting stent with a standard stent for coronary revascularization*. New England Journal of Medicine, 2002. **346**(23): p. 1773-80.
 64. Schampaert, E., J.W. Moses, J. Schofer, M. Schluter, A.H. Gershlick, E.A. Cohen, D.A. Palisaitis, G. Breithardt, D.J. Donohoe, H. Wang, J.J. Popma, R.E. Kuntz, and M.B. Leon, *Sirolimus-eluting stents at two years: A pooled analysis of SIRIUS, E-SIRIUS, and C-SIRIUS with emphasis on late revascularizations and stent thromboses*. American Journal of Cardiology, 2006. **98**(1): p. 36-41.
 65. Farb, A. and A.B. Boam, *Stent thrombosis redux - The FDA perspective*. New England Journal of Medicine, 2007. **356**(10): p. 984-987.
 66. Farb, A., A.P. Burke, F.D. Kolodgie and R. Virmani, *Pathological mechanisms of fatal late coronary stent thrombosis in humans*. Circulation, 2003. **108**(14): p. 1701-1706.
 67. Finn, A.V., M. Joner, G. Nakazawa, F. Kolodgie, J. Newell, M.C. John, H.K. Gold and R. Virmani, *Pathological correlates of late drug-eluting stent thrombosis - Strut coverage as a marker of endothelialization*. Circulation, 2007. **115**(18): p. 2435-2441.
 68. Joner, M., A.V. Finn, A. Farb, E.K. Mont, F.D. Kolodgie, E. Ladich, R. Kutys, K. Skorija, H.K. Gold and R. Virmani, *Pathology of drug-eluting stents in humans. Delayed healing and late thrombotic risk*. Journal of the American College of Cardiology, 2006. **48**(1): p. 193-202.
 69. Kotani, J.i., M. Awata, S. Nanto, M. Uematsu, F. Oshima, H. Minamiguchi, G.S. Mintz and S. Nagata, *Incomplete neointimal coverage of sirolimus-eluting stents. Angioscopic findings*. Journal of the American College of Cardiology, 2006. **47**(10): p. 2108-2111.
 70. Nakazawa, G., S.K. Yazdani, A.V. Finn, M. Vorpahl, F.D. Kolodgie and R. Virmani, *Pathological findings at bifurcation lesions: The impact of flow distribution on atherosclerosis and arterial healing after stent implantation*. Journal of the American College of Cardiology, 2010. **55**(16): p. 1679-1687.

71. Joner, M., G. Nakazawa, A.V. Finn, S.C. Quee, L. Coleman, E. Acampado, P.S. Wilson, K. Skorija, Q. Cheng, X. Xu, H.K. Gold, F.D. Kolodgie, and R. Virmani, *Endothelial cell recovery between comparator polymer-based drug-eluting stents*. Journal of the American College of Cardiology, 2008. **52**(5): p. 333-42.
72. Guagliumi, G., M.A. Costa, V. Sirbu, G. Musumeci, H.G. Bezerra, N. Suzuki, A. Matiashvili, N. Lortkipanidze, L. Mihalsik, A. Trivisonno, O. Valsecchi, G.S. Mintz, O. Dressler, H. Parise, A. Maehara, E. Cristea, A.J. Lansky, R. Mehran, and G.W. Stone, *Strut coverage and late malapposition with paclitaxel-eluting stents compared with bare metal stents in acute myocardial infarction: optical coherence tomography substudy of the Harmonizing Outcomes with Revascularization and Stents in Acute Myocardial Infarction (HORIZONS-AMI) Trial*. Circulation, 2011. **123**(3): p. 274-81.
73. Kolandaivelu, K., R. Swaminathan, W.J. Gibson, V.B. Kolachalama, K.L. Nguyen-Ehrenreich, V.L. Giddings, L. Coleman, G.K. Wong and E.R. Edelman, *Stent thrombogenicity early in high-risk interventional settings Is driven by stent design and deployment and protected by polymer-drug coatings*. Circulation, 2011. **123**(13): p. 1400-1409.
74. Hassan, A.K.M., S.C. Bergheanu, T. Stijnen, B.L. van der Hoeven, J.D. Snoep, J.W.M. Plevier, M.J. Schalij and J.W. Jukema, *Late stent malapposition risk is higher after drug-eluting stent compared with bare-metal stent implantation and associates with late stent thrombosis*. European Heart Journal, 2010. **31**(10): p. 1172-1180.
75. Cook, S., P. Wenaweser, M. Togni, M. Billinger, C. Morger, C. Seiler, R. Vogel, O. Hess, B. Meier and S. Windecker, *Incomplete stent apposition and very late stent thrombosis after drug-eluting stent implantation*. Circulation, 2007. **115**(18): p. 2426-2434.
76. Murata, A., D. Wallace-Bradley, A. Tellez, C. Alviar, M. Aboodi, A. Sheehy, L. Coleman, L. Perkins, G. Nakazawa, G. Mintz, G.L. Kaluza, R. Virmani, and J.F. Granada, *Accuracy of optical coherence tomography in the evaluation of neointimal coverage after stent implantation*. JACC Cardiovascular Imaging, 2010. **3**(1): p. 76-84.
77. Prati, F., F. Stazi, J. Dutary, A. La Manna, A. Di Giorgio, T. Pawlosky, N. Gonzalo, M.E. Di Salvo, F. Imola, C. Tamburino, M. Albertucci, and F. Alfonso, *Detection of very early stent healing after primary angioplasty: an optical coherence tomographic observational study of chromium cobaltum and first-generation drug-eluting stents. The DETECTIVE study*. Heart, 2011. **97**(22): p. 1841-6.
78. Schwartz, R.S., E. Edelman, R. Virmani, A. Carter, J.F. Granada, G.L. Kaluza, N.A.F. Chronos, K.A. Robinson, R. Waksman, J. Weinberger, G.J. Wilson, and R.L. Wilensky, *Drug-eluting stents in preclinical studies updated consensus*

- recommendations for preclinical evaluation.* Circulation: Cardiovascular Interventions, 2008. **1**(2): p. 143-153.
79. Venkatraman, S. and F. Boey, *Release profiles in drug-eluting stents: Issues and uncertainties.* Journal of Controlled Release, 2007. **120**(3): p. 149-160.
 80. Finn, A.V., F.D. Kolodgie, J. Harnek, L.J. Guerrero, E. Acampado, K. Tefera, K. Skoriya, D.K. Weber, H.K. Gold and R. Virmani, *Differential response of delayed healing and persistent inflammation at sites of overlapping sirolimus- or paclitaxel-eluting stents.* Circulation, 2005. **112**(2): p. 270-278.
 81. Balakrishnan, B., J.F. Dooley, G. Kopia and E.R. Edelman, *Intravascular drug release kinetics dictate arterial drug deposition, retention, and distribution.* Journal of Controlled Release, 2007. **123**: p. 100-108.
 82. Mongrain, R., I. Faik, R.L. Leask, J. Rodes-Cabau, E. Larose and O.F. Bertrand, *Effects of diffusion coefficients and struts apposition using numerical simulations for drug eluting coronary stents.* Journal of Biomechanical Engineering-Transactions of the Asme, 2007. **129**: p. 733-742.
 83. Hwang, C.W., D. Wu and E.R. Edelman, *Physiological transport forces govern drug distribution for stent-based delivery.* Circulation, 2001. **104**: p. 600-605.
 84. Hwang, C.W. and E.R. Edelman, *Arterial ultrastructure influences transport of locally delivered drugs.* Circulation Research, 2002. **90**(7): p. 826-832.
 85. Levin, A.D., N. Vukmirovic, C.W. Hwang and E.R. Edelman, *Specific binding to intracellular proteins determines arterial transport properties for rapamycin and paclitaxel.* Proceedings of the National Academy of Sciences of the United States of America, 2004. **101**(25): p. 9463-9467.
 86. Finn, A.V., G. Nakazawa, M. Joner, F.D. Kolodgie, E.K. Mont, H.K. Gold and R. Virmani, *Vascular responses to drug eluting stents - Importance of delayed healing.* Arteriosclerosis Thrombosis and Vascular Biology, 2007. **27**(7): p. 1500-1510.
 87. Tzafiriri, A.R., N. Vukmirovic, V.B. Kolachalama, I. Astafieva and E.R. Edelman, *Lesion complexity determines arterial drug distribution after local drug delivery.* Journal of Controlled Release, 2010. **142**(3): p. 332-8.
 88. Machan, L., *Clinical experience and applications of drug-eluting stents in the noncoronary vasculature, bile duct and esophagus.* Advanced Drug Delivery Reviews, 2006. **58**: p. 447-462.
 89. Balakrishnan, B., A.R. Tzafiriri, P. Seifert, A. Groothuis, C. Rogers and E.R. Edelman, *Strut position, blood flow, and drug deposition - Implications for single and overlapping drug-eluting stents.* Circulation, 2005. **111**: p. 2958-2965.

90. Kolachalama, V.B., A.R. Tzafiriri, D.Y. Arifin and E.R. Edelman, *Luminal flow patterns dictate arterial drug deposition in stent-based delivery*. Journal of Controlled Release, 2009. **133**: p. 24-30.
91. Di Ventura, B., C. Lemerle, K. Michalodimitrakis and L. Serrano, *From in vivo to in silico biology and back*. Nature, 2006. **443**(7111): p. 527-533.
92. Vairo, G., M. Cioffi, R. Cottone, G. Dubini and F. Migliavacca, *Drug release from coronary eluting stents: A multidomain approach*. Journal of Biomechanics, 2010. **43**(8): p. 1580-1589.
93. Kolachalama, V.B., E.G. Levine and E.R. Edelman, *Luminal flow amplifies stent-based drug deposition in arterial bifurcations*. PLoS ONE, 2009. **4**(12): p. 1-9.
94. Migliavacca, F., F. Gervaso, M. Prosi, P. Zunino, S. Minisini, L. Formaggia and G. Dubini, *Expansion and drug elution model of a coronary stent*. Computer Methods in Biomechanics and Biomedical Engineering, 2007. **10**: p. 63-73.
95. McMichael, W.J. and J.D. Hellums, *Interphase mass and heat transfer in pulsatile flow*. American Institute of Chemical Engineers Journal, 1975. **21**(4): p. 743-752.
96. Ma, P., X. Li and D.N. Ku, *Heat and mass transfer in a separated flow region for high Prandtl and Schmidt numbers under pulsatile conditions*. International Journal of Heat and Mass Transfer, 1994. **37**: p. 2723-2736.
97. Seidlitz, A., S. Nagel, B. Semmling, N. Grabow, H. Martin, V. Senz, C. Harder, K. Sternberg, K.P. Schmitz, H.K. Kroemer, and W. Weitschies, *Examination of drug release and distribution from drug-eluting stents with a vessel-simulating flow-through cell*. European Journal of Pharmaceutics and Biopharmaceutics, 2011. **78**(1): p. 36-48.
98. Moore, J.E., Jr. and D.N. Ku, *Pulsatile velocity measurements in a model of the human abdominal aorta under resting conditions*. Journal of Biomechanical Engineering, 1994. **116**(3): p. 337-46.
99. Holenstein, R. and D.N. Ku, *Reverse flow in the major infrarenal vessels - a capacitive phenomenon*. Biorheology, 1988. **25**(6): p. 835-842.
100. Ku, D.N., *Blood flow in arteries*. Annual Review of Fluid Mechanics, 1997. **29**: p. 399-434.
101. Womersley, J.R., *Method for the calculation of velocity, rate of flow and viscous drag in arteries when the pressure gradient is known*. Journal of Physiology-London, 1955. **127**(3): p. 553-563.
102. Zamir, M., *The physics of pulsatile flow*. Biological Physics Series, ed. E. Greenbaum. 2000, New York: Springer-Verlag.

103. Ku, D.N. and D.P. Giddens, *Laser doppler anemometer measurements of pulsatile flow in a model carotid bifurcation*. Journal of Biomechanics, 1987. **20**(4): p. 407-421.
104. Mills, C.J., I.T. Gabe, J.H. Gault, D.T. Mason, J. Ross, Jr., E. Braunwald and J.P. Shillingford, *Pressure-flow relationships and vascular impedance in man*. Cardiovascular Research, 1970. **4**(4): p. 405-17.
105. Moore, R., J. Bishoff, S. Loenig and S.G. Docimo, *Minimally invasive urologic surgery*. 2005: Taylor & Francis.
106. Blum, U., B. Krumme, P. Flugel, A. Gabelmann, T. Lehnert, C. Buitrago-Tellez, P. Schollmeyer and M. Langer, *Treatment of ostial renal-artery stenoses with vascular endoprotheses after unsuccessful balloon angioplasty*. New England Journal of Medicine, 1997. **336**: p. 459-465.
107. Dorros, G., M. Jaff, A. Jain, C. Dufek and L. Mathiak, *Follow-up of primary Palmaz-Schatz stent placement for atherosclerotic renal artery stenosis*. American Journal of Cardiology, 1995. **75**: p. 1051-1055.
108. Rees, C.R., J.C. Palmaz, G.J. Becker, K.O. Ehrman, G.M. Richter, B.T.a.D. M.D. and D.E. Schwarten, *Palmaz stent in atherosclerotic stenoses involving the ostia of the renal arteries: Preliminary report of a multicenter study*. Radiology, 1991. **181**: p. 507-514.
109. Van De Ven, P., R. Kaatee, J.J. Beutler, F.J.A. Beek, A.-J.J. Woittiez, E. Buskens, H.A. Koomans and W.P. Mali, *Arterial stenting and balloon angioplasty in ostial atherosclerotic renovascular disease: A randomised trial*. Lancet, 1999. **353**: p. 282-286.
110. Liepsch, D., S. Moravec, A.K. Rastogi and N.S. Vlachos, *Measurement and calculations of laminar flow in a ninety degree bifurcation*. Journal of Biomechanics, 1982. **15**: p. 473-485.
111. Karino, T., H.H.M. Kwong and H.L. Goldsmith, *Particle flow behaviour in models of branching vessels: I. Vortices in 90° T-junctions*. Bio rheology, 1979. **16**: p. 231-248.
112. Moore Jr, J.E., D.N. Ku, C.K. Zarins and S. Glagov, *Pulsatile flow visualization in the abdominal aorta under differing physiologic conditions: Implications for increased susceptibility to atherosclerosis*. Journal of Biomechanical Engineering, 1992. **114**: p. 391-397.
113. Mamas, M.A., V. Farooq, A. Latib, S. Sastry, S. D'Souza, P. Williams, A. Wiper, L. Neyses, M. El-Omar, D.G. Fraser, and F. Fath-Ordoubadi, *Use of the Sideguard (Cappella) stent in bifurcation lesions: a real-world experience*. EuroIntervention, 2012. **7**(10): p. 1170-80.

114. AIAA, *Guide for the verification and validation of computational fluid dynamics simulations*, in *AIAA-G-077-1998*. 1998, American Institute of Aeronautics and Astronautics: Reston.
115. Lovich, M.A., C. Creel, K. Hong, C.W. Hwang and E.R. Edelman, *Carrier proteins determine local pharmacokinetics and arterial distribution of paclitaxel*. *Journal of Pharmaceutical Sciences*, 2001. **90**: p. 1324-1335.
116. Higuchi, T., *Mechanism of sustained-action medication. Theoretical analysis of rate of release of solid drugs dispersed in solid matrices*. *Journal of Pharmaceutical Sciences*, 1963. **52**: p. 1145-9.
117. Kamath, K.R., J.J. Barry and K.M. Miller, *The Taxus (TM) drug-eluting stent: A new paradigm in controlled drug delivery*. *Advanced Drug Delivery Reviews*, 2006. **58**(3): p. 412-436.
118. Saltzman, W.M., *Drug Delivery: Engineering principles for drug therapy*. 2001, New York: Oxford University Press.
119. Chung, T.J., *Computational Fluid Dynamics*. Vol. 2nd. 2010, Cambridge: Cambridge University Press.
120. COMSOL (2010) *COMSOL Multiphysics Reference Guide v4.0a*.
121. Brooks, A.N. and T.J.R. Hughes, *Streamline upwind/Petrov–Galerkin formulations for convection dominated flows with particular emphasis on the incompressible Navier–Stokes equations*. *Computer Methods in Applied Mechanics and Engineering*, 1982. **32**(1-3): p. pp. 199–259.
122. Mavriplis, D.J., *Unstructured grid techniques*. *Annual Review of Fluid Mechanics*, 1997. **29**: p. 473-514.
123. Chung, J. and G.M. Hulbert, *A time integration algorithm for structural dynamics with improved numerical dissipation - the Generalized-Alpha Method*. *Journal of Applied Mechanics-Transactions of the Asme*, 1993. **60**(2): p. 371-375.
124. Jansen, K.E., C.H. Whiting and G.M. Hulbert, *A generalized-alpha method for integrating the filtered Navier-Stokes equations with a stabilized finite element method*. *Computer Methods in Applied Mechanics and Engineering*, 2000. **190**(3-4): p. 305-319.
125. ANSYS (2010) *ANSYS CFX Reference Guide v13.0*.
126. Barth, T.J. and D.C. Jespersen, *The design and application of upwind schemes on unstructured meshes*. *AIAA Paper: AIAA-89-0366*, 1989.
127. Rhie, C.M. and W.L. Chow, *Numerical study of the turbulent flow past an isolated airfoil with trailing edge separation*. *AIAA*, 1983. **21**: p. 1525-1532.

128. Balakrishnan, B., J. Dooley, G. Kopia and E.R. Edelman, *Thrombus causes fluctuations in arterial drug delivery from intravascular stents*. Journal of Controlled Release, 2008. **131**: p. 173-180.
129. Tada, S. and J.M. Tarbell, *Flow through internal elastic lamina affects shear stress on smooth muscle cells (3D simulations)*. American Journal of Physiology - Heart and Circulatory Physiology, 2002. **282**: p. H576-H584.
130. Holmes, D.B. and Vermeule, Jr., *Velocity profiles in ducts with rectangular cross sections*. Chemical Engineering Science, 1968. **23**(7): p. 717-&.
131. Cheng, N.S., *Formula for viscosity of glycerol-water mixture*. Industrial and Engineering Chemistry Research, 2008. **47**(9): p. 3285-3288.
132. Taylor, C.A., T.J. Hughes and C.K. Zarins, *Finite element modeling of three-dimensional pulsatile flow in the abdominal aorta: relevance to atherosclerosis*. Annals of Biomedical Engineering, 1998. **26**(6): p. 975-87.
133. Bryant, S.J., K.A. Davis-Arehart, N. Luo, R.K. Shoemaker, J.A. Arthur and K.S. Anseth, *Synthesis and characterization of photopolymerized multifunctional hydrogels: Water-soluble poly(vinyl alcohol) and chondroitin sulfate macromers for chondrocyte encapsulation*. Macromolecules, 2004. **37**(18): p. 6726-6733.
134. Hwang, C.W., D. Wu and E.R. Edelman, *Impact of transport and drug properties on the local pharmacology of drug-eluting stents*. International Journal of Cardiovascular Intervention, 2003. **5**(1): p. 7-12.
135. Hickey, A.S. and N.A. Peppas, *Solute diffusion in poly(vinyl alcohol) poly(acrylic acid) composite membranes prepared by freezing/thawing techniques*. Polymer, 1997. **38**(24): p. 5931-5936.
136. Creel, C.J., M.A. Lovich and E.R. Edelman, *Arterial paclitaxel distribution and deposition*. Circulation Research, 2000. **86**(8): p. 879-884.
137. Hose, D.R., A.J. Narracott, B. Griffiths, S. Mahmood, J. Gunn, D. Sweeney and P.V. Lawford, *A thermal analogy for modelling drug elution from cardiovascular stents*. Computer Methods in Biomechanics and Biomedical Engineering, 2004. **7**(5): p. 257-64.
138. Culbertson, C.T., S.C. Jacobson and J. Michael Ramsey, *Diffusion coefficient measurements in microfluidic devices*. Talanta, 2002. **56**(2): p. 365-373.
139. Wan, J., B. Steele, S.A. Spicer, S. Strohsband, G.R. Feijoo, T.J. Hughes and C.A. Taylor, *A one-dimensional finite element method for simulation-based medical planning for cardiovascular disease*. Computer Methods in Biomechanics and Biomedical Engineering, 2002. **5**(3): p. 195-206.

140. Papageorgiou, G.L., B.N. Jones, V.J. Redding and N. Hudson, *The area ratio of normal arterial junctions and its implications in pulse-wave reflections*. Cardiovascular Research, 1990. **24**(6): p. 478-484.
141. Olufsen, M.S., *Structured tree outflow condition for blood flow in larger systemic arteries*. American Journal of Physiology-Heart and Circulatory Physiology, 1999. **276**(1): p. H257-H268.
142. He, X.Y. and D.N. Ku, *Unsteady entrance flow development in a straight tube*. Journal of Biomechanical Engineering-Transactions of the Asme, 1994. **116**(3): p. 355-360.
143. Hansen, K.J., M.S. Edwards, T.E. Craven, G.S. Cherr, S.A. Jackson, R.G. Appel, G.L. Burke and R.H. Dean, *Prevalence of renovascular disease in the elderly: A population-based study*. Journal of Vascular Surgery, 2002. **36**(3): p. 443-451.
144. Missouriis, C.G., T. Buckenham, F.P. Cappuccio and G.A. MacGregor, *Renal artery stenosis: A common and important problem in patients with peripheral vascular disease*. American Journal of Medicine, 1994. **96**(1): p. 10-14.
145. Gross, C.M., J. Krämer, J. Waigand, F. Uhlich, H. Olthoff, F.C. Luft and R. Dietz, *Ostial renal artery stent placement for atherosclerotic renal artery stenosis in patients with coronary artery disease*. Catheterization and Cardiovascular Diagnosis, 1998. **45**(1): p. 1-8.
146. Jean, W.J., I. Al-Bitar, D.L. Zwicke, S.C. Port, D.H. Schmidt and T.K. Bajwa, *High incidence of renal artery stenosis in patients with coronary artery disease*. Catheterization and Cardiovascular Diagnosis, 1994. **32**(1): p. 8-10.
147. Schillinger, M., E. Minar and R. Ahmadi, *Treating renal artery stenosis: A statement pro endovascular therapy*. Herz, 2004. **29**(1): p. 68-75.
148. Stettler, C., S. Wandel, S. Allemann, A. Kastrati, M.C. Morice, A. Schömig, M.E. Pfisterer, G.W. Stone, M.B. Leon, J.S. de Lezo, J.J. Goy, S.J. Park, M. Sabaté, M.J. Suttorp, H. Kelbaek, C. Spaulding, M. Menichelli, P. Vermeersch, M.T. Dirksen, P. Cervinka, A.S. Petronio, A.J. Nordmann, P. Diem, B. Meier, M. Zwahlen, S. Reichenbach, S. Trelle, S. Windecker, and P. Jüni, *Outcomes associated with drug-eluting and bare-metal stents: a collaborative network meta-analysis*. Lancet, 2007. **370**(9591): p. 937-948.
149. Carr, R.T. and S.L. Kotha, *Separation surfaces for laminar flow in branching tubes - Effect of Reynolds number and geometry*. Journal of Biomechanical Engineering, 1995. **117**: p. 442-447.
150. Karino, T. and H.L. Goldsmith, *Particle flow behavior in models of branching vessels. II. Effects of branching angle and diameter ratio on flow patterns*. Biorheology, 1985. **22**: p. 87-104.

151. Duraiswamy, N., J.M. Cesar, R.T. Schoepfoerster and J.E. Moore, *Effects of stent geometry on local flow dynamics and resulting platelet deposition in an in vitro model*. Biorheology, 2008. **45**(5): p. 547-561.
152. Farb, A., P.F. Heller, S. Shroff, L. Cheng, F.D. Kolodgie, A.J. Carter, D.S. Scott, J. Froehlich and R. Virmani, *Pathological analysis of local delivery of paclitaxel via a polymer-coated stent*. Circulation, 2001. **104**(4): p. 473-479.
153. Yoshizumi, M., H. Kurihara, T. Sugiyama, F. Takaku, M. Yanagisawa, T. Masaki and Y. Yazaki, *Hemodynamic shear stress stimulates endothelin production by cultured endothelial cells*. Biochemical and Biophysical Research Communications, 1989. **161**(2): p. 859-864.
154. Dean, W.R., *Note on the motion of fluid in a curved pipe*. Philosophical Magazine, 1927. **20**: p. 208-223.
155. Schwartz, R.S., E.R. Edelman, A. Carter, N.A. Chronos, C. Rogers, K.A. Robinson, R. Waksman, L. Machan, J. Weinberger, R.L. Wilensky, J.L. Goode, O.D. Hottenstein, B.D. Zuckerman, and R. Virmani, *Preclinical evaluation of drug-eluting stents for peripheral applications: recommendations from an expert consensus group*. Circulation, 2004. **110**(16): p. 2498-505.
156. Arena, F.J., *Arterial kink and damage in normal segments of the superficial femoral and popliteal arteries abutting nitinol stents - A common cause of late occlusion and restenosis? A single-center experience*. Journal of Invasive Cardiology, 2005. **17**(9): p. 482-486.

APPENDIX

Appendix 1.

License agreements for reprinting images.

Figure 1-1: Figure reprinted with permission from John Wiley & Sons

RightsLink License #: 2877561068053

Figure 1-2: Figure reprinted with permission from Springer

RightsLink License #: 2877560118875

Figure 1-4: Figure reprinted with permission from Wolter Kluwer Health

RightsLink License #: 2877560404080

Figure 1-5: Figure reprinted with permission from Elsevier

RightsLink License #: 2877560589925

Figure 1-6: Figure reprinted with permission from Wolter Kluwer Health

RightsLink License #: 287756070442

Figure 1-7: Figure reprinted with permission from Elsevier

RightsLink License #: 2877560894520

Figure 1-8: Figure reprinted with permission from *Cardiovascular Research*

RightsLink License #: 2878130659533

Figure 1-9: Figure reprinted with permission from Wolter Kluwer Health

RightsLink License #: 2877570394402

Appendix 2.

Fourier Transformation of Flow Waveform

```
This code generates Fourier coefficients for a signal (eg. Flow waveform).
function Q_t=fft_flowwaveform(t,ydata)
%%% Very Important. Y_data must be cyclical, and must not repeat itself.
%%% Therefore if the Time increment is delta_t, and your time period is Tp
%%% then truncate data at t=Tp-delta_t
%%% Eg. If Flow cycle is of length 1_second (60bpm). And you have data
%%% points at each 1/100 second. Include data from 0sec:0.99second, since 0
%%% sec is the same as 1 sec (cyclical in nature).

%%% Input is T data, and Y data
%%% Output is input for CFX, the term Q= a0 +alcos(Wt)+
%%% Where W is your fundamental frequency = 2*pi /Tp
%%% (eg. Tp might be 60bpm=1second)
%%%
%units in seconds

Y=ydata;
L=length(Y);
delta_t=t(2)-t(1); % time step
Tp=t(end)+delta_t; % Time period is t(n+1)
Fs=1/Tp; % Sampling Frequency
NFFT = 2^nextpow2(L); % Next power of 2 from length of y
Yfft = fft(Y);
f = [1:L:L-1]';

plot(f,2./L.*abs(Yfft(1:(L-1))))
title('Amplitude Spectrum of y(t)')
xlabel('Frequency (Hz)')
ylabel('|Y(f)|')

figure

Y1=Yfft(1:(L-1));
%to plot in real space
N=floor((L)/2);
Y=Y1/L; %scale by n
Tp1=Tp
z1=0:Tp1/L:(L-2)*Tp1/L
i=sqrt(-1);om=2*pi/Tp1;
a0=Y(1);
y=a0;
an=2.*real(Y(2:N));bn=-2.*imag(Y(2:N))
for m=1:length(an)
    y=y+real((an(m)+i.*bn(m)).*exp(-i.*m.*om.*z1))'
end
plot(t,ydata,'-b')
hold on
plot(z1,y,'-*r')
xlabel('Time');ylabel('Magnitude Flow')

hold on
inv_Y=ifftn(Yfft)
nin=L-1;Tp=Tp -delta_t;
plot(0:Tp/nin:(nin-1)*Tp/nin,inv_Y(1:floor(L-1)),'*k')
legend('Data Points','Fourier Expansion','Inverse Fourier')

% This outputs the Fourier harmonics as a string for copy-paste into CFX
Q_t=strcat(num2str(a0));
for m=1:length(an)
    Q_t=strcat(Q_t,'+',num2str(an(m)), '*cos(',num2str(m),'*W*t)
+',num2str(bn(m)), '*sin(',num2str(m),'*W*t)');
end
```

Appendix 3.

A complex pressure waveform $A_n e^{int}$ for a vessel can be derived from known unsteady flow harmonics, Q_n , using Womersley's framework in eqn. (5-2). The complex flow waveform can be written as $Q_n e^{i\omega t}$, and in polar form $Q_n e^{i\omega t} = M_q e^{i(\omega t + \phi_q)}$. By letting $J_1(\alpha i^{3/2}) = M_1 e^{i\theta_1}$ and $J_0(\alpha i^{3/2}) = M_0 e^{i\theta_0}$, then we can write,

$$\frac{2 J_1(\alpha i^{3/2})}{\alpha i^{3/2} J_0(\alpha i^{3/2})} = \frac{2 M_1}{\alpha M_0} e^{i\delta}$$

where $\delta = \theta_1 - \theta_0 - \frac{3\pi}{4}$, then for each harmonic n , eqn. (5-2) can be rewritten as,

$$M_q e^{i(\omega t + \phi_q)} = \frac{\pi R^2}{i\omega\rho} \left(1 - \frac{2 M_1}{\alpha M_0} e^{i\delta} \right) A_n e^{i\omega t}$$

$$A_n e^{i\omega t} = \frac{i\omega\rho}{\pi R^2} \frac{M_q e^{i(\omega t + \phi_q)}}{\left(1 - \frac{2 M_1}{\alpha M_0} e^{i\delta} \right)}$$

$$A_n e^{i\omega t} = \frac{i\omega\rho}{\pi R^2} \frac{M_q e^{i(\omega t + \phi_q)} \left(1 - \frac{2 M_1}{\alpha M_0} e^{-i\delta} \right)}{\left(1 - \frac{2 M_1}{\alpha M_0} e^{i\delta} \right) \left(1 - \frac{2 M_1}{\alpha M_0} e^{-i\delta} \right)}$$

$$A_n e^{i\omega t} = \frac{i\omega\rho}{\pi R^2} \frac{M_q \left(e^{i(\omega t + \phi_q)} - \frac{2 M_1}{\alpha M_0} e^{i(\omega t + \phi_q - \delta)} \right)}{\left(1 - \frac{4 M_1}{\alpha M_0} \cos\delta + \frac{4}{\alpha^2} \left(\frac{M_1}{M_0} \right)^2 \right)}$$

Then the resulting pressure gradient waveform, $K_n(t)$, is the real part of $A_n e^{int}$ which is:

$$K_n(t) = \text{Real} \left\{ \frac{i\omega\rho M_q \left(e^{i(\omega t + \phi_q)} - \frac{2 M_1}{\alpha M_0} e^{i(\omega t + \phi_q - \delta)} \right)}{\pi R^2 \left(1 - \frac{4 M_1}{\alpha M_0} \cos\delta + \frac{4}{\alpha^2} \left(\frac{M_1}{M_0} \right)^2 \right)} \right\} \quad (7-1)$$

The first six renal arterial flow harmonics are derived from data points taken from Taylor et al. [132], using the algorithm in Appendix 2. This is shown in Figure 3-3b.

Pressure gradient harmonics are derived from these flow harmonics, using eqn. (7-1) and are shown in Table 7-1, and plotted in Figure 5-1.

Table 7-1: Components of the complex pressure wave in the renal artery.

n	α	A_n (Pa)	M_n	ϕ_n (rads)
1	4.138377	669.5599 + -115.2616 i	679.4083	-0.1705
2	5.85255	-96.1725 + -1391.8042 i	1395.1230	-1.6398
3	7.16788	-660.567 + 355.4751 i	750.1408	2.6479
4	8.276755	-66.7178 + 345.1536 i	351.5427	1.7617

5	9.253693	67.4814 + -132.4266i	148.6289	-1.0995
6	10.13691	-50.9514 + 117.5305i	128.0994	1.9799

NOTE:

A note on Fourier representation of harmonics and waveforms:

Any complex number can be written be expressed in its polar form:

That is given $Q = A + iB$, then

$$M_q = \sqrt{A^2 + B^2},$$

$$\phi_q = -\tan^{-1}\left(\frac{B}{A}\right)$$

And then the flow gradient can be expressed as

$$q = \text{Real}(Q_n e^{int}) = M_q \cos(nt + \phi_q)$$

Where M_q is the modulus and ϕ_q is the argument of the complex gradient Q .

Note 2: $\text{Real}\{ie^{i\theta}\} = -\sin(\theta)$.

Appendix 4.

CALIBRATION OF SIGNAL

The signal was analysed to determine that there was a linear relationship between fluorescence and depth of sample (of known concentration). Figure a shows that a linear relationship can be assumed for at least the thicknesses of the hydrogel sample ($0 < l < 3\text{mm}$) and fluorescence intensity. In Figure 7-1b a calibration based on this assumption is presented. Here fluorescent intensity, measured as count/pixel, plotted against concentration depth, in units g/m^2 (concentration*depth of sample) is shown.

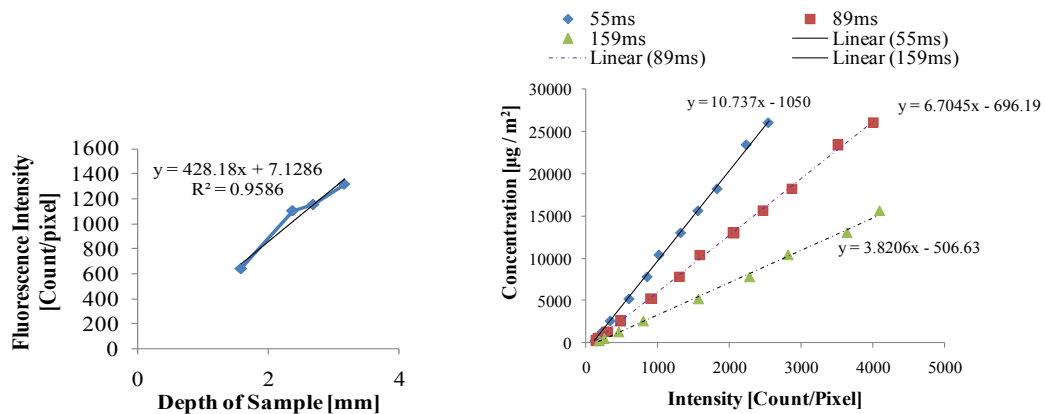


Figure (7-1:a) The fluorescent intensity for depth of excited field, showing an approximately linear relationship and (b) Calibration Fluorescent Intensity Concentration for different exposure times for a sample of depth $\leq 3\text{mm}$.

Appendix 5.

SENSITIVITY ANALYSIS: MESH CONVERGENCE

A mesh sensitivity analysis was performed, by performing sequential refinements on the mesh. Solution was determined to be sufficiently refined when there was less than a 2% change in the variable of interest, that is when error, $E < 0.02$. The first variables of interest is the area-weighted average concentration in the local area of the tissue. The error for this variable is defined as:

$$E_{AWAC} = \frac{\iint_{\Omega} |c_{n+1}(x) - c_n(x)| dx}{\iint_{\Omega} c_{n+1}(x) dx}$$

where $\Omega \in \{-5W < x < 5W, 0 < y < 2W\}$ and W is the strut width. The second variable of interest is the integral of concentration across the tissue area, denoted the Area-Under the Curve (AUC). The error in this variable is defined as:

$$E_{AUC} = \frac{\int_L |c_{n+1}(x) - c_n(x)| dx}{\int_L c_{n+1}(x) dx}$$

where $c_{n+1}(x)$ and $c_n(x)$, represent the concentrations for mesh solution at refinement levels n and $n + 1$, and $L \in \{-2.5W < x < 2.5W, y = 0.2W\}$.

Due to high computational cost the simulation was run for a time period of 25seconds (truncated short of the 50s endpoint used in final analysis). Figure 7-2 shows the convergence of solution with increasing irregular mesh Refinement. A solution was

determined to be sufficiently refined when there was approximately 2.8×10^4 elements corresponding to 1.12×10^5 degrees of freedom.

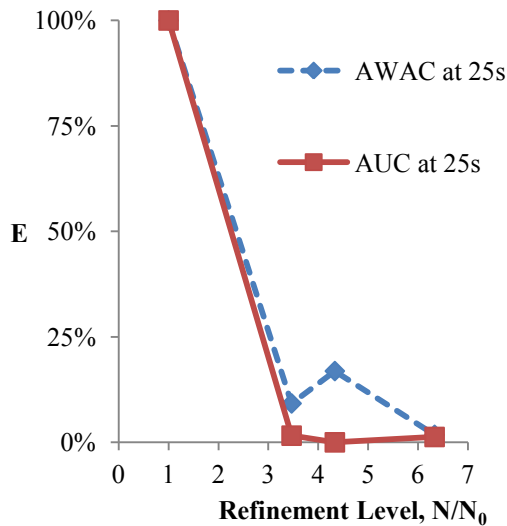


Figure 7-2: Mesh sensitivity analysis. Refinement level is measured as the Number of DOF, N , in each refinement divided by the number of DOF in the original mesh N_0 . Results show convergence of solution (Decreasing E) with increasing refinement.

SENSITIVITY ANALYSIS: TIME-STEP CONVERGENCE

For a time-dependent solution it becomes necessary to discretize the solution time so as to accurately resolve time-dependent features of the solution. For a model of drug elution there will be three key events; first there will be the drug release as modelled by the Higuchi model, there will be transient transport of the drug in both fluid and tissue domains and finally there is the pulsatile nature of the fluid flow defined over a cycle of length T_{period} . In order to determine whether final solution was in fact independent of time step taken, the time step in the solution for $\alpha=1$ (the maximum T_{period}) was sequentially halved. The solution was considered time-independent when the error in

Area-Weighted Average Concentration (Figure 7-3) for sequential solutions, E_{AWAC} , was less than 0.3%.

A time-step when Δt was the maximum value of either 0.06 s or $0.05 * T_{\text{period}}$ was found to resolve temporal dependence.

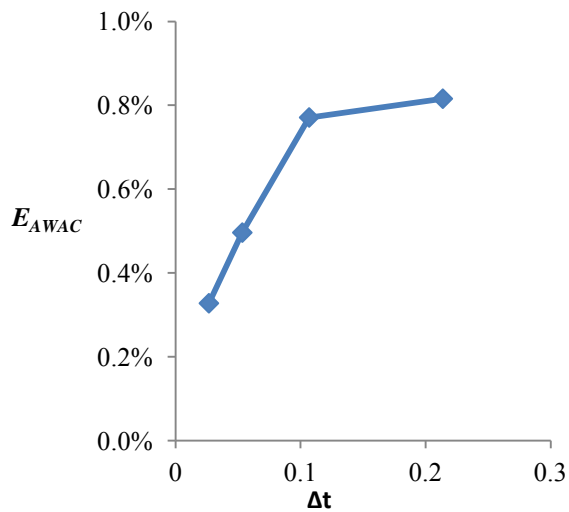


Figure 7-3: Time step convergence sensitivity analysis. Error in the Area-weighted average concentration as the time step is sequentially halved. Solution converged when error was less than 0.3%.

Appendix 6.

SENSITIVITY ANALYSIS: MESH CONVERGENCE

A mesh sensitivity analysis was performed, by performing sequential refinements on the mesh. Solution was determined to be sufficiently refined when there was less than a 6% change in the variable of interest, that is when error, $E < 0.06$. The variable of interest is the volume-weighted average concentration in the local volume of the tissue. The error for this variable is defined as:

$$E_{AWAC} = \frac{\iint_{\Omega} |c_{n+1}(x) - c_n(x)| dx}{\iint_{\Omega} c_{n+1}(x) dx}$$

where $\Omega \in \{-20W < x < 20W\}$ and W is the strut width, and $c_{n+1}(x)$ and $c_n(x)$, represent the concentrations for mesh solution at refinement levels n and $n + 1$, and $L \in \{-2.5W < x < 2.5W, y = 0.2W\}$.

Figure 7-4 shows the convergence of solution with increasing irregular mesh refinement.

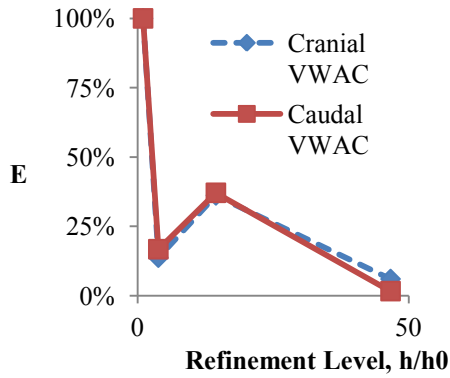


Figure 7-4: Mesh sensitivity analysis. Refinement level is measured as the elements, N , in each refinement divided by the number of elements in the original mesh N_0 . Results show convergence of solution (Decreasing E) with increasing refinement.

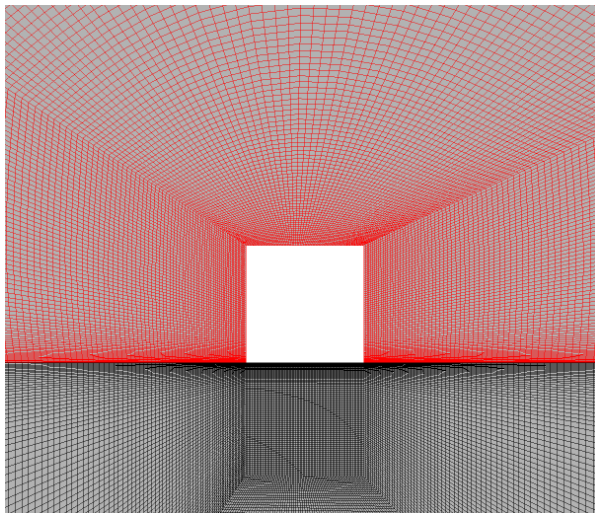


Figure 7-5: Local mesh distribution of computational domain- mesh elements shown in the immediate vicinity of stent strut (in white) on the caudal side. Red lines show mesh element edges in the lumen domain, black line show mesh element edges in arterial wall domain.